

---


Electronic Theses and Dissertations, 2020-

---

2020

## Enhancement of absorptance by ultrafast laser pulse shaping for efficient laser processing of thin polymers

Arifur Rahaman  
*University of Central Florida*

 Part of the [Polymer and Organic Materials Commons](#), and the [Semiconductor and Optical Materials Commons](#)

Find similar works at: <https://stars.library.ucf.edu/etd2020>

University of Central Florida Libraries <http://library.ucf.edu>

This Doctoral Dissertation (Open Access) is brought to you for free and open access by STARS. It has been accepted for inclusion in Electronic Theses and Dissertations, 2020- by an authorized administrator of STARS. For more information, please contact [STARS@ucf.edu](mailto:STARS@ucf.edu).

---

### STARS Citation

Rahaman, Arifur, "Enhancement of absorptance by ultrafast laser pulse shaping for efficient laser processing of thin polymers" (2020). *Electronic Theses and Dissertations, 2020-*. 616.

<https://stars.library.ucf.edu/etd2020/616>

ENHANCEMENT OF ABSORPTANCE BY ULTRASHORT LASER PULSE SHAPING FOR  
EFFICIENT LASER PROCESSING OF THIN POLYMERS

By

ARIFUR RAHAMAN

B.Sc. University of Dhaka, Bangladesh, 2011

M.Sc. University of Dhaka, Bangladesh, 2013

M.S. University of Texas at El Paso, USA, 2015

A dissertation submitted in partial fulfillment of the requirements  
for the degree of Doctor of Philosophy in Optics & Photonics  
CREOL, The College of Optics & Photonics  
at the University of Central Florida  
Orlando, Florida

Summer Term

2020

Major Professor: Xiaoming Yu

©2020 Arifur Rahaman

## **ABSTRACT**

Ultrashort-pulsed lasers have been used for high precision processing of a wide range of materials including dielectrics, semiconductors, metals, and polymers/polymer composites, enabling numerous applications ranging from micromachining, photonics to life sciences. However, there are challenges when applying this technology in the industry, which requires scale and throughput different from lab use. The goal of this research is to understand how ultrafast laser pulses interact with thin polymers/polymer composite materials and develop a method that is efficient for ultrafast laser processing of these materials. It is a common practice in industrial applications to run the laser at a high repetition rate and hence high average power. However, the heat accumulation under such processing conditions will deteriorate the processing quality, especially for polymers, which typically have a low melting temperature. An analytical solution for two-dimensional modeling of the temperature distribution has been presented and the solution is used to understand the effect of laser parameters on ultrafast laser processing of polypropylene (PP), which is an important polymer for both scientific and industrial applications. Laser cutting experiments are carried out on PP sheets to correlate with the theoretical calculation. This study shows that in laser cutting, the total energy absorbed in the material and the intensity are two important figures of merit to predict the cutting performance. It is found that heat accumulation can be avoided by a proper choice of the processing conditions and the optical properties (i.e. reflectance, transmittance, and absorptance) are important parameters to control processing with ultrafast lasers.

To determine the reflectance, transmittance, and absorptance, time-resolved, single-shot measurements are performed in ultrafast laser interaction with polypropylene for a wide range of laser pulse energies. The absorptance during the ultrafast laser interaction with polymers is divided

into the different linear and non-linear effective absorption channels and the absorption mechanism of ultrafast laser interaction with polymers in near-infrared wavelength are explained with a model that takes into account different effective absorption channels and suggests that the non-linear absorption originates from vibrational overtone/combination absorption.

The enhancement of the absorptance has been investigated for efficiently processing thin polymers with ultrafast lasers by changing pulse duration. It is suggested from this study that the intense shorter pulse (167 fs) is more efficient for surface processing as most of the energy absorbed at the surface due to the strong nonlinear absorption, while a longer pulse (1000 fs) is more efficient for bulk processing for polymers.

The results are useful for designing and controlling ultrafast laser processing of polymers and optimizing laser process parameters for the most efficient processing of polymers.

To My Parents, Brother, and my lovely Wife

## ACKNOWLEDGMENT

At first, I would like to express my gratitude and thanks to my supervisor **Dr. Xiaoming Yu**. I am truly grateful to him, not only as a supervisor but also as a mentor. His constant guidance, valuable suggestions, encouragement, innovative ideas, and new experimental techniques were the driving force behind this research work. He has taught me the art of quality research and independent thinking. I am thankful to him for everything he has done for me and helping me to do this work.

It is my great pleasure to express my gratitude to my co-supervisor **Dr. Aravinda Kar**. His enthusiasm and devotion to work have made a deep impression on me. I am truly grateful to him for offering much advice during our weekly meetings and analytical solutions. I would like to thank him for his suggestions, innovative ideas, and continuous encouragement in my research.

I would like to express my gratitude to **Dr. M.J. Soileau, Dr. Stephen Kuebler, and Dr. Ranganathan Kumar** for their time and suggestions, and for being a member of my thesis committee.

I would like to pay my special thanks to my groupmates **Dr. Xinpeng Du, Boyang Zhou, and He Cheng** for their help and supportive company during my research work.

Finally, I would like to express my gratitude to my lovely wife for her help, support, and encouragement in every aspect of my life; and to my parents, sisters, and brother, who raised me and trusted me with their endless love.

# TABLE OF CONTENT

LIST OF FIGURES .....	xi
LIST OF TABLES .....	xvii
CHAPTER 1: BACKGROUND.....	1
1.1 Introduction.....	1
1.2 Generation of ultrashort laser pulses.....	2
1.3 Interaction of ultrashort laser pulse with solid material.....	5
1.4 Ultrafast laser processing of polymers.....	8
1.5 Challenges to process polymer with an ultrashort pulse.....	10
1.6 Ultrafast laser pulse shaping .....	13
1.7 Polypropylene sample .....	14
1.7 Motivations & Objectives .....	15
1.9 References.....	18
CHAPTER 2: ANALYTICAL SOLUTION TO A 2D TRANSIENT THERMAL MODEL .....	22
2.1 Introduction.....	22
2.1 Thermal modeling.....	23
2.2 Spatial and Temporal profile of the ultrashort laser pulses .....	24
2.3 Development of the thermal model and derivation of the analytical solution .....	26
2.4 Solution of Heat Conduction Model (HCM) .....	28



2.5 Outputs from the model .....	34
2.6 References.....	38
CHAPTER 3: THERMAL EFFECTS OF ULTRAFAST LASER INTERACTION WITH POLYPROPYLENE.....	40
3.1 Introduction.....	40
3.2 Experimental studies.....	41
3.3 Results and discussion .....	42
3.4 Summery.....	52
3.5 References.....	53
CHAPTER 4: TIME-RESOLVED MEASUREMENTS OF ULTRAFAST LASER INTERACTION WITH POLYPROPYLENE.....	54
4.1 Introduction.....	54
4.2 Experimental setup.....	56
4.3 Experimental Results .....	58
4.4 Model and Discussion.....	61
4.5 Summery.....	65
4.6 References.....	66
CHAPTER 5: MECHANISMS OF ULTRAFAST LASER INTERACTION WITH OPAQUE AND TRANSPARENT POLYPROPYLENE.....	69
5.1 Introduction.....	69
5.2 Experimental design.....	71

5.3 Experimental Results to compare opaque and transparent PP .....	72
5.4 Model and discussion.....	77
5.5 Self-phase modulation (SPM) responsible for wavelength shift .....	82
5.6 Summary .....	84
5.7 References.....	85
5.8 Appendix.....	88
 CHAPTER 6: PULSE-TO-PULSE EVALUATION OF OPTICAL PROPERTIES IN ULTRAFAST LASER PROCESSING OF POLYPROPYLENE.....	 92
6.2 Introduction.....	92
6.2 Experimental setup.....	93
6.3 Effect of 1 <sup>st</sup> pulse and 2 <sup>nd</sup> pulse during ultrafast interaction.....	95
6.4 Theoretical Analysis .....	100
6.5 Summery .....	105
6.6 References.....	106
 CHAPTER 7: EFFECT OF PULSE DURATION IN FRONT AND BACK SURFACE PROCESSING OF TRANSPARENT POLYPROPYLENE.....	 109
7.1 Introduction.....	109
7. 2 The spatial and temporal distortion of ultrashort pulse .....	110
7.3 The effect of pulse duration on ultrafast laser interaction .....	113
7.4 Field enhancement and the back surface damage .....	118

7.5 Effect of the pulse duration on optical properties .....	122
7.6 Theoretical analysis and discussion .....	124
7.7 Summary .....	127
7.8 References .....	128
<b>CHAPTER 8: CONCLUSIONS</b> .....	<b>130</b>
8.1 Conclusions .....	130
8.2 Future works .....	133
Appendix: Publications .....	136

## LIST OF FIGURES

Figure 1.1: Intensity of the periodic pulse train resulting from the sum of N laser modes of equal magnitudes and phases.....	4
Figure 1.2: Femtosecond laser interactions with dielectrics, the conventional view of pulsed laser-material interactions (left column) and the hypothesis for molecular vibrational absorption mechanism .....	6
Figure 1.3: Publications on the ultrafast laser to process polymers with different pulse duration and wavelengths (data complied mostly from ref. [35]).....	9
Figure 1.4: Optical absorption of materials with different wavelengths .....	10
Figure 1.5: Potential energy diagram for a vibration overtone or combination absorptions with C-H vibrational excitation.....	11
Figure 1.6: Characteristic peaks of different elements, Opaque PP (left) and transparent PP (right) in the secondary ion mass spectroscopic spectrum.....	14
Figure 2.1: Schematic of ultrashort pulse laser heating model in cylindrical coordinates with boundary conditions at four locations as BC1, BC2, BC3, and BC4 at the upper and lower surfaces, the center of the cylinder and $r = R_c$ , respectively.....	24
Figure 2.2: Results from the thermal model for various laser parameters, (a) radially symmetric temperature distribution at the surface of the workpiece, $z = 0$ , and (b) axial distribution of temperature at the center of the laser beam, $r = 0$ , to examine the maximum depth of the workpiece that can be vaporized using different laser parameters.....	35
Figure 2.3: 2D contour plot of temperature distribution in the workpiece, showing isotherms to indicate the removal of materials above the isotherm of vaporization temperature marked by 601 K contour.....	36

Figure 2.4: Temperature distribution over time for different energies at the surface of the workpiece ( $z = 0, r = 0$ ) and the decomposition temperature of PP indicated by a horizontal dash line, (a) heat accumulation with different pulses and (b) heat accumulation with 2  $\mu\text{J}$  pulse energy. .... 37

Figure 3.1: Schematics of the experimental setup for laser cutting. .... 41

Figure 3.2: Effect of different pulse repetition rates on the laser cutting process for different pulse energies with the same average powers, showing a variety of cut quality such as partial-depth cutting, through cutting and burning of the workpiece. .... 43

Figure 3.3: Microscopic examination of the cut quality, (a) illustration of heat accumulation at a high (1 MHz) repetition rate, (b) optical microscopic images of laser cut PP sheets at 1 MHz and 100 kHz with the same average power 1.5 W and (c) SEM images of the sheets in (b) for analyzing the cut quality at a higher magnification. .... 44

Figure 3.4: Comparison between the experimental kerf profile and the model result obtained at the cutting speed of 20 mm/s with a laser of pulse energy 20  $\mu\text{J}$  and 100 kHz repetition rate. .... 44

Figure 3.5: A process parameter map containing theoretical isotherms and experimental results to delineate different physical effects such as through cut and burning observed during the interaction between the ultrafast laser and PP workpiece. .... 45

Figure 3.6: Estimation of absorptivity by fitting the theoretical results to experimental data on partial cut depths at  $r = 0$  for different cutting speeds. .... 47

Figure 3.7: Experimental data for the depth of the cavity formed during laser cutting at different speeds and repetition rates, showing that the cut depths follow the same trend as a function of absorbed intensity. .... 48

Figure 3.8: Comparison between the experimental data for the material removal rate as a function of absorbed average power during laser cutting and the corresponding linear trend predicted by an overall energy balance model. ....	51
Figure 4.1: Schematic for experimental set up for time-resolved measurement .....	57
Figure 4.2: PD signals observed on the oscilloscope (a) Incident, reflected, and transmitted signal for 20- $\mu$ J pulse energy. The signals are scaled by 6.5%, 10%, and 100%, respectively. Shaded region for each of the signals represents the FWHM integrated area. The inset shows the linearity of the PDs (only PD 1 is shown here). (b) The signal detected by PD 2 for different pulse energies. (c) Second peaks with different pulse energies.....	59
Figure 4.3: Reflectance (R), transmittance (T), and absorptance (A) of PP sheet as a function of laser fluence. ....	60
Figure 4.4: (a) Fitting of the experimental results using Eq. 4.2. The laser intensity used in this experiment can be divided into three regions (Region I, II and III). Damage observed by (b) optical and (c) scanning electron microscopy (SEM) at corresponding intensities 9.4 (A), 94.1 (B), 378.3 (C) and 658.2 (D) $\text{PW}/\text{m}^2$ shown in (a). ....	62
Figure 4.5: Absorptance, $A$ of impure PP sample is determined from the transmittance, $T$ , and the specular reflection measurement, $R_s$ of PP sample by using a spectrophotometer (Cary 500). ...	63
Figure 5.1: Schematic for experimental set up for measuring optical properties of ultrafast laser interaction with transparent material .....	71
Figure 5.2: Damage observed by scanning electronic microscopy (SEM) on the surface of opaque (top row) and transparent (bottom row) PP sample with different fluences.....	73
Figure 5.3: (a) SEM images of the damage in opaque (top) and transparent (bottom) surface, and its corresponding damage profile on the surface of the material. (b-d) Cross-sectional analysis of	

transparent PP sample with FIB (focused ion beam) milling, which is irradiated with pulse energy 20 $\mu$ J.....	75
Figure 5.4: Reflectance, transmittance, and absorptance for transparent PP sample are $R_{tr}$ , $T_{tr}$ , and $A_{tr}$ , respectively and $R_{op}$ , $T_{op}$ , and $A_{op}$ for opaque PP, respectively, as functions of laser fluence and intensity .....	76
Figure 5.5: The multipole reflection is considered as an inclined laser beam that is irradiated on the sample. ....	78
Figure 5.6: (a) Fitting of the experimental results for opaque PP sample and transparent PP sample. The laser intensity used in this experiment can be divided into three regions (Region I, II, and III). ....	80
Figure 5.7: Absorptance, $A$ , of transparent PP sample is determined from the transmittance, $T$ , and the specular reflectance measurement, $R_s$ , by using linear spectroscopic measurement. ....	81
Figure 5.8: Schematic of the temporal Gaussian pulse.....	83
Figure 5.9: The wavelength shifting with various intensity at different slope values of the intense temporal pulse.....	84
Figure 6.1: Experimental set up for measuring the optical properties of ultrafast laser interaction with transparent PP .....	94
Figure 6.2: Damage A, B, C, and D (scanning electronic microscopy (SEM) images at the left) are irradiated with single pulse and damages E, F, G, and H (SEM images at the left) are irradiated with a pair of the identical pulse. The damage profiles are shown beside each of the damages..	96
Figure 6.3: Cross-sectional analysis of transparent PP sample with Focused Ion Beam (FIB) milling, which is irradiated at pulse energy 80 $\mu$ J .....	98
Figure 6.4: Surface damage with a single pulse (top) and double pulse (bottom) with different peak fluences .....	99

Figure 6.5: Reflectance (R), transmittance (T), and absorptance (A) as a function of peak fluence for 1 <sup>st</sup> pulse (circular data point) and 2 <sup>nd</sup> pulse (star data points) in double pulse case with the delay 1 ms. ....	100
Figure 6.6: Fitting of the experimental results of 167 fs for transparent PP sample. The laser intensity used in this experiment can be divided into three regions (Region I, II, and III) .....	102
Figure 6.7: Absorptance, A, of transparent PP sample is determined from the linear spectroscopic measurement. ....	104
Figure 7.1: (a) spatial distribution, and (b) temporal distribution of the peak intensity of the ultrafast laser with pulse duration 167 fs. ....	111
Figure 7.2: 3D representation of the peak intensity distribution of ultrafast laser during propagation through the transparent PP Sample. ....	112
Figure 7.3: Experimental verification for double peaks with different heights , experimental setup in the left and camera images shown in right with and without sample .....	113
Figure 7.4 : The front surface damages the transparent PP sample with different pulse durations (i.e. 167, 371, 710, and 1000 fs) for a wide range of pulse energies (1 $\mu$ J to 100 $\mu$ J).....	114
Figure 7.5: The back surface damages of the transparent PP sample with different pulse durations(i.e. 167, 371, 710, and 1000 fs) for a wide range of pulse energies(1 $\mu$ J to 100 $\mu$ J). ....	115
Figure 7.6: (a) Determining (a) damage area from optical microscopic images for the different pulse durations(i.e. 167, 371, 710, and 1000 fs) and (b) the damage threshold peak intensity with different pulse durations (i.e. 167, 371, 710, and 1000 fs). ....	116
Figure 7.7: The damage threshold peak fluence/intensity with different pulse durations .....	116
Figure 7.8: Comparing theoretical and experimental damaged area as a function of (a) peak fluence and (b) peak intensity.....	117
Figure 7.9: Front and back surface damage with 1000 fs pulse duration. ....	118



Figure 7.10: Electric fields at the entrance and back surface of the polymer surface. An incident angle is considered at a normal incident .....	119
Figure 7.11: Determining the beam diameter at the front and the back surface from experimental damage diameter .....	120
Figure 7.12: Camera image of the beam diameter at the entrance surface and the exit surface.	121
Figure 7.13: (a) Reflectance (R), (b) transmittance (T), and (c) absorptance (A) as a function of laser fluences with different pulse durations (i.e. 167 fs, 371 fs, 710 fs, and 1000 fs).....	123
Figure 7.14: The multipole reflection is considered as an inclined laser beam that is irradiated on the transparent PP sample .....	124
Figure 7.15: The experimental results of (a) transmittance and (b) absorptance ( $A = 1 - R - T$ ) for different pulse durations (i.e. 167 fs, 371 fs, 710 fs, and 1000 fs) are fitted with the theoretical calculation. ....	126
Figure 8.1: Experimental set up for measuring the optical properties of ultrafast laser interaction with transparent PP for multi-pulses.....	133
Figure 8.2: A microfluidic channel fabricated with ultrafast laser .....	134
Figure 8.3: Experimental set up for optical sensing in laser material processing applications ..	135

**LIST OF TABLES**

Table 1: Thermophysical properties of PP [14-16] and laser irradiation parameters for thermal modelling ..... 34

# CHAPTER 1: BACKGROUND

## 1.1 Introduction

Ultrafast lasers have been used widely for both fundamental research and practical applications since they were developed in the early 1980s [1, 2]. For materials processing, ultrafast lasers offer precision, flexibility, and robustness that are not easily achieved by other laser sources [3, 4]. These characteristics are enabled fundamentally by the short pulse duration, high peak power, and non-thermal interaction with a wide range of materials (e.g. metals, glasses, semiconductors, polymers, and ceramics). Ultrafast lasers generate ultrashort pulses in the range of femtoseconds to a few tens of picoseconds, a timescale that is shorter than the thermal equilibrium time in most materials. Ultrafast lasers have been used to process varieties of materials [5-7] and various types of material processing including laser drilling [8], cutting [9], surface hardening [10], polishing [11,12], cleaning [13] and micro/nano machining [14,15]. Ultrafast lasers interact with different materials based on the mechanism of laser energy absorption. In semiconductors and dielectrics, laser excitation may lead to non-thermal phase transformations induced by the transient modification of interatomic bonding when a high concentration of free electrons is promoted across the bandgap [16]. In materials that have a large bandgap (such as dielectrics and some semiconductors), the excited electrons can absorb the laser energy and bring the material to the plasma state or even produce the Coulomb explosion, the latter of which is due to charge separation on the surface [17]. The absorption mechanism is different for materials that are opaque, such as metals and some semiconductors at visible to near-infrared wavelengths. In these materials, linear absorption contributes the most to laser energy deposition. However, material processing with ultrashort pulses is quite complicated as different linear and nonlinear

absorption mechanisms are involved during the interaction between the ultrashort pulses and polymers. Therefore, it is still challenging to process polymers with high precision and control due to the dynamic behaviors of the interaction between the ultrashort pulses and polymers.

## 1.2 Generation of ultrashort laser pulses

It is over fifty years since ultrafast laser pulses were first produced by passive mode-locking of a giant-pulse ruby laser by Mocker and Collins [18] in 1965. The generation of the first optical pulses in the picosecond range with Nd: glass laser was realized by DeMaria [19]. Within only two decades since the invention of the laser the duration of the shortest pulse shrunk by six orders of magnitude from the nanosecond regime to the femtosecond regime [20]. Nowadays researchers can generate attosecond pulses, which are three orders of magnitude shorter than femtosecond pulses [21]. Ultrashort pulses can be generated directly from a wide variety of lasers with a wide range of wavelengths. Mode locking techniques are the most important technique for generating ultrafast laser pulses by locking the phases of laser longitudinal modes [22]. A laser can oscillate at many longitudinal modes, with frequencies that are equally separated by the intermodal spacing (the frequency separation between two adjacent modes) according to the relationship [22]

$$\nu = \frac{c}{2l}$$

where  $l$  is the distance between two mirrors (same as the length of the Fabry-Perot interferometer). Considering each of the laser modes as a uniform plane wave propagating in the z-direction with a velocity  $c = c_0/n$ , the total complex wavefunction of the field can be written as

$$E(z, t) = \sum_q A_q e^{i[2\pi\nu_q(t-\frac{z}{c})]}$$

where

$$\nu_q = \nu_o + q\nu; \quad q = 0, \pm 1, \pm 2, \dots \dots \dots$$

is the frequency of mode  $q$  and  $A_q$  is its complex envelope. Here,  $\nu_o$  is the central frequency of the atomic lineshape. After substituting  $\nu_q$  into  $E(z, t)$

$$E(z, t) = A\left(t - \frac{z}{c}\right) e^{i[2\pi\nu_o(t-\frac{z}{c})]}$$

where the complex envelope  $A(t)$  as a periodic function of the period,  $\tau$  is given by

$$A(t) = \sum_q A_q e^{i[\frac{2\pi qt}{\tau}]}$$

and

$$\tau = \frac{1}{\nu} = \frac{2l}{c}$$

For  $N$  modes ( $q = 0, \pm 1, \dots \dots N = 2n + 1$ ), whose complex coefficients are all equal,  $A_q = A$ .

$A(t)$  may take the form of periodic narrow pulses, if the magnitudes and phases of the complex coefficients  $A_q$  are properly chosen. Then

$$A(t) = A \sum_{q=-n}^n e^{i[\frac{2\pi qt}{\tau}]}$$

After some algebraic manipulations  $A(t)$  can be written as

$$A(t) = A \frac{\sin(\frac{N\pi t}{\tau})}{\sin(\frac{\pi t}{\tau})}$$

Therefore, the optical intensity is given by

$$I(z, t) = |A|^2 \frac{\sin^2[N\pi(t - z/c)/\tau]}{\sin^2[\pi(t - z/c)/\tau]}$$

The shape of the mode-locked laser pulse train is dependent on the number of modes  $N$ , which is proportional to the atomic linewidth  $\Delta\nu$ . The pulse duration  $t_{on} = \frac{1}{\Delta\nu}$  is inversely proportional to the atomic linewidth  $\Delta\nu$ , and therefore large  $\Delta\nu$  can generate a very narrow pulse. Although the calculation given above is derived for the special case in which modes have equal amplitudes and phases, calculations based on more realistic situations yield similar results [22]. Methods for mode-locking in a laser cavity can be classified as active and passive mode-locking. Inactive mode-locking, typically an external signal is used to induce a modulation of the light in the cavity, whereas passive mode-locking relies on an optic element in the laser cavity which causes self-modulation of the light.

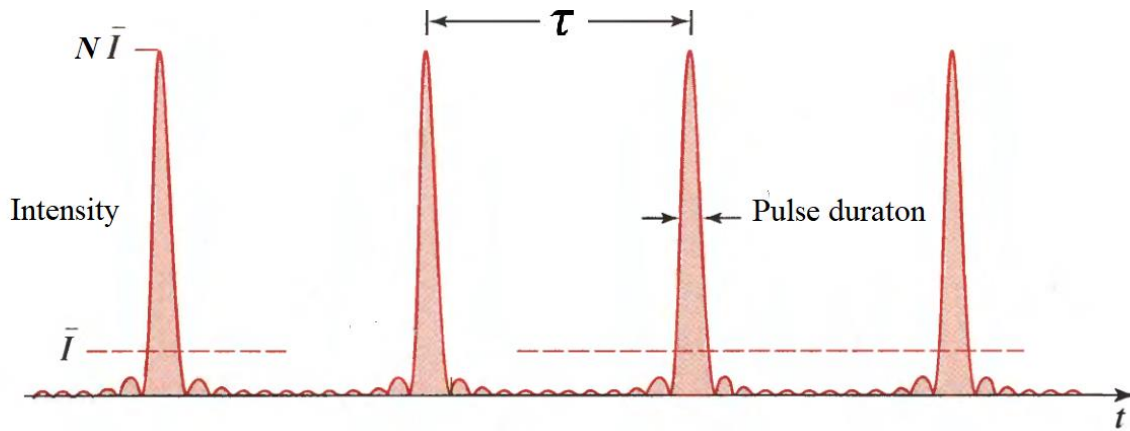


Figure 1.1: Intensity of the periodic pulse train resulting from the sum of  $N$  laser modes of equal magnitudes and phases

Figure 1.1 shows the intensity of the periodic pulse train resulting from the sum of  $N$  laser equal magnitudes and phases. The duration of each pulse is  $N$  times smaller than the period  $\tau$  and peak intensity of that pulse is  $N$  times greater than the mean intensity. Although mode-locking is

the most common technique for generating ultrashort pulses, other approaches exist, for example, strong electro-optic phase modulation and subsequent compression of continuous-wave lasers [23].

The generation of ultrashort laser pulses has been covered in several review articles [24, 25]. Amplification of ultrashort pulses is important for material processing because of high pulse energies, typically higher than a few micro-joules, are needed to induce significant material modification. Ultrashort pulse amplification is typically achieved by a technique called ‘chirped pulse amplification’ (CPA), which increases the energy of ultrashort laser pulses while avoiding damaging the gain media by temporally stretching the input, low-energy pulses from femtoseconds to picoseconds or longer. An ultrashort pulse can be stretched in time using a pair of gratings that are arranged so that the low-frequency component (longer wavelength) of the laser pulse travels a shorter path than the high-frequency component. The laser pulse, therefore, becomes positively chirped with a pulse duration much longer than the original pulse. Then the stretched pulse is safely introduced to the gain medium and amplified by a factor of  $10^6$  or more. Finally, the amplified laser pulse is recompressed back to the original pulse width through introducing negative chirp, the reversal process of pulse stretching, and therefore pulse energy and peak power can be increased.

### 1.3 Interaction of ultrashort laser pulse with solid material

The combination of high power and short pulse duration puts the interaction of ultrashort laser light with solid material into a unique interaction regime. The main distinction comes from the way that laser energy is absorbed. Figure 1.2 illustrates the conventional view ultrafast laser

interaction with dielectrics in the left column, where the laser-induced processes can be roughly divided into three groups [26].

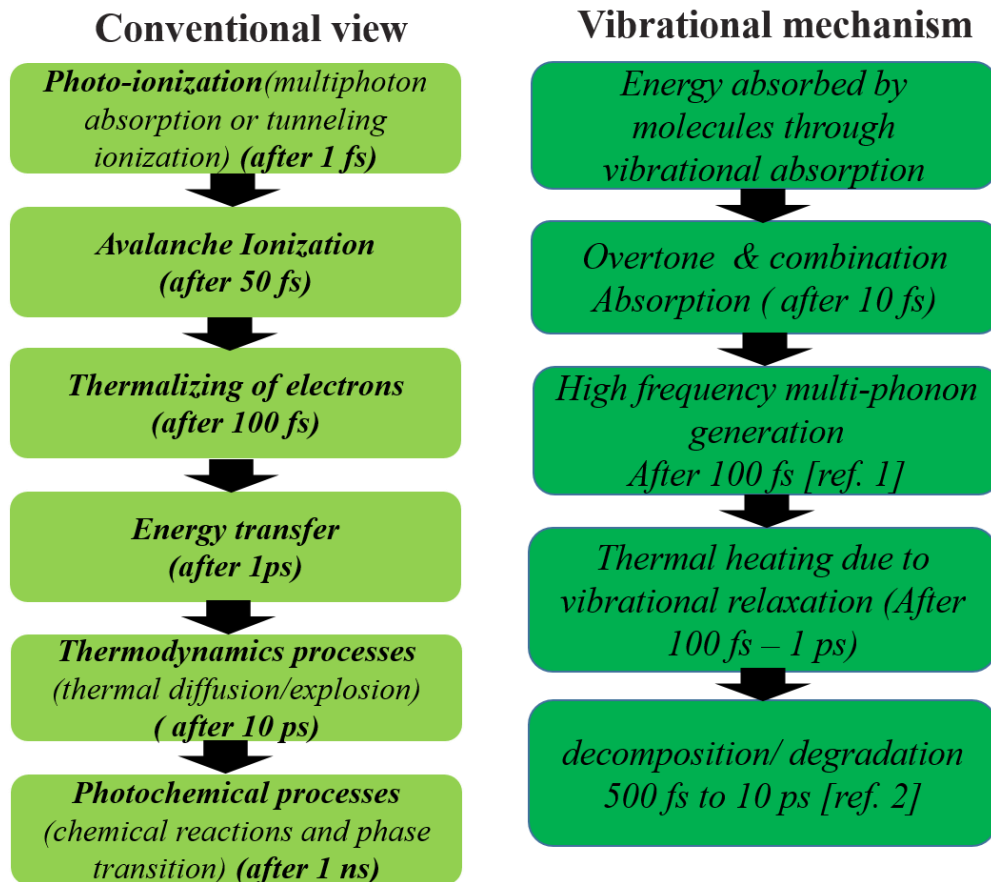


Figure 1.2: Femtosecond laser interactions with dielectrics, the conventional view of pulsed laser-material interactions (left column) and the hypothesis for molecular vibrational absorption mechanism

Optically active electronics states after laser excitation and the initial ultrafast processes occurring in response to the electronic excitation (such as multiphoton and avalanche ionization); rapid non-equilibrium phase transformations originated from energy transfer from excited electrons to atomic vibrations, and the subsequent cooling and solidification. When a femtosecond laser pulse with high peak intensity is focused on the material, an optical breakdown can take

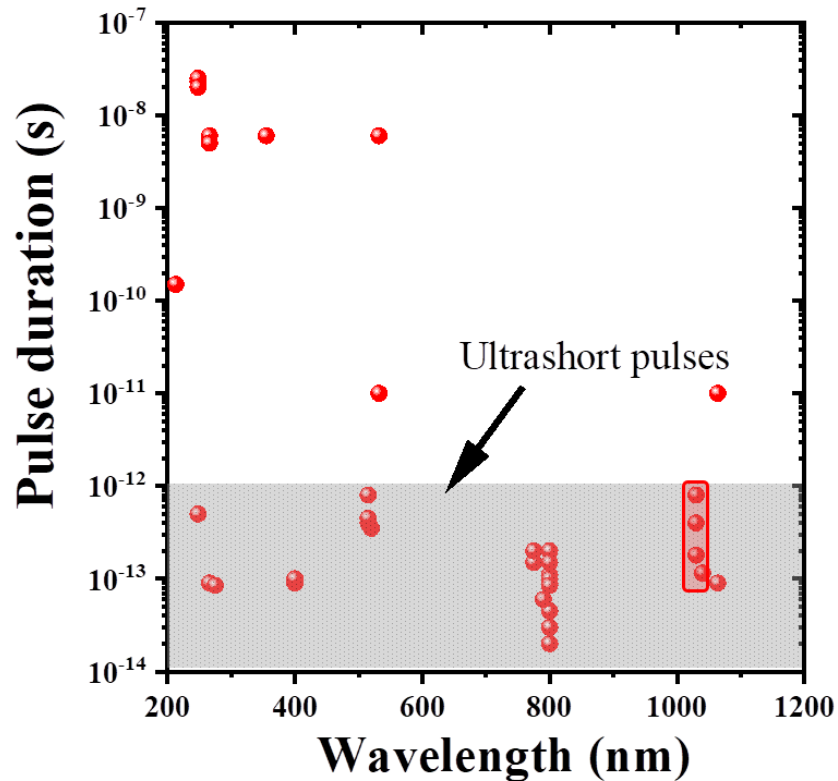


place, resulting in insignificant, and often visible, change to the material. Laser pulse energy is transferred to electrons on a time scale comparable to the duration of the ultrashort pulse. The highly excited electrons thermalize with the ions within tens to hundreds of ps. Material phases change due to melting, vaporization, and solidification occurs on the ns timescale. Unlike the conventional view of the ultrafast laser absorption mechanism, laser energy can be absorbed by the molecules through the vibrational absorption mechanism during the ultrafast laser interaction with dielectrics, especially with polymers. In the case of polymers, vibrational overtone and combination absorption can happen with 10 fs that lead to high-frequency multi-phonon generation with after 100 fs [27]. Thermal heating occurs due to the vibration relaxation within the time scale of 100 fs to 1 ps, that thermal heating accelerates to the decomposition/degradation process of polymers within the time scale of 500 fs to 10 ps [28].

The ablation behavior of any material is primarily influenced by its optical (e.g., reflectance, linear and nonlinear absorptance, and transmittance) and thermal (e.g., thermal diffusivity, conductivity) properties [17]. The absorption mechanism is different for materials that are opaque or transparent to the laser wavelength. For opaque materials (such as metals and some semiconductors at visible to near-infrared wavelengths), the main contribution is linear absorption, whereas nonlinear processes (e.g., multiphoton and avalanche ionization) play an important role in a transparent material. After receiving ultrashort pulse irradiation, electrons and lattice will achieve thermal equilibrium, and the transfer time of the electronic energy to the lattice is between picoseconds to nanoseconds [29]. The energy transferred to the lattice can increase the lattice temperature to the boiling or vaporization temperature, resulting in material ablation, damage, or modification of the refractive index.

## 1.4 Ultrafast laser processing of polymers

Polymers have a great interest in industrial applications due to unique properties such as lightweight, corrosion resistance, thermal and electrical insulators, easy to design and manufacturing any structures, etc. [30]. Polymers are important industrial materials for various applications including the automobile industry, aircraft structures, bullet-proof covers, packaging, surface protecting coating, scientific equipment, and household items, etc. [31, 32]. After the rise of research on ultrafast laser processing, researchers have focused on the ultrafast laser processing of polymers [2, 5]. Polymers were one of the first material to be processed with ultrafast laser in 1987 reported by two groups, R. Srinivasan and S. Stuke [33, 34]. Since then researchers have been investigating methods to minimize defects in ultrafast laser processing of polymer for various applications and started exploring various aspects of using ultrafast laser for processing polymers for such applications. In the last two decades, research has been focused on the influences of different types of ultrafast laser and laser parameters on ablated structures. Fig. 1.3 shows some publications on ultrafast laser processing of polymers with different wavelengths and pulse durations. It can be seen that for ultrashort pulses, there are more studies at 800 nm (Ti: Sapphire laser) than  $> 1 \mu\text{m}$ , which is the laser wavelength used in this dissertation. Fig. 1.3 shows that very few publications are reported around 1030 nm wavelength and pulse durations used on these publications are random from 100 fs to 1 ps. In addition, researchers investigated the methods to minimize defects in ultrafast laser processing. Therefore, their studies were mostly to observe the influence of laser type and parameters on accuracy and precision. Therefore, it is required to understand the interaction mechanism of ultrafast laser with polymers in near-infrared (NIR) to have better control in ultrafast laser processing of polymers for scientific and industrial applications.



## 1.5 Challenges to process polymer with an ultrashort pulse

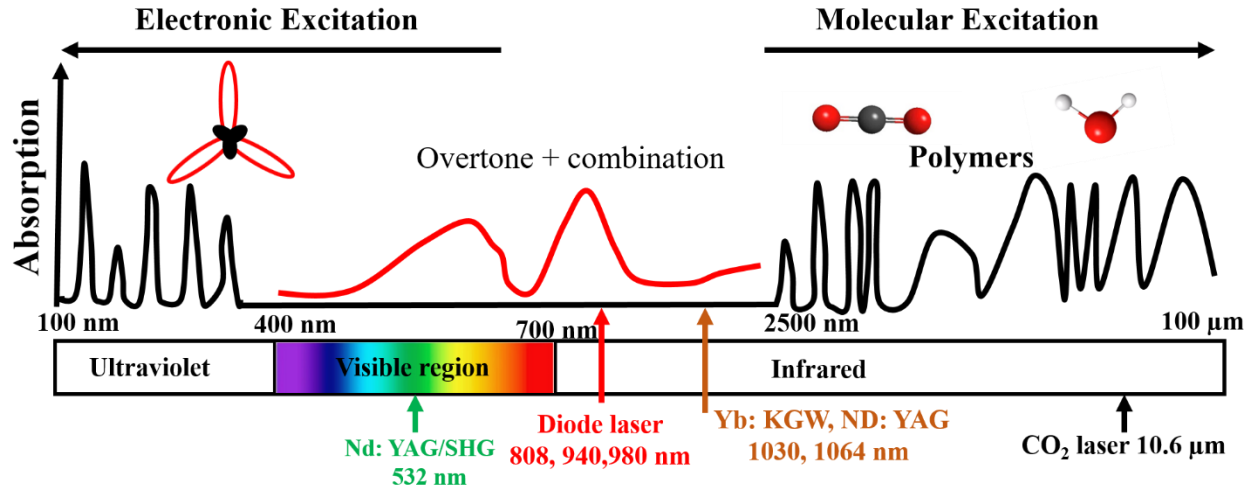


Figure 1. 4: Optical absorption of materials with different wavelengths

Polymers show strong optical absorption in ultraviolet (UV) wavelengths and far-infrared, and less absorption at visible to near-infrared (N-IR) wavelengths. Therefore, initial studies were performed mostly with UV wavelengths [45, 46]. However, because of the high peak intensity of ultrafast laser pulses, ultrafast lasers enable the processing of polymeric material via nonlinear optical interaction in near-infrared wavelengths [47]. Polymers can be processed with linear optical absorption in far-ultraviolet (122-200 nm) light, for example, with excimer laser with wavelengths 193 nm (ArF) or 248 nm (KrF), and in far-infrared light, for example, with CO<sub>2</sub> lasers. Fig. 1.4 shows the optical absorption of polymer with different wavelengths and absorption mechanisms with different wavelengths. Due to the high bandgap of the most to the polymers, it is quite impossible to have electronic and molecular excitation with NIR wavelengths. Therefore, the absorption mechanism of ultrafast laser processing in NIR wavelengths are quite complicated.

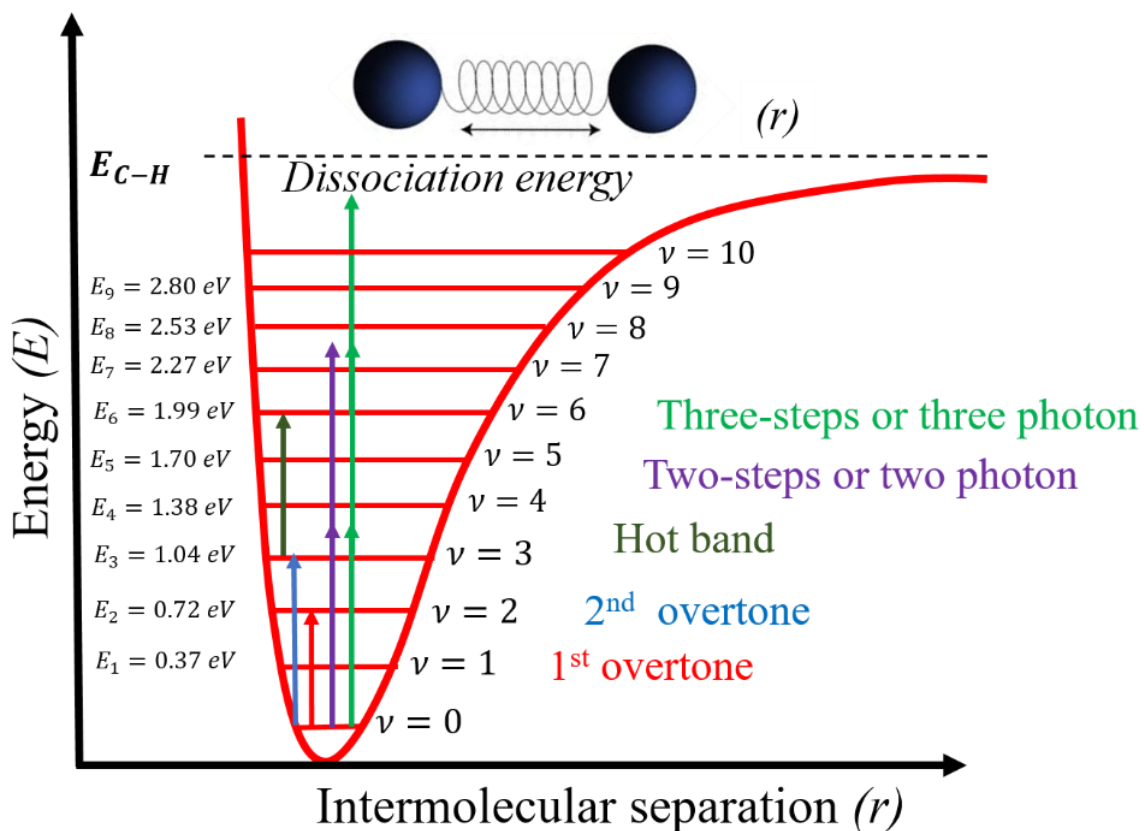


Figure 1.5: Potential energy diagram for a vibration overtone or combination absorptions with C-H vibrational excitation

The mechanism of ultrafast laser interaction with polymers in the near-infrared wavelength is still challenging to understand due to complicated linear and nonlinear absorption mechanisms. Absorption in polymers at wavelengths ranging from 800 to 2500 nm, which corresponds to wavenumber 12,500 to 4000  $\text{cm}^{-1}$ , is considered to be based on vibrational overtone and combination absorption [48]. The exact mechanism of ultrafast laser interaction with polymers remains controversial among researchers in the near-infrared wavelengths. In a molecule, fundamental vibrational frequencies correspond to transition from  $\nu = 0$  to  $\nu = 1$ , but overtones occur when a vibrational mode is excited from  $\nu = 0$  to higher frequency levels as shown in Fig.

1.5. The vibrational combination absorptions arise from the sharing of near-infrared energy between two and more fundamental or overtone absorptions.

Although polymers are the first material to be processed with ultrafast laser, there are still challenges, which are summarized below:

1. Shorter pulses create more vaporization leading to the formation of plasma plume, which can reduce the quality of the processed material as polymers have a very low decomposition temperature.
2. The absorption mechanism of polymers varies with different intensity/fluence, which needs to be well characterized to have accurate predictions on the processing results.
3. Most polymers have a very large bandgap. Therefore, photons need to have high energy to be absorbed by the electronic transition. However, the process mechanism of polymers is quite complicated with near-infrared (NIR) wavelengths.
4. It is common practice to run the laser at a high repetition rate and hence high average power to make ultrafast laser processing compatible with the scale and throughput needed for industrial use. However, heat accumulation under such processing conditions will deteriorate the processing quality, especially for polymers that typically have a low melting temperature.
5. The photochemical and photothermal process might dominate for some polymers during their process with ultrafast lasers, which might give some unpredictable process conditions.

## 1.6 Ultrafast laser pulse shaping

Temporal pulse shaping has been demonstrated as an important technique frequently used in ultrafast applications [49]. The interaction of ultrashort laser pulses with the material can be modified by pulse shaping to enhance the absorptance in polymers. Enhanced absorptance in polymers has many applications in such as laser micromachining (e.g., cutting, drilling, and waveguide, etc.), surface hardening, polishing, and surface cleaning.

Ultrafast pulse shaping has been used to tailor laser-matter interactions, which enhances the phenomena induced by ultrafast laser pulses. The study of the laser-matter interactions of ultrashort laser pulse with controlled pulse width and separation between two pulses has been shown in different articles [50, 51]. Depending on the pulse width and separation between two pulses, dynamics of the laser matter interaction may change and the properties of the ablated species may vary. Several experimental and theoretical investigations have been carried out for double-pulse ultrafast laser ablation (ULA). Spyridaki *et al.* [52] demonstrated that double-pulse ablation produces a much smoother ablation crater than single-pulse ablation. In that study, the first pulse produced a molten layer, and energy coupling efficiency increased for the second pulse. Hu *et al.* [53] observed ion emission increases with the separation of two pulses. In their study, it was suggested that the enhanced absorption of the second pulse is responsible for this increase in ion emission. Stoian *et al.* showed a significant improvement in the quality of ultrafast laser micromachining of dielectrics by using temporally shaped pulse trains with subpicosecond separation [51]. These various studies have provided a basic understanding of the dynamics of laser-matter interactions, but most of the studies deal with ultrafast laser ablation of dielectrics and metals, while for polymers this is a largely unexplored field.

## 1.7 Polypropylene sample

Polymers have a great interest in industrial applications due to unique properties such as lightweight, corrosion resistance, thermal and electrical insulators, easy to design and manufacturing any structures, etc.. Polypropylene (PP) is an important industrial material, which has a wide range of applications including packaging for consumer products (medical industry), plastic parts for various industries (including automotive industry), laboratory, and special devices like hinges, household products, battery cases, and fabrics [54].

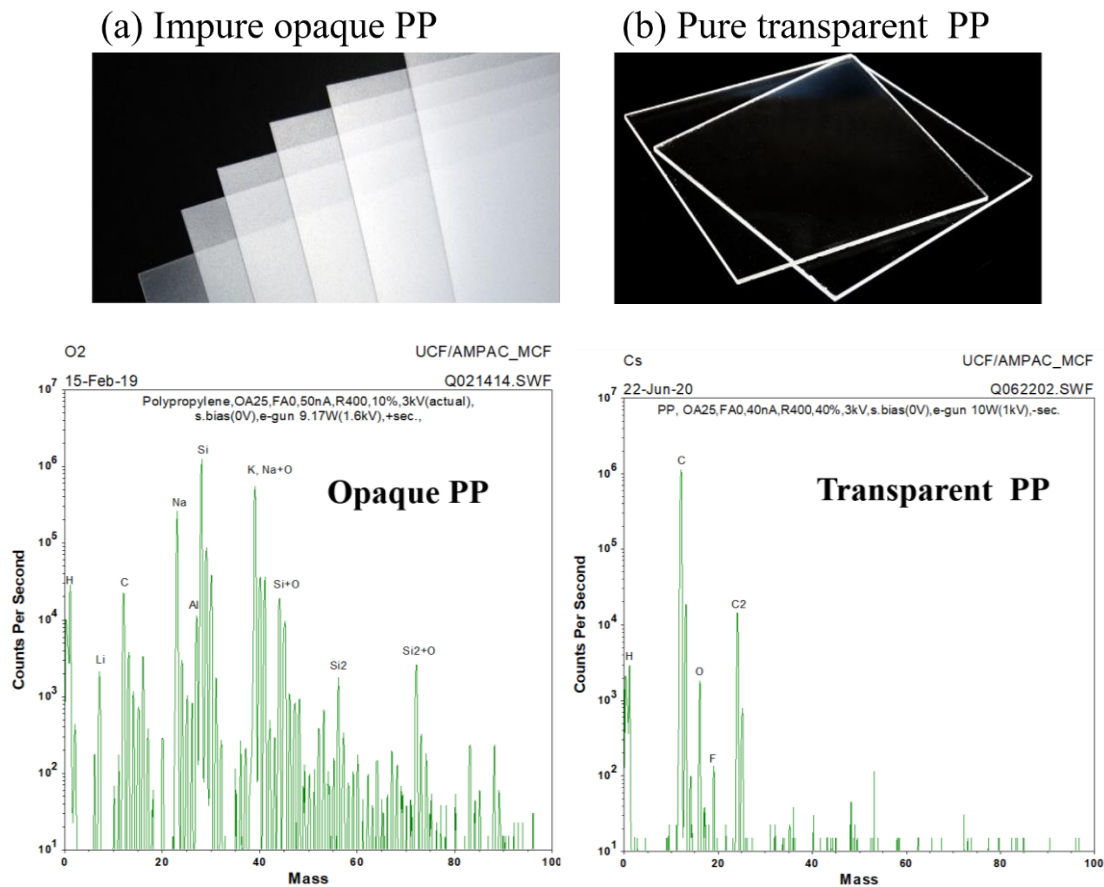


Figure 1.6: Characteristic peaks of different elements, Opaque PP (left) and transparent PP (right) in the secondary ion mass spectroscopic spectrum.



Different kinds of PP are commercially available, which can be divided into two groups based on optical properties, Opaque and transparent, where opaque mostly reflects and absorbs irradiate laser energy as opaque PP contains different pigments, which can be of organic or inorganic structure. However, the mechanism of ultrafast laser processing is different for transparent and opaque PP. In this study, both opaque (mostly reflects and absorbs irradiate laser energy) and transparent PP (PP301440, Goodfellow, which is mostly transparent, around 90% of visible light) samples are used. Fig. 1.6 shows the image of the opaque PP (left) and the transparent PP (right), and the characteristics peaks of different elements containing. The opaque PP sheet is 300  $\mu\text{m}$  thick containing small amounts of several impurities Si, C, Li, Na, Al, K, and SiO<sub>2</sub> that exhibited characteristic peaks in the secondary ion mass spectroscopic spectrum and the transparent PP sheet is 450  $\mu\text{m}$  thick, has almost no impurity.

## 1.7 Motivations & Objectives

Modern ultrafast lasers are compact, tabletop systems capable of delivering short, powerful pulses at a high repetition rate, high peak power, and other unique characteristics. Interaction of ultrashort pulses with the material has many features that make ultrashort laser systems attractive for a variety of applications. In the ultrashort time duration, the energy of the laser pulse is concentrated both in space and time, resulting in an extremely high laser intensity at the focal spot up to the order of  $\text{TW}/\text{cm}^2$  [55]. At such high intensity, the absorbed laser energy can disassemble any kind of material lattices, even the strongest bond in the diamond lattice [56]. Another feature of the femtosecond laser is called “cold ablation”, which is associated with the extremely short pulse duration. In this case, the pulse duration is too short to let heat diffuse far from the center of interaction, and the energy of the laser pulse can turn directly to plasma. Therefore, femtosecond

lasers can remove material only at the focal spot with a minimum heat affect zone, and high-speed processing is possible with proper tuning of laser processing parameters for enhanced energy coupling [57]. However, due to the complex nature of ultrafast laser – solid interaction, it is not clear how the temporal profile of ultrafast laser pulses affects energy transfer during the interaction between the ultrashort laser pulses and polymers with near-infrared wavelength. This motivates us to investigate the dynamics behavior of ultrafast laser interaction with polymers, with the aim to optimize energy transfer using pulse shaping techniques.

The interaction of ultrashort pulses with polymers has many features that make ultrashort laser systems attractive for a variety of applications. However, heat accumulation and plasma plume in the material at high pulse repetition rates can deteriorate the processing quality, especially for polymers which typically have a low melting temperature. The underlying physics to efficiently cut polymers with ultrafast lasers is important, especially for flexible electronics consisting of polymeric substrates. There is a lack of understanding of how to efficiently process polymers using ultrashort pulsed lasers. Energy loss due to light scattering must be accounted for and compensated. It has been shown that temporal pulse shaping is a powerful tool to enhance energy transfer. However, applying this technique for processing polymeric imposes new challenges, which are the main focus of this research.

The main purpose of this research is to develop energy-efficient ultrafast laser processing for polymeric/thin composite materials by ultrafast pulse shaping. The objectives of this research are summarized as follows:

- Review literature on ultrafast laser processing of polymeric material and identify the state of art and knowledge gaps in the laser processing of polymers.
- Develop a model to analyze the thermal effect of the laser processing of polymeric material.

- Design experiments to study the absorptance of polymeric/thin composite materials for femtosecond laser pulses
- Obtain time-averaged and time-resolved data on reflection (specular, diffused) and transmission, and calculate the absorbance
- Use the experimentally determined absorptance in the model and obtain processing conditions under which laser energy can be coupled most efficiently to the material
- Design and construct ultrafast laser pulse shaping experiments and determine the most efficient intensity/fluence region for polymer processing.
- Perform laser cutting and drilling experiments to verify the modeling results and achieve the energy-efficient processing of polymers.

## 1.9 References

1. W. Sibbett, A. A. Lagatsky, and C. T. A. Brown, “The development and application of femtosecond laser systems,” *Opt. Express* **20**(7), 6989-7001 (2012).
2. K. Sugioka and Y. Cheng, “Review Ultrafast Lasers – reliable tools for advanced material processing,” *Light Sci. Appl.* **3**(4), 1-12 (2014).
3. R. R. Gattass and E. Mazur, “Femtosecond laser micromachining in transparent materials,” *Nat. Photonics* **2**, 219-225 (2008).
4. S. Mishra and V. Yadava, “Laser Beam Micro-Machining (LBMM) – A review,” *Opt. Lasers Eng.* **73**, 89 -122 (2015).
5. K. C. Phillips, H. H. Gandhi, E. Mazur, and S. K. Sundaram, “Ultrafast laser processing of materials: a review,” *Adv. Opt. Photonics* **7**(4), 684 - 712 (2015).
6. M. Malinauskas, A. Žukauskas, S. Hasegawa, Y. Hayasaki, V. Mizeikis, R. Buividas and S. Juodkazis, “Ultrafast laser processing of materials: from science to industry,” *Light Sci. Appl.* **5**(8), 1-14 (2016).
7. S. Nolte, M. Will, J. Burghoff, and A. Tünnermann, “Ultrafast laser processing: New options for three-dimensional photonic structures,” *J. Mod. Opt.* **51**(16 -18), 2533 - 2542 (2004).
8. X. Zhao and Y. C. Shin, “Femtosecond laser drilling of high - aspect ratio microchannels in glass,” *Appl. Phys. A* **104**(2), 713–719 (2011).
9. A. N. Fuchs, M. Schoeberl, J. Tremmer, and M. F. Zaeh, “Laser cutting of carbon fiber fabrics,” *Phys. Procedia* **41**, 372–380 (2013).
10. A. K. Nath, A. Gupta, and F. Benny, “Theoretical and experimental study on laser surface hardening by repetitive laser pulses,” *Surf. Coat. Technol.* **206**(8-9), 2602–2615 (2012).
11. M. Malinauskas, A. Žukauskas, S. Hasegawa, Y. Hayasaki, V. Mizeikis, R. Buividas, and S. Juodkazis, “Ultrafast laser processing of materials: from science to industry,” *Light: Sci. Appl.* **5**(8), e16133 (2016).
12. L. L. Taylor, J. Xu, M. Pomerantz, T. R. Smith, J. C. Lambropoulos, and J. Qiao, “Femtosecond laser polishing germanium,” *Opt. Express* **9**(11), 4165–4177 (2019).
13. . T. Ersoy, T. Tunay, M. Uğuryol, G. Mavili, and S. Akturk, “Femtosecond laser cleaning of historical paper with sizing,” *J. Cult. Herit.* **15**(3), 258–265 (2014).
14. R. R. Gattass and E. Mazur, “Femtosecond laser micromachining in transparent materials,” *Nat. Photonics* **2**(4), 219–225 (2008).
15. W. Jia, Y. Luo, J. Yu, B. Liu, M. Hu, L. Chai, and C. Wang, “Effects of high-rate femtosecond laser micromachining on the physical and chemical properties of polylactide (PLA),” *Opt. Express* **23**(21), 26932–26939 (2015).
16. M. Hase, P. Fons, K. Mitrofanov, A.V. Kolobov, J. Tominaga, “Femtosecond structural transformation of phase - change materials far from equilibrium monitored by coherent phonons,” *Nat. Commun.* **6**, 8367 (2015).

17. N.M. Bulgakova, R. Stoian, A. Rosenfeld, I.V. Hertel, and E.E.B. Campbell, “Electronic transport and consequences for material removal in ultrafast pulsed laser ablation of materials,” *Phys. Rev. B*, **69**, 054102 (2004).
18. H. Mocker, R. Collins, “Mode competition and self – locking effects in a Q – Switched Ruby laser”, *Appl. Phys. Lett.* **7**, 270 (1965).
19. A. J. DeMaria, D. A. Stetser, H. Heyman, “Self modelocking of lasers with saturable absorbers”, *Appl. Phys. Lett.* **8**,174(1966).
20. M. Wollenhaupt, A. Assion, and T.Baumert, “Short and ultrashort laser pulses”, *Springer Handbook of Lasers and Optics*, Springer, 1047-1094, (2012).
21. P.M. Paul, E. S. Toma, P. Breger, G. Mullot, F. Audebert, Ph. Balcou, H. G. Muller, P. Agostini, “Observation of a train of attosecond pulses from high harmonic generation”, *Science* **292**, 1689–1692 (2001).
22. B.E. A. Saleh and M. C. Teich, “Fundamental of photonics”, Wiley, (2007).
23. A. M. Weiner, “Ultrafast optical pulse shaping: A tutorial”, *Optical Communications* **284**, 3669-3692, (2011).
24. P.M.W. French, “The generation of ultrashort laser pulses”, *Rep. Prog. Phys.* **58**, 169–267 (1995).
25. J. D. Simon, “Ultrashort light pulses”, *Rev. Sci. Instrum.* **60**, 3597–3624 (1989).
26. M. V. Shugaev, C. Wu, O. Armbruster, A. Naghilou, N. Brouwer, D. S. Ivanov, T. J.-Y. Derrien, N. M. Bulgakova, W. Kautek, B. Rethfeld, and L. V. Zhigilei, “Fundamental of ultrafast laser – material interaction,” **41**, 12,960-964, (2016).
27. Y. Hosokawa, M. Yashiro, T. Asahi, and H. Masuhara, Photothermal conversion dynamics in femtosecond and picosecond discrete laser etching of Cu-Phthalocyanine amorphous film analysed by ultrafast UV-VIS absorption spectroscopy,” *J. Photochem. Photobio. A: Chem.*, **142**, 197-207 (2001).
28. S. R. Cain, F. C. Burns, C. E. Otis, B. Braren, “Photothermal description of polymer ablation: Absorption behavior and degradation time scales,” *Jour. of Appl. Phys.* **72**, 5172(1992).
29. J. Kruger, and W. Kautek, “Ultrashort Pulse Laser interaction with dielectrics and polymers”, *Adv Polym Sci.*,**168**, 247-289, (2004).
30. S. R.-Kumar, B. Lies, X. Zhang, H. Lyu, H. Qin, “ Laser ablation of polymer: a review,” *Polym. Int.* **68**, 1391-1401 (2019).
31. L. Persano, A. Camposo, C. Tekmen, and D. Pisignano, “Industrial upscaling of spinning and applications of polymer nanofibers,” *Macromol. Mater. Eng.* **298**, 504-520 (2013).
32. Clarinval AM, Halleux J (2005) Classification of biodegradable polymers. In: Smith R (ed) *Biodegradable polymers for industrial applications*. Woodhead, Cambridge.
33. R. Srinivasan, E. Sutcliffe, and B. Braren, “Ablation and etching of poly-methylmethacrylate by very short (160 fs) ultraviolet (308 nm) laser pulses,” *Appl. Phys. Lett.* **51**, 1285-1287 (1987).

34. S. Kuper and M. Stuke, "Femtosecond UV excimer laser ablation" *Appl. Phys. B*, **44**, 199-204 (1987).
35. M. Terakawa, "Femtosecond laser processing of biodegradable polymers," *Appl. Sci.* **8**, 1123 (2018).
36. C. D. Marco, S. M. Eaton, R. Suriano, S. Turri, M. Levi, R. Ramponi, G. Cerullo, and R. Osellame, "Surface properties of femtosecond laser ablated PMMA," *ACS Appl. Mater. Interfaces* **2**, 2377-2384 (2010).
37. S. Baudach, J. Bonse, and W. Kautek, "Ablation experiments on polyimide with femtosecond laser pulses," *Appl. Phys. A* **69**, S395-S398 (1999).
38. Z. B. Wang, and M. H. Hong, "Femtosecond laser ablation of polytetrafluoroethylene (Teflon) in ambient air," *Jour. of Appl. Phys.* **93**, 6375 (2003).
39. S. Darvishi, T. Cubaud, and J. P. Longtin, "Ultrafast laser machining of tapered microchannels in glass and PDMS," *Opt. and Lasers in Eng.* **50**, 210-214(2012).
40. H. W. Choi, J. K. Johnson, J. Nam, D. F. Farson, and J. Lannutti, "Structuring electrospun polycaprolactone nanofiber tissue scaffolds by femtosecond laser ablation," *J. Laser Appl.* **19**, 225-231(2007).
41. W. Y. Yeong, K. P. Lim, G. K. L. Ng, L. P. Tan, F. Y. C. Boey, and S. S. Venkatraman, "Annealing of biodegradable polymer induced by femtosecond laser micromachining," *Adv. Eng.* **12**, B89-B93(2010).
42. H. W. Wang, C. W. Cheng, C. W. Li, H. W. Chang, P. H. Wu, and G. J. Wang, "Fabrication of pillared PLGA microvessel scaffold using femtosecond laser ablation," *Int. J. Nanomed* **7**, 1865-1873.
43. D. G. Papazoglou, D. Abdollahpour, and S. Tzortzakis, "Ultrafast electron and material following femtosecond filamentation induced excitation of transparent solids," *Appl. Phys. A* **114**, 161-168 (2014).
44. H. Schmidt, J. Ihlemann, B. Wolff-Rottke, K. Luther, and J. Troe, "Ultraviolet laser ablation of polymers: spot size, pulse duration, and plume attenuation effects explained," *Jour. of Appl. Phys.* **83**, 5458-5468(1998).
45. S. Kuper, and M. Stuke, "Femtosecond UV excimer laser ablation," *Appl. Phys. B* **44**, 199-204(1987).
46. R. Srinivasan, E. Sutcliffe., and E. Braren, "Ablation and etching of polymethacrylate by very short (160 fs) ultraviolet (308 nm) laser pulses," *Appl. Phys. Lett.* **51**, 1285-1287 (1987).
47. F. Sima, K. Sugioka, R. M. Vazquez, R. Osellame, L. Kelemen, and P. Ormos, "Three-dimensional femtosecond laser processing for lab-on-a-chip applications," *Nanophotonics* **7**, 613-647(2018).
48. K. B. Bec and C. W. Huck, "Breakthrough potential in Near-Infrared spectroscopy : spectra simulation. A review of recent developments," *Front. Chem.* **7**, 48 (2019).
49. S. Dinda, S N. Bandyopadhyay, and D. Goswami, "Rapid programmable pulse shaping of femtosecond pulses at the MHz repetition rate" *OSA Continuum*, **2**, 1386-1400 (2019).

50. F. Bourquard, J. P. Colombier, M. Guillermin, A. S. Loir, C. Donnet, R. Stoian, and F. Garrelie, “Temporal pulse shaping effects on aluminium and boron ablation plumes generated by ultrashort pulsed laser ablation and analyzed by time- and space-resolved optical spectroscopy” *Appl. Sur. Sci.*, **258**, 9374-9378 (2012).
51. R. Stoian, M. Boyle, A. Thoss, A. Rosenfeld, G. Korn, I.V Hertel, and E. E. B. Campbell “Laser ablation of dielectrics with temporally shaped femtosecond pulses” *Appl. Phys. Lett.* **80**, 353-355 (2002).
52. M. Spyridaki, E. Koudoumas, P. Tzanetakis, and C. Fotakis, “Temporal pulse manipulation and ion generation in ultrafast laser ablation of silicon”, *Appl. Phys. Lett.*, **84**, 1474 (2003).
53. Z. Hu, “Mechanism for the ablation of Si <111> with pairs of pairs of ultrashort laser pulses”, *Appl. Phys. Lett.*, **90**, 1131910 (2007).
54. A. Rahaman, A. Kar, and X. Yu, “ Time resolved measurements of optical properties in ultrafast laser interaction with polypropylene” *Opt. Express*, 28(2), 2640-2648(2020).
55. A. Riveiro, F. Quintero, F. Lusquiños, J. del Val, R. Comesaña, M. Boutinguiza, and J. Pou, “Laser cutting of Carbon Fiber Composite materials”, “Manufacturing Engineering Society International Conference”, Spain, **13**, 388-395, (2017).
56. WS Lau, WB Lee, Pang SQ Pulsed Nd: YAG laser cutting of carbon fibre composite materials. *CIRP Ann* **39**,179–182, (1990).
57. C. B. Schaffer, A. Brodeur, J. F. García, E. Mazur, J. F. Garcia, and E. Mazur, “Micromachining bulk glass by use of femtosecond laser pulses with nano joule energy,” *Opt. Lett.*, **26**, 2, 93–95, (2001).

## CHAPTER 2: ANALYTICAL SOLUTION TO A 2D TRANSIENT THERMAL MODEL

(This Chapter is mostly based on a theoretical calculation of the Author's publication: Arifur Rahaman, Aravinda Kar, and Xiaoming Yu, "Thermal effects of ultrafast laser interaction with polypropylene," *Opt. Express* **27**(4), 5764-5783 (2019).)

### 2.1 Introduction

Mathematical models of the thermal effects can be divided into two types: analytical and numerical models. Analytical models yield analytical solutions, representing a direct relation between laser parameters and the heating process. The analytical solutions are, however, difficult to obtain for complex systems, but can be determined under certain simplifying assumptions to gain insights into the physical processes. These solutions can be used as a guideline for optimizing the laser processing parameters. There have been several studies on analytical modeling in recent years. B.S. Yilbas *et al.* [1] introduced a one-dimensional model using the kinetic theory approach for short-pulse laser processing. Their study compared the predictions of kinetic energy theory with predictions from other models for laser pulses with pulse durations in the range of  $10^{-9}$  to  $10^{-11}$  s. Khenner *et al.* [2] obtained an analytical solution to the classical heat conduction problem of solid film irradiated by repetitive laser pulses using the method of separation of variables. B.S. Yilbas and Pakdemirli [3] derived a closed-form solution of the temperature distribution originated from repetitively pulsed laser heating using the perturbation method. They utilized the hyperbolic heat conduction equation derived from the Boltzman equation and its general solution, which was obtained using the Fourier transform method [4]. However, previous solutions to the hyperbolic heat conduction equation are limited in one – dimensional (1D) spatial and temporal dimensions. A. K. Nath *et al.* [5] presented a 1D model for the temperature profiles during heating and cooling cycles in repetitively pulsed laser irradiation, and the effects of processing parameters, such as



laser power, beam diameter, scan speed, pulse duration, repetitive rate, and duty cycle, on laser surface hardening were analyzed. Stuart *et al.* [6] developed a general theoretical model of laser interaction with dielectrics, which was shown to be in good agreement with experimental data in the short pulse regime. A generalized analytical solution was presented by Tung T. Lam [7] for electron and lattice temperature profiles in a metallic film exposed to ultrashort laser pulses using the superposition and the Fourier transform method in conjunction with the solution structure theorems. Chen *et al.* [8] presented the two-dimensional analytical solutions of repetitively pulsed laser heating of aluminum alloy and investigated the effects of processing parameters on the temperature distribution. They showed that millisecond pulse duration can avoid the plasma effect. Taylor *et al.* [9] established a three-dimensional, two-temperature model (TTM) and a heat-accumulation model based on classical heat generation and conduction equations to evaluate their efficacy and efficiency in simulating non-thermal ablation and heat accumulation during multi-pulse femtosecond laser processing of silicon.

## 2.1 Thermal modeling

A 2D transient Heat Conduction Model (HCM) and its analytical solution that describe ultrashort laser pulse interaction with the workpiece is discussed in this section. The model is based on the geometry shown in Fig. 2.1, which depicts laser pulses irradiating on a piece of thin solid material. The workpiece is considered in an axisymmetric cylindrical coordinate system.

The absorbed laser energy is assumed to be converted to heat instantaneously. The material removal is modeled as a sublimation process where heated solid materials directly turn into vapor because the liquid phase exists only for a very short period [10]. For laser processing of polymeric

composite materials, chemical degradation can occur before the temperature reaches the vaporization temperature [11]. For simplification, chemical degradation is treated in the same way as sublimation because both processes absorb energy and produce gases [12].

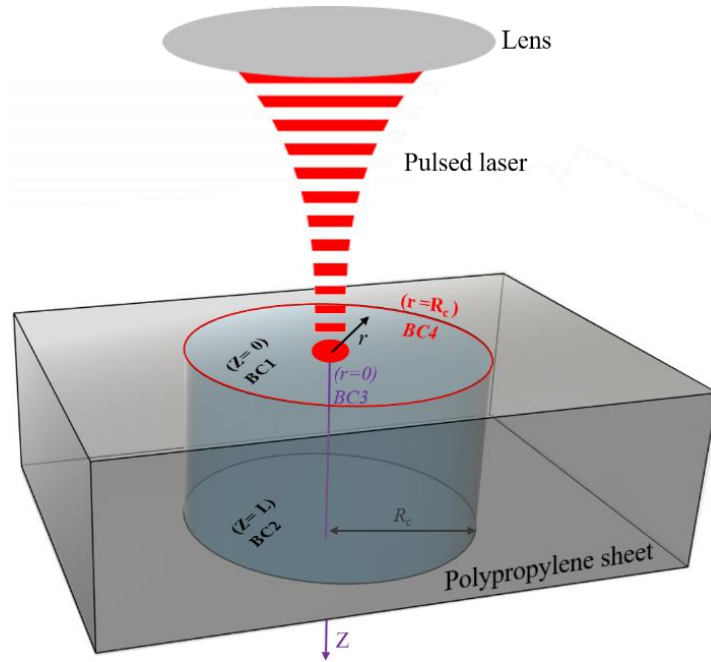


Figure 2.1: Schematic of ultrashort pulse laser heating model in cylindrical coordinates with boundary conditions at four locations as BC1, BC2, BC3, and BC4 at the upper and lower surfaces, the center of the cylinder and  $r = R_c$ , respectively.

## 2.2 Spatial and Temporal profile of the ultrashort laser pulses

The intensity  $I(\mathbf{r}, t)$  of the Gaussian beam is given by

$$I(r, t) = AI_o e^{-\frac{2r^2}{\omega_o^2}} \varphi(t)$$

where  $A$  is the absorptivity of the workpiece;  $r$ ,  $\omega_o$  and  $I_o = \frac{4E}{\pi\omega_o^2 t_{on}}$  are the radial coordinate, radius at the waist of the laser beam, and the peak intensity, respectively.  $\varphi(t)$  is the laser pulse

shape function, describing the temporal profile of the laser pulse as a function of time  $t$ . In this study  $\varphi(t)$  is assumed to be a triangular shape given by

$$\varphi(t) = \begin{cases} \frac{t - (n_p - 1)t_p}{t_{pk}} & \text{for } (n_p - 1)t_p \leq t \leq (n_p - 1)t_p + t_{pk} \\ \frac{(n_p - 1)t_p + t_{on} - t}{t_{on} - t_{pk}} & \text{for } (n_p - 1)t_p + t_{pk} < t \leq (n_p - 1)t_p + t_{on} \\ 0 & \text{for } (n_p - 1)t_p + t_{on} < t \leq (n_p - 1)t_p + t_p \end{cases}$$

where  $n_p = 1, 2, 3, 4, \dots$  are the total number of pulses irradiating on the sample,  $t_{on}$  and  $t_p$  are the laser pulse on time and period (pulse on plus pulse off time), respectively, and  $t_{pk}$  is the time at which the pulse reaches its peak intensity.

The femtosecond laser system of this study produces Gaussian pulses that were used at the pulse length of 200 fs for cutting experiments. This pulse shape can be approximated fairly well as a triangular pulse due to the high peak power and short pulse length of the Gaussian pulse. The error in the energy of a triangular pulse compared to the Gaussian pulse is 6.44% for both types of a pulse having the same pulse length of 200 fs, where the Gaussian pulse length is defined as the full width at half maxima. Different pulse shapes would affect the temporal distribution of the temperature. Replacing the Gaussian pulse with a triangle pulse simplifies the thermal analysis considerably without introducing a significant error due to the small error in the pulse energy. The effects of different pulse shapes on the temperature distribution can be studied by representing the pulse shape function through the variable  $\phi(t)$  in this model.

## 2.3 Development of the thermal model and derivation of the analytical solution

The 2D transient HCM is solved analytically in the cylindrical coordinates for a semi-infinite medium irradiated by a pulsed laser beam. As shown in Fig. 2.1, the origin of the coordinate system lies on the top surface of the workpiece and coincides with the center of the laser beam. The radial ( $r$ ) axis is parallel to the workpiece surface and the axial ( $z$ ) axis points to the bottom surface of the workpiece. Here, both  $r$  and  $z$  are considered as finite.

Considering different thermal conductivities in the  $r$  and  $z$  directions, the governing heat conduction equation is given by [13]

$$\frac{\partial^2 T(r,z,t)}{\partial r^2} + \frac{1}{r} \frac{\partial T(r,z,t)}{\partial r} + k_{zr} \frac{\partial^2 T(r,z,t)}{\partial z^2} = \frac{1}{\alpha_r} \frac{\partial T(r,z,t)}{\partial t} \quad (2.1)$$

where  $k_{zr} = \frac{k_z}{k_r}$  is the ratio of thermal conductivity along  $z$ ,  $k_z$ , to the thermal conductivity along  $r$ ,  $k_r$ , and  $\alpha_r = \frac{k_r}{\rho c_p}$  is the thermal diffusivity along the  $r$ -direction. Here,  $\rho$  and  $c_p$  are the density and specific heat of the workpiece, respectively. Since the temperature of the substrate varies during the cutting process, the temperature-dependent thermophysical properties and absorptivity affect the temperature distribution in the material as cutting progress. Due to the paucity of high-temperature data, however, thermal models are generally developed with constant values of the properties as a first-order approximation to the laser-material interaction process.

The boundary conditions (BCs) and the initial condition (IC) are

$$BC1: -k_z \frac{\partial T(r,z,t)}{\partial z} \Big|_{z=0} = AI(\mathbf{r}, t)$$

$$BC2: -k_z \frac{\partial T(r,z,t)}{\partial z} \Big|_{z=L} = h(T_L - T_\infty)$$

$$BC3: \left. \frac{\partial T(r,z,t)}{\partial r} \right|_{r=0} = 0$$

$$BC4: T(R_c, z, t) = T_\infty$$

$$IC : T(r, z, 0) = T_o$$

where  $h$  is the heat transfer coefficient of the air-workpiece boundary at the lower ( $z = L$ ) surface. Here,  $T_\infty$  and  $T_o$  are the ambient temperature and initial temperature of the workpiece, respectively, and  $T_L = T(r, L, t)$  and  $R_c$  is the characteristic radius of the cylinder, which is determined in the appendix.

To reduce the dependency of the solution on a potentially large number of dimensional parameters, dimensionless parameters are used which are defined as

$$\begin{aligned} r^* &= \frac{r}{\omega_o} & z^* &= \frac{z}{\omega_o} \\ t^* &= \frac{\alpha_r t}{\omega_o^2} & T^*(r^*, z^*, t^*) &= \frac{T(r,z,t) - T_\infty}{T_o - T_\infty} \end{aligned}$$

where  $t^*$  is known as the Fourier number. Applying the dimensionless parameters to Eq. (2.1), BCs and IC, the HCM can be rewritten as

$$\frac{1}{r^*} \frac{\partial}{\partial r^*} \left( r^* \frac{\partial T^*(r^*, z^*, t^*)}{\partial r^*} \right) + k_{zr} \frac{\partial^2 T^*(r^*, z^*, t^*)}{\partial z^{*2}} = \frac{1}{\alpha_r} \frac{\partial T^*(r^*, z^*, t^*)}{\partial t^*} \quad (2.2)$$

which is subject to the following BCs and IC with dimensionless parameters

$$BC1: \left. \frac{\partial T^*(r^*, z^*, t^*)}{\partial z^*} \right|_{z^*=0} = -\frac{A}{k_z} I(r^*, t^*)$$

$$BC2: \left. \frac{\partial T^*(r^*, z^*, t^*)}{\partial z^*} \right|_{z^*=L^*} = -Bi T^*(r^*, z^*, t^*)|_{z^*=L^*}$$

$$BC3: \left. \frac{\partial T^*(r^*, z^*, t^*)}{\partial r^*} \right|_{r^*=0} = 0$$

$$BC4: T^*(R_c^*, z^*, t^*) = 0$$

$$IC: T^*(r^*, z^*, 0) = T_i$$

where  $Bi = \frac{h\omega_o}{k_z}$  is Biot number,  $T_i = 1$  and  $R_c^* = \frac{R_c}{\omega_o}$ . The method of solving this HCM is outlined in section 2.4 to obtain the following dimensionless temperature distribution in the workpiece

## 2.4 Solution of Heat Conduction Model (HCM)

Eq. (2) is transformed into Eq. (3) by applying the zeroth-order Hankel integral transform for finite media  $\bar{T}^*(\lambda_m^*, z^*, t^*) = \int_0^{R_c^*} r^* J_0(\lambda_m^* r^*) T^*(r^*, z^*, t^*) dr^*$ , where  $\lambda_m^*$  is the m-th eigenvalue,  $m = 1, 2, 3, \dots$ , corresponding to the radial boundary conditions and  $J_0$  is the Bessel function of the first kind of zeroth order. The integral transform also yields an eigenvalue expression,  $J_0(\lambda_m^* R_c^*) = 0$ , which is used to determine m-number of values of  $\lambda_m^*$ .

$$k_{zr} \frac{d^2 \bar{T}^*(\lambda_m^*, z^*, t^*)}{dz^{*2}} - \lambda_m^{*2} \bar{T}^*(\lambda_m^*, z^*, t^*) = \frac{d\bar{T}^*(\lambda_m^*, z^*, t^*)}{dt^*} \quad (2.3)$$

which must satisfy the following BCs and IC

$$BC1: \left. \frac{d\bar{T}^*(\lambda_m^*, z^*, t^*)}{dz^*} \right|_{z^*=0} = -\frac{A}{k_z} \bar{I}(\lambda_m^*, t^*) \quad (2.4)$$

$$BC2: \left. \frac{d\bar{T}^*(\lambda_m^*, z^*, t^*)}{dz^*} \right|_{z^*=L^*} = -Bi \bar{T}^*(\lambda_m^*, z^*, t^*)|_{z^*=L^*} \quad (2.5)$$

$$IC: \bar{T}^*(\lambda_m^*, z^*, 0) = \bar{T}_i(\lambda_m^*) \quad (2.6)$$

The Hankel transformed laser intensity  $\bar{I}(\lambda_m^*, t^*)$  and initial condition  $\bar{T}_i(\lambda_m^*)$  are given by the following expressions:

$$\bar{I}(\lambda_m^*, t^*) = \int_0^{R_c^*} r^* J_0(\lambda_m^* r^*) I(r^*, t^*) dr^* \quad (2.7)$$

$$\bar{T}_i(\lambda_m^*) = \int_0^{R_c^*} r^* J_0(\lambda_m^* r^*) T_i dr^* \quad (2.8)$$

The integral in Eq. (2.7) has a closed form result  $\frac{I_0 \varphi(t^*)}{4} e^{-\frac{\lambda_m^{*2}}{8}}$  when  $R_c^* \rightarrow \infty$ . To utilize this closed form expression in the HCM for obtaining an analytical temperature distribution, the integral in Eq. (2.7) is evaluated numerically for sufficiently large values of  $R_c^*$  and different values of  $\lambda_m^*$  so that the numerical value of the integral matches well with the result of the closed form expression. This approach yielded  $R_c^* = 10.5$  and therefore  $R_c = 193.2 \mu\text{m}$ , which indicates that the PP sheet can be considered radially infinite for radii larger than or equal to 10 times the laser beam radius, i.e.,  $R_c = 10.5 \omega_0$ .

Using Duhamel's theorem on Eq. (2.3), the new governing equation can be rewritten as

$$k_{zr} \frac{d^2 \bar{\psi}^*(\lambda_m^*, z^*, t^*, \tau^*)}{dz^{*2}} - \lambda_m^{*2} \bar{\psi}^*(\lambda_m^*, z^*, t^*, \tau^*) = \frac{d\bar{\psi}^*(\lambda_m^*, z^*, t^*, \tau^*)}{dt^*} \quad (2.9)$$

and the boundary and initial conditions, (4), (5) and (6), can be expressed as

$$BC1: \left. \frac{d\bar{\psi}^*(\lambda_m^*, z^*, t^*, \tau^*)}{dz^*} \right|_{z^*=0} = -\frac{A}{k_z} \bar{I}(\lambda_m^*, \tau^*) \quad (2.10)$$

$$BC2: \left. \frac{d\bar{\psi}^*(\lambda_m^*, z^*, t^*, \tau^*)}{dz^*} \right|_{z^*=L^*} = -Bi \bar{\psi}^*(\lambda_m^*, z^*, t^*, \tau^*) \Big|_{z^*=L^*} \quad (2.11)$$

$$IC: \bar{\psi}^*(\lambda_m^*, z^*, 0, \tau^*) = \bar{T}_i(\lambda_m^*) \quad (2.12)$$

The solution to Eq. (2.9),  $\bar{\psi}^*(\lambda_m^*, z^*, t^*, \tau^*)$ , can be split into the following transient and steady state solutions:

$$\bar{\psi}^*(\lambda_m^*, z^*, t^*, \tau^*) = \bar{\psi}_H^*(\lambda_m^*, z^*, t^*) + \bar{\psi}_{SS}^*(\lambda_m^*, z^*, \tau^*) \quad (2.13)$$

The governing equation for the transient solution can be obtained from Eqs. (2.9) and (2.13):

$$k_{zr} \frac{d^2 \bar{\psi}_H^*(\lambda_m^*, z^*, t^*)}{dz^{*2}} - \lambda_m^{*2} \bar{\psi}_H^*(\lambda_m^*, z^*, t^*) = \frac{d\bar{\psi}_H^*(\lambda_m^*, z^*, t^*)}{dt^*} \quad (2.14)$$

and the boundary and initial conditions for Eq. (2.14) is determined from Eqs. (2.13), (2.10), (2.11)

and (2.12):

$$\left. \frac{d\bar{\psi}_H^*(\lambda_m^*, z^*, t^*)}{dz^*} \right|_{z^*=0} = 0 \quad (2.15)$$

$$\left. \frac{d\bar{\psi}_H^*(\lambda_m^*, z^*, t^*)}{dz^*} \right|_{z^*=L^*} + Bi \bar{\psi}_H^*(\lambda_m^*, z^*, t^*) \Big|_{z^*=L^*} = 0 \quad (2.15)$$

$$\bar{\psi}_H^*(\lambda_m^*, z^*, 0) = \bar{T}_i(\lambda_m^*) - \bar{\psi}_{ss}^*(\lambda_m^*, z^*, \tau^*) \quad (2.17)$$

Similarly, Eqs. (2.9) and (2.13) yield the following governing equation for the steady state solution:

$$\frac{d^2 \bar{\psi}_{ss}^*(\lambda_m^*, z^*, \tau^*)}{dz^{*2}} - \frac{\lambda_m^{*2}}{k_{zr}} \bar{\psi}_{ss}^*(\lambda_m^*, z^*, \tau^*) = 0 \quad (2.18)$$

with the boundary conditions determined from Eqs. (2.13), (2.10) and (2.11) as

$$\left. \frac{d\bar{\psi}_{ss}^*(\lambda_m^*, z^*, \tau^*)}{dz^*} \right|_{z^*=0} = \bar{I}(\lambda_m^*, \tau^*) \quad (2.19)$$

$$\left. \frac{d\bar{\psi}_{ss}^*(\lambda_m^*, z^*, \tau^*)}{dz^*} \right|_{z^*=L^*} + Bi \bar{\psi}_{ss}^*(\lambda_m^*, z^*, \tau^*) \Big|_{z^*=L^*} = 0 \quad (2.20)$$

The solution of Eq. (2.17) can be written as



$$\begin{aligned}
& \bar{\psi}_{ss}^*(\lambda_m^*, z^*, \tau^*) \\
&= C_3 \left[ - \left\{ \frac{Bi \sinh\left(\frac{\lambda_m^*}{\sqrt{k_{zr}}} L^*\right) + \frac{\lambda_m^*}{\sqrt{k_{zr}}} \cosh\left(\frac{\lambda_m^*}{\sqrt{k_{zr}}} L^*\right)}{\frac{\lambda_m^*}{\sqrt{k_{zr}}} \sinh\left(\frac{\lambda_m^*}{\sqrt{k_{zr}}} L^*\right) + Bi \cosh\left(\frac{\lambda_m^*}{\sqrt{k_{zr}}} L^*\right)} \right\} \cosh\left(\frac{\lambda_m^*}{\sqrt{k_{zr}}} z^*\right) \right. \\
&\quad \left. + \sinh\left(\frac{\lambda_m^*}{\sqrt{k_{zr}}} z^*\right) \right]
\end{aligned} \tag{2.21}$$

where  $C_3 = -\frac{A\sqrt{k_{zr}}}{k_z \lambda_m^*} \bar{I}(\lambda_m^*, \tau^*)$ .

Eq. (2.14) is solved by applying the Fourier integral transform

$$\tilde{\psi}_H^*(\lambda_m^*, \gamma_n^*, t^*) = \int_0^{L^*} \cos(\gamma_n^* z^*) \bar{\psi}_H^*(\lambda_m^*, z^*, t^*) dz^* \tag{2.22}$$

where  $\cos(\gamma_n^* z^*)$  is the eigenfunction with  $\gamma_n^*$  as the n-th eigenvalue for  $n = 1, 2, 3, \dots$ , corresponding to the axial boundary conditions. The eigenvalues  $\gamma_n^*$  are determined from the transcendental equation  $\gamma_n^* \tan(\gamma_n^* L^*) = Bi$ .

Eq. (2.14) simplifies to the following first order ordinary differential equation under the Fourier transform (22):

$$\frac{d\tilde{\psi}_H^*(\lambda_m^*, \gamma_n^*, t^*)}{dt^*} + (k_{zr} \gamma_n^{*2} + \lambda_m^{*2}) \tilde{\psi}_H^*(\lambda_m^*, \gamma_n^*, t^*) = 0 \tag{2.23}$$

and the initial condition (2.15) transforms to the following expression:

$$\tilde{\psi}_H^*(\lambda_m^*, \gamma_n^*, 0) = \tilde{T}_i(\lambda_m^*) - \tilde{\psi}_{ss}^*(\lambda_m^*, \gamma_n^*, \tau^*) \tag{2.24}$$

Under this initial condition (2.24), the solution to Eq. (2.23) is

$$\tilde{\psi}_H^*(\lambda_m^*, \gamma_n^*, t^*) = \tilde{\psi}_H^*(\lambda_m^*, \gamma_n^*, 0) e^{-(k_{zr} \gamma_n^{*2} + \lambda_m^{*2}) t^*} \quad (2.25)$$

Applying the inverse Fourier integral transform to Eq. (2.25) and using Eq. (2.13), the solution to Eq. (2.9) can be written as

$$\begin{aligned} \bar{\psi}^*(\lambda_m^*, z^*, t^*, \tau^*) &= \sum_{n=1}^{\infty} \frac{\cos(\gamma_n^* z^*)}{N_F(\gamma_n^*)} \left[ \tilde{T}_i(\lambda_m^*, \gamma_n^*) - \tilde{\psi}_{ss}^*(\lambda_m^*, \gamma_n^*, \tau^*) \right] e^{-(k_{zr} \gamma_n^{*2} + \lambda_m^{*2}) t^*} \\ &+ \bar{\psi}_{ss}^*(\lambda_m^*, z^*, \tau^*) \end{aligned} \quad (2.26)$$

where the normalization constant,  $N_F(\gamma_n^*)$ , for the Fourier transform is given by

$$\frac{1}{N_F(\gamma_n^*)} = \frac{2(\gamma_n^{*2} + Bi^2)}{L^*(\gamma_n^{*2} + Bi^2) + Bi}$$

and

$$\tilde{T}_i(\lambda_m^*, \gamma_n^*) = \int_0^{L^*} \bar{T}_i(\lambda_m^*) \cos(\gamma_n^* z^*) dz^*$$

Duhamel's theorem relates the solution  $\bar{\psi}^*(\lambda_m^*, z^*, t^*, \tau^*)$  to the solution  $\bar{T}^*(\lambda_m^*, z^*, t^*)$  of the original problem in Eq. (2.3) by the following integral

$$\bar{T}^*(\lambda_m^*, z^*, t^*) = \int_0^{t^*} \frac{\partial \bar{\psi}^*(\lambda_m^*, z^*, t^*, \tau^*)}{\partial t^*} d\tau^* \quad (2.27)$$

which yields the Hankel transformed temperature distribution as

$$\begin{aligned} \bar{T}^*(\lambda_m^*, z^*, t^*) &= \bar{\psi}_{ss}^*(\lambda_m^*, z^*, \tau^*) + \sum_{n=1}^{\infty} \frac{\cos(\gamma_n^* z^*)}{N_F(\gamma_n^*)} \tilde{T}_i(\lambda_m^*, \gamma_n^*) e^{-at^*} \\ &- \sum_{n=1}^{\infty} \frac{\cos(\gamma_n^* z^*)}{N_F(\gamma_n^*)} \left[ \tilde{\psi}_{ss}^*(\lambda_m^*, z^*, 0) e^{-at^*} \right. \\ &\left. - \int_0^{t^*} e^{-a(t^* - \tau^*)} \frac{d}{d\tau^*} \{ \bar{\psi}_{ss}^*(\lambda_m^*, \gamma_n^*, \tau^*) \} d\tau^* \right] \end{aligned}$$

(2.28)

where  $a = (k_{zr} \gamma_n^2 + \lambda_m^2)$ . The inverse Hankel transform of this expression yields the temperature distribution  $T^*(r^*, z^*, t^*)$  as given in Eq. (2.29).

$$\begin{aligned}
T^*(r^*, z^*, t^*) &= \sum_{m=1}^{\infty} \frac{J_0(\lambda_m^* r^*)}{N_H(\lambda_m^*)} \bar{\psi}_{ss}^*(\lambda_m^*, z^*, \tau^*) \\
&+ \sum_{m=1}^{\infty} \frac{J_0(\lambda_m^* r^*)}{N_H(\lambda_m^*)} \sum_{n=1}^{\infty} \frac{\cos(\gamma_n^* z^*)}{N_F(\gamma_n^*)} \tilde{T}_i(\lambda_m^*, \gamma_n^*) e^{-at^*} \\
&- \sum_{m=1}^{\infty} \frac{J_0(\lambda_m^* r^*)}{N_H(\lambda_m^*)} \sum_{n=1}^{\infty} \frac{\cos(\gamma_n^* z^*)}{N_F(\gamma_n^*)} \tilde{G}(\lambda_m^*, \gamma_n^*) \int_0^{t^*} e^{-a(t^* - \tau^*)} \frac{d\varphi^*(\tau^*)}{d\tau^*} d\tau^*
\end{aligned}
\tag{2.29}$$

where the normalization constant for the Hankel transform is

$$\frac{1}{N_H(\lambda_m^*)} = \frac{2}{R^{*2} J_1^2(\lambda_m^* R^*)}$$

and

$$\tilde{G}(\lambda_m^*, \gamma_n^*) = \int_0^{L^*} \bar{\psi}_{ss}^*(\lambda_m^*, z^*) \cos(\gamma_n^* z^*) dz^*$$

All other variables in Eq. (2.29) are defined above. Eq. (2.29) yields the dimensional temperature distribution in terms of  $r$ ,  $z$  and  $t$  as

$$T(r, z, t) = (T_o - T_\infty)T^*(r^*, z^*, t^*) + T_\infty \tag{2.30}$$

## 2.5 Outputs from the model

The temperature distributions in polypropylene (PP) sheets due to ultrafast laser irradiation are modeled using the above mentioned analytical solutions where the following thermophysical properties and laser parameters are used.

Table 1: Thermophysical properties of PP [14-16] and laser irradiation parameters for thermal modeling

Properties and Parameters	Value
Thickness of PP workpiece, ( $\mu\text{m}$ )	300
Thermal decomposition temperature, $T_c$ (K)	601
Density of the material, $\rho$ ( $\text{Kgm}^{-3}$ )	946
Thermal conductivity, $k, k_r, k_z$ ( $\text{Wm}^{-1}\text{K}^{-1}$ )	0.22
Thermal diffusivity, $\alpha$ ( $\text{m}^2\text{s}^{-1}$ )	$1.37 \times 10^{-7}$
Specific heat capacity at constant pressure, $C_p$ ( $\text{Jkg}^{-1}\text{K}^{-1}$ )	1920
Heat transfer coefficient, $h$ ( $\text{W}/\text{m}^2\text{K}$ )	100
Pulse duration, $t_{\text{on}}$ (fs)	200
Pulse repetition rate, $N_p$ (MHz)	1
Pulse repetition rate, $N_p$ (kHz)	10, 100
Laser beam radius, $\omega_o$ ( $\mu\text{m}$ )	18.4
Laser Wavelength, $\lambda$ (nm)	1030

Fig. 2.2(a) shows the temperature distributions along the  $r$  direction at the PP surface  $z = 0$  for different pulse energies from  $0.3 \mu\text{J}$  to  $2 \mu\text{J}$ . Here, the pulse repetition rate ( $N_p$ ) and the pulse duration are set to  $1 \text{ MHz}$  and  $200 \text{ fs}$ , respectively. Since the laser intensity is higher at the center of the beam, the maximum temperature is reached at  $r = 0$ . In addition, a higher temperature is attained for larger pulse energies because the input energy to the workpiece increases as the pulse energy is increased. The temperature distributions along the  $z$ -direction at the center of the laser beam  $r = 0$  are shown in Fig. 2.2(b) for pulse energies from  $0.3 \mu\text{J}$  to  $2 \mu\text{J}$ . In the model, the laser beam is absorbed in the surface ( $z = 0$ ) where the highest temperature is reached for each pulse energy. The temperature decreases as the depth increase, because input energy decreases with increasing depth.

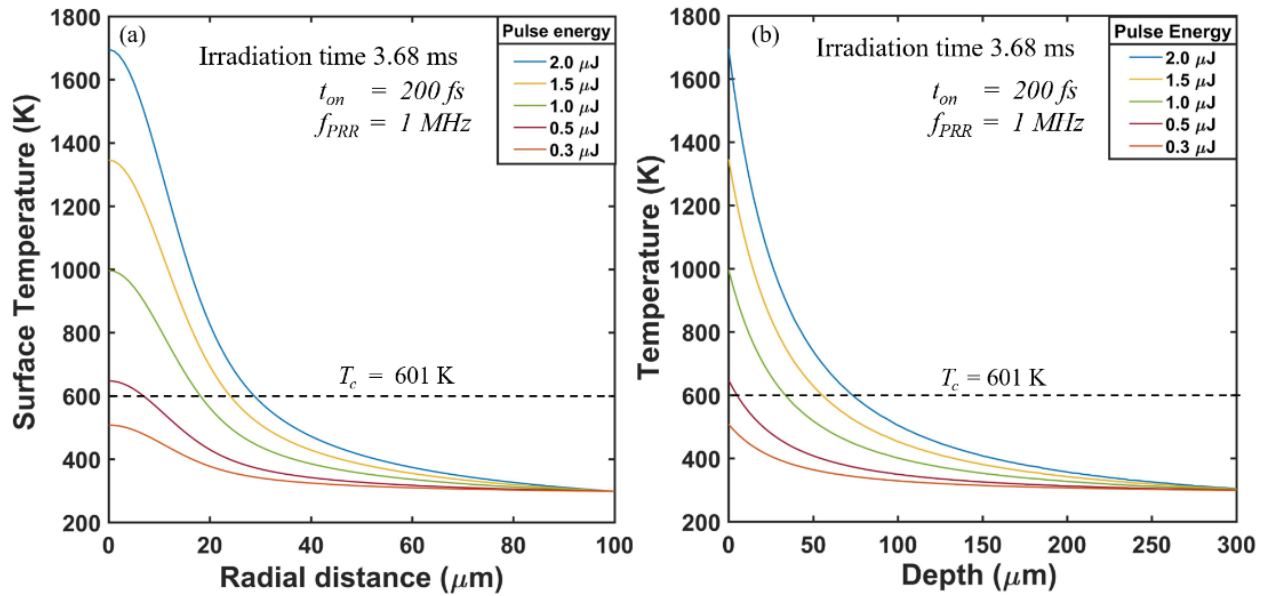


Figure 2.2: Results from the thermal model for various laser parameters, (a) radially symmetric temperature distribution at the surface of the workpiece,  $z = 0$ , and (b) axial distribution of temperature at the center of the laser beam,  $r = 0$ , to examine the maximum depth of the workpiece that can be vaporized using different laser parameters.

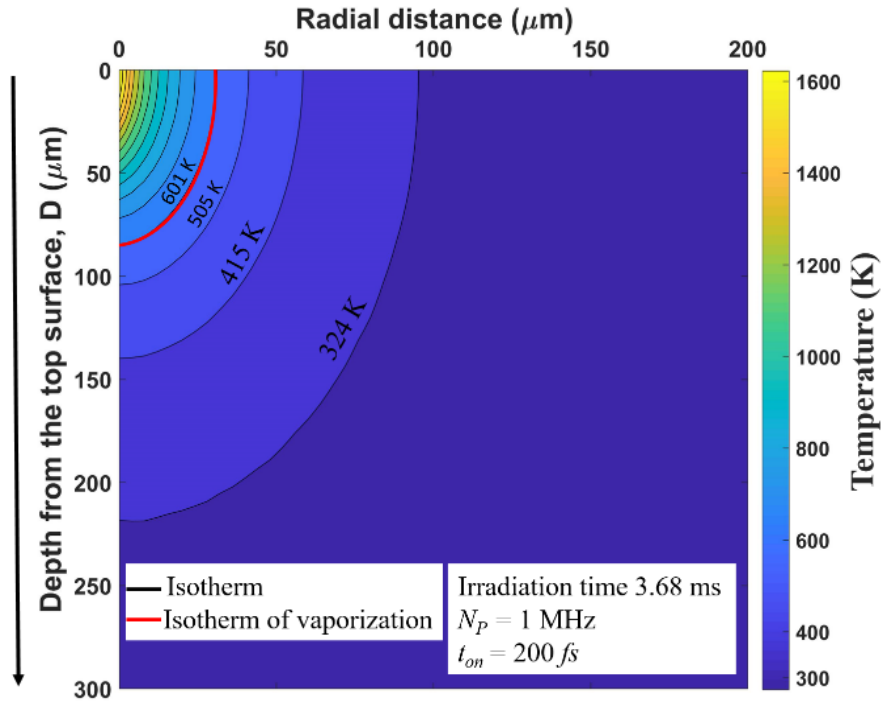


Figure 2.3: 2D contour plot of temperature distribution in the workpiece, showing isotherms to indicate the removal of materials above the isotherm of vaporization temperature marked by 601 K contour.

Fig. 2.3 shows the 2D temperature distribution in the workpiece for an average power of 2 W, the repetition rate of 1 MHz and interaction time of  $t_i = 3.68$  ms, where  $t_i = \frac{2\omega_0}{v}$ , where  $v$  is the laser cutting speed. The temperature at the workpiece surface ( $z = 0$ ) and the laser beam center ( $r = 0$ ) is around 1600 K, which is higher than the thermal decomposition temperature of PP (600 K – 700 K). By setting the temperature of 601 K (428°C) as the minimum temperature required for PP material removal, the threshold pulse energy can be determined from Fig. 2.3 for partial-depth cutting,  $D$ , on the upper surface or full-depth cutting, i.e., through cutting, from the upper to the lower surfaces. Similarly, the kerf width and the depth of cut for any pulse energy can be obtained from the contour graph (Fig. 2.3) by comparing it with the known decomposition temperature of

PP. The volume of the removed material can be calculated from the kerf width and the depth of cut by assuming a particular shape of the cross-section such as a triangular or parabolic shape.

Fig. 2.4(a) shows the surface temperature at the center of the laser beam as a function of time. It can be seen that the workpiece temperature increases very rapidly at the arrival of each laser pulse, which is expected because of the short pulse duration. Heat accumulation in the workpiece is higher at high pulse energies. The heat accumulation depends on the pulse energy and pulse repetition rate [17, 18], which need to be optimized for efficient materials processing to avoid excessive heating and thermal damage to the material. Fig. 2.4(b) shows the heat accumulation for the pulse energy  $2 \mu\text{J}$  at the repetition rate  $1 \text{ MHz}$ , and the laser-material interaction time  $3.68 \text{ ms}$  within which  $3680$  pulses are incident on the sample. It can be seen that the temperature is above the PP decomposition temperature at  $0.5 \text{ ms}$ .

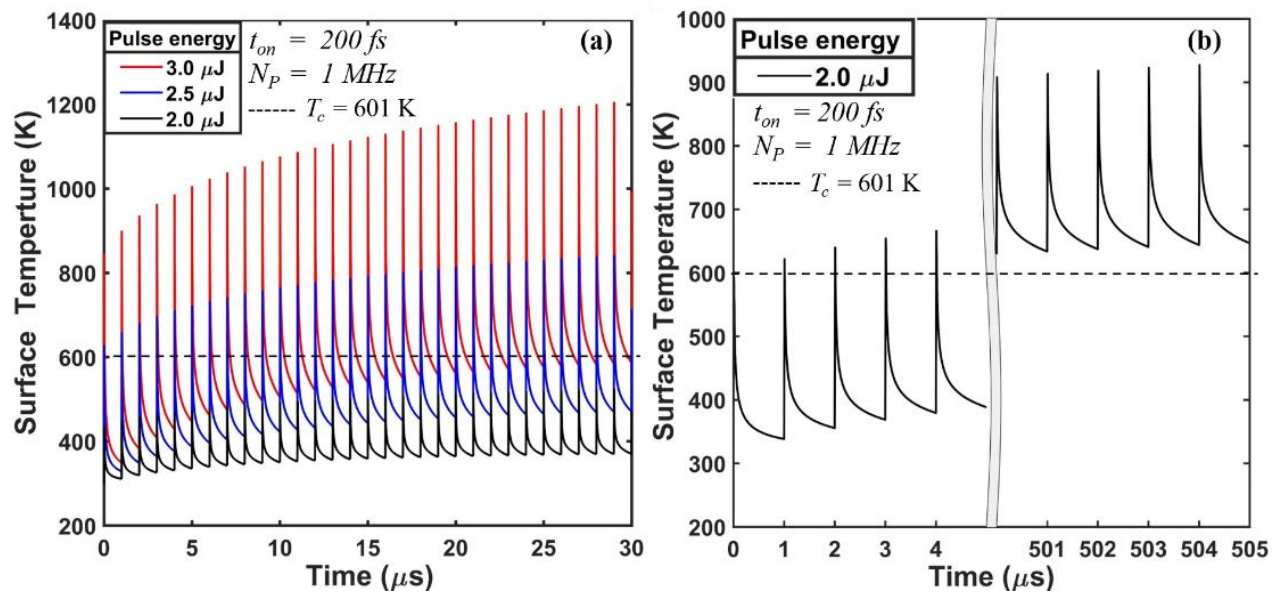


Figure 2.4: Temperature distribution over time for different energies at the surface of the workpiece ( $z = 0, r = 0$ ) and the decomposition temperature of PP indicated by a horizontal dash line, (a) heat accumulation with different pulses and (b) heat accumulation with  $2 \mu\text{J}$  pulse energy.

## 2.6 References

1. B. S. Yilbas and S. Z. Shuja, "Laser short-pulse heating of surfaces," J. Phys. D: Appl. Phys. **32**(16), 1947 - 1954 (1999).
2. M. Khenner and V. K Henner, "Temperature of spatially modulated surface of solid film heated by repetitive laser pulses," J. Phys. D: Appl. Phys. **38**(23), 4196 - 4201 (2005).
3. B. S. Yilbas and M. Pakdemirli, "Analytical solution for temperature field in electron and lattice sub-systems during heating of solid film," Physica B Condens Matter **382**(1- 2), 213 - 219 (2006).
4. B. S. Yilbas, A. Y. Al-Dweik, and S. B. Mansour, "Analytical solution of hyperbolic heat conduction equation in relation to laser short-pulse heating," Physica B Condens Matter **406**(8), 1550 -1555 (2011).
5. A. K. Nath, A. Gupta, and F. Benny, "Theoretical and experimental study on laser surface hardening by repetitive laser pulses," Surf. Coat. Tech. **206**(8-9), 2602 - 2615 (2012).
6. B. C. Stuart, M. D. Feit, S. Herman, A. M. Rubenchil, B. W. Shore, and M. D. Perry, "Optical ablation by high- power short - pulse lasers," J. Opt. Soc. Am. B **13**(2), 459 - 468 (1996).
7. T. T. Lam, "A generalized heat conduction solution for ultrafast laser heating in metallic films," Int. J. Heat Mass Transf. **73**, 330 - 339 (2014).
8. G. Chen, Y. Wang, J. Zhang, and J. Bi, "An analytical solution for two-dimensional modeling of repetitive long pulse laser heating material," Int. J. Heat a Mass Transf. **104**, 503 - 509 (2017).
9. L. L. Taylor, R. E. Scott, and J. Qiao, "Integrating two-temperature and classical heat accumulation models to predict femtosecond laser processing of silicon," Opt. Material Express **8**(3), 648 - 658 (2018).
10. V. I. Mazhukin, I. Smurov, C. Surry, and G. Flamant, "Overheated metastable states in polymer sublimation by laser radiation," Appl. Surf. Sci. **86**(1- 4), 7-12 (1995).
11. Y. K. Godovsky, *Thermophysical properties of Polymers*, (Springer, 1992).
12. C. Zang, I. A. Salman, N. R. Quick, and A. Kar, "Two-dimensional transient modeling of CO2 laser drilling of microvias in high-density flip chip substrates," in ICALEO (LIA, 2005), pp. 404-411.
13. M. N. Özışık and D. W. Hahn, *Heat conduction*, (Wiley, 2010).
14. C. Maier and T. Calafut, *Polypropylene: The Definitive User's Guide and data book*, (Elsevier, 2008).
15. S. J. Kalita, S. Bose, H. L. Hosick, and A. Bandyopadhyay, "Development of controlled porosity polymer-ceramic composite scaffolds via fused deposition modeling," Mater Sci. Eng. C **23**(5), 611 - 620 (2003).



16. S. Zhang and A. R. Horrocks, "A review of flame retardant polypropylene fibres," *Prog. Polym. Sci.* **28**(11), 1517-1538 (2003).
17. S. M. Eaton, H. Zhang, P. R. Herman, F. Yoshino, L. Shah, J. Bovatsek, and Al. Y. Arai, "Heat accumulation effects in femtosecond laser-written waveguides with variable repetition rate," *Opt. Express* **13**(12), 4708 - 4716 (2005).
18. F. Bauer, A. Michalowski, T. Kiedrowski, and S. Nolte, "Heat accumulation in ultra-short pulsed scanning laser ablation of metals," *Opt. Express* **23**(2), 1035 -1043 (2015).

## **CHAPTER 3: THERMAL EFFECTS OF ULTRAFAST LASER INTERACTION WITH POLYPROPYLENE**

(This Chapter is mostly based on the experimental part of the Author's publication: Arifur Rahaman, Aravinda Kar, and Xiaoming Yu, "Thermal effects of ultrafast laser interaction with polypropylene," *Opt. Express* **27**(4), 5764-5783 (2019).)

### 3.1 Introduction

In this chapter, the analytical solution is used to analyze the effects of processing parameters, i.e. pulse energy, scanning speed, repetition rate, focal spot size, and pulse duration. Experiments are conducted on PP sheets of thickness 300  $\mu\text{m}$ , which are important materials in many industrial applications, such as packaging for consumer products, plastic parts for various industries including the automotive industry, special devices like hinges, and fabrics [1], due to low cost, good flexibility, and low weight of this material. The experimental results will be used to verify the model and to analyze the effects of various processing parameters. The material removal rates are found to have a linear relationship with the absorbed laser energy for different values of absorptivities under various laser-PP interaction conditions, indicating that the thermal effects of different laser parameters are similar but the optical effects, i.e., the absorptivities, are different. This study on laser-PP interactions using theoretical and experimental methods shows the feasibility of using ultrashort laser pulses to cut thin polymer materials with high precision. Also, thermal model, which is developed in this study, can be applied to other laser materials processing applications, such as the laser heat treatment for surface hardening, laser drilling, laser ablation, and micro-and nano-structuring of the surface. In addition, this model can be used to determine the temperature distribution by varying the beam shape temporally and spatially for examining the shapes and sizes of the two-dimensional and three-dimensional structures produced by a given set of laser parameters.

### 3.2 Experimental studies

Commercially available PP sheets ( $(C_3H_6)_n$ ) of thickness  $300\ \mu\text{m}$  were used in this study. The reflectance and absorption coefficient of this material are measured as 81% and  $188\ \text{cm}^{-1}$ , respectively, at the wavelength of 1030 nm. A Yb: KGW (Yb doped Potassium Gadolinium Tungstate) laser of this wavelength was used to cut the PP sheets with various laser parameters. The cross-sections of the laser cut channels were prepared using both a sharp knife and a laser beam. Since similar cross-sections were obtained by both methods, the sharp knife was used for simplicity. The sheets were placed in an upright position and the cross-sections were examined in an optical microscope to measure the width and depth of the kerf.

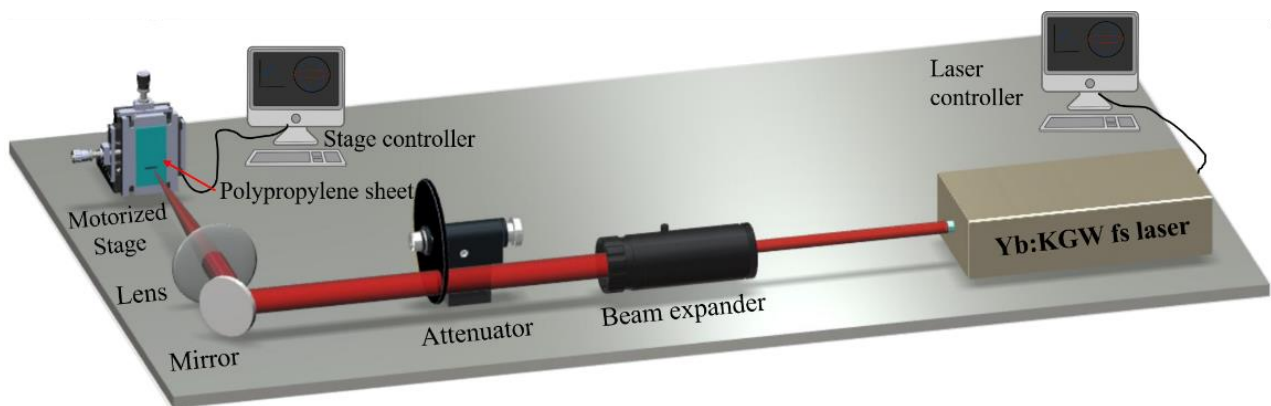


Figure 3.1: Schematics of the experimental setup for laser cutting.

Fig. 3.1 shows an experimental setup for ultrafast laser cutting of thin ( $300\ \mu\text{m}$ ) PP sheets. The laser delivers 170 fs – 10 ps laser pulses with the maximum pulse energy of 1 mJ and the repetition rate tunable up to 1 MHz. The central wavelength is 1030 nm and the maximum average output power is 6 W. The diameter of the output beam of the laser system is 4 mm which is enlarged to 10 mm by a beam expander. The laser power is controlled by an attenuator which is a

variable neutral density filter. The laser beam is focused with a lens of 250 mm focal length and the workpiece is placed at the focal plane where the beam diameter is measured to be 36.8  $\mu\text{m}$  at  $1/e^2$ -point. The surface of the workpiece is kept perpendicular to the laser beam.

### 3.3 Results and discussion

Fig. 3.2 shows experimental results for the effect of repetition rates on the laser cutting of PP sheets at 10 mm/s. For a 10 kHz repetition rate (Fig. 3.2(a)), each of the pulses has large pulse energy, therefore, the workpiece is heated to high temperatures resulting in a large heat-affected zone (HAZ). Fig. 3.2(b) shows the laser cutting at 100 kHz where the overlapping area between two successive pulses is higher than that at 10 kHz. The areas of pulse overlapping on the surface of the workpiece are 96.54% and 99.65% of the area of laser spot for 10 kHz and 100 kHz, respectively, and this overlapping area is defined as  $O_l = 2 \omega_o^2 [\cos^{-1}(\frac{v}{2\omega_o N_p}) - (\frac{v}{2\omega_o N_p}) \sqrt{1 - (\frac{v}{2\omega_o N_p})^2}]$ . The best cutting results were observed at 100 kHz with almost no HAZ where through cuts were obtained for pulse energies  $> 15 \mu\text{J}$ . Although the pulse overlapping is much higher for 100 kHz compare to previous case of Fig. 3.2(a), better cutting quality is obtained in Fig. 3.2(b) since the pulse energy is much lower than in the case of Fig. 3.2(a). For 1 MHz repetition rate (Fig. 3.2(c)), the pulse overlapping is too high (99.96%), which doesn't allow heat to dissipate in the bulk of the workpiece before the next pulse is incident on the workpiece. Therefore, the heat accumulates at the laser-material interaction zone, causing thermal damage and burning of the material as shown in Fig. 3.2(c). This heat accumulation effect is illustrated in Fig. 3.3(a).

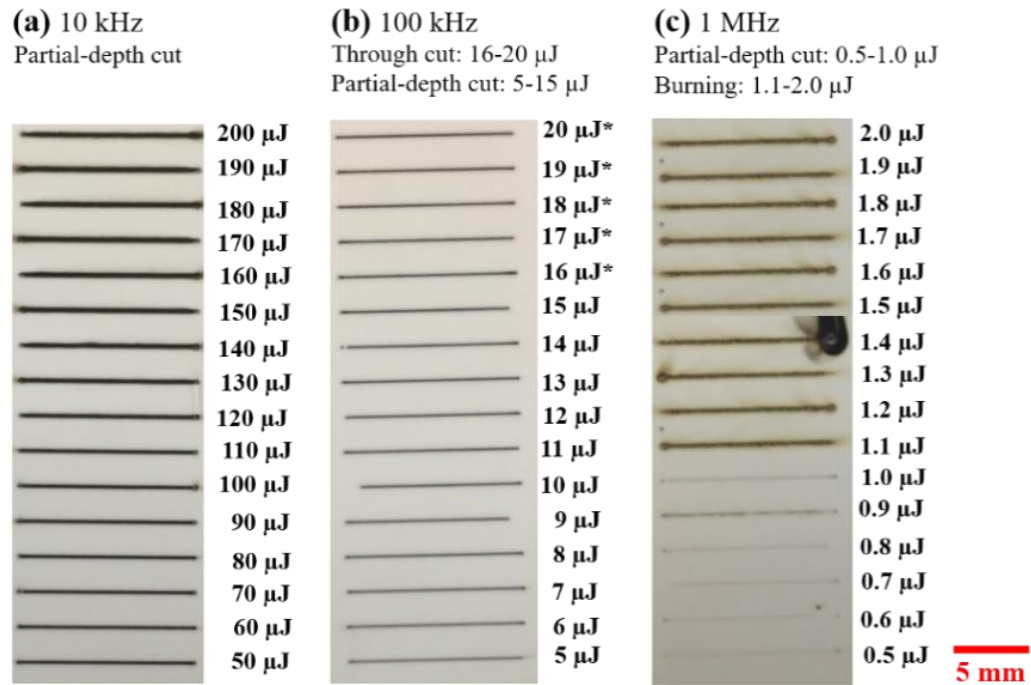


Figure 3.2: Effect of different pulse repetition rates on the laser cutting process for different pulse energies with the same average powers, showing a variety of cut quality such as partial-depth cutting, through cutting and burning of the workpiece.

The upper row in Fig. 3.3(a) shows that the time period between two pulses is very short for 1 MHz, which doesn't allow heat to dissipate, therefore heat accumulation occurs. The lower row, on the other hand, shows a longer time period between two pulses at the pulse repetition rate of 100 kHz, which provides sufficient time for heat to dissipate resulting in nearly no accumulation of heat. Fig. 3.3 (b) shows the optical microscopic top view of the workpiece after cutting experiments at 1 MHz and 100 kHz repetition rates. Partial-depth cuts were obtained for both cases, but the cuts were shallower in the case of 1 MHz pulse than for 100 kHz pulses. The reason for this effect has been explained above in Fig. 3.2. Significant HAZ and burning can be observed at 1 MHz and cleaner cuts can be seen at 100 kHz in Fig. 3.3 (b). Fig. 3.3 (c) shows a Scanning Electron Microscope (SEM) images for examining the cut surfaces at a higher magnification than in Fig. 3.3 (b). These micrographs reveal wavy but cleaner kerf produced by 100 kHz pulses,

whereas 1 MHz pulses produce wider kerf at the surface with damaged side wall. The burning, which is observed at 1 MHz pulses, is expected to induce uncontrolled heating and vaporization of the workpiece, resulting in thermal damages and highly tapered profile of the kerf.

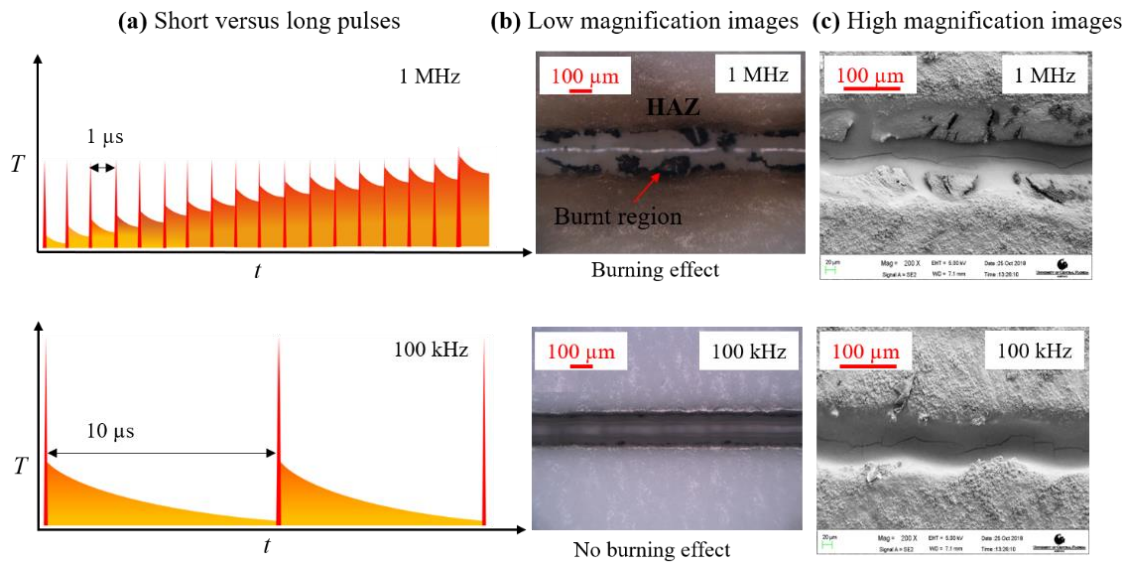


Figure 3.3: Microscopic examination of the cut quality, (a) illustration of heat accumulation at a high (1 MHz) repetition rate, (b) optical microscopic images of laser cut PP sheets at 1 MHz and 100 kHz with the same average power 1.5 W and (c) SEM images of the sheets in (b) for analyzing the cut quality at a higher magnification.

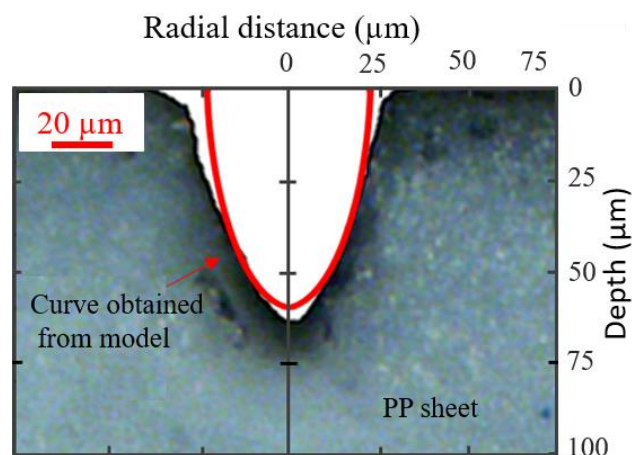


Figure 3.4: Comparison between the experimental kerf profile and the model result obtained at the cutting speed of 20 mm/s with a laser of pulse energy 20  $\mu$ J and 100 kHz repetition rate.

Fig. 3.4 shows the cross-sectional view of a laser-cut channel in PP. This partial-depth cutting was accomplished with 20  $\mu\text{J}$  pulse energy and a 100 kHz repetition rate at 20 mm/s cutting speed. Fig. 3.5 also shows a theoretical cross-section determined from the 2D thermal model corresponding to the isotherm of the decomposition temperature (601 K) of PP. The shapes of different isotherms are discussed in the previous chapter in Fig. 2.3. It can be seen that the experimental and theoretical results match fairly well. The discrepancies between the two profiles may be due to the variations in the thermophysical properties and absorptivity of PP at high temperatures during laser cutting.

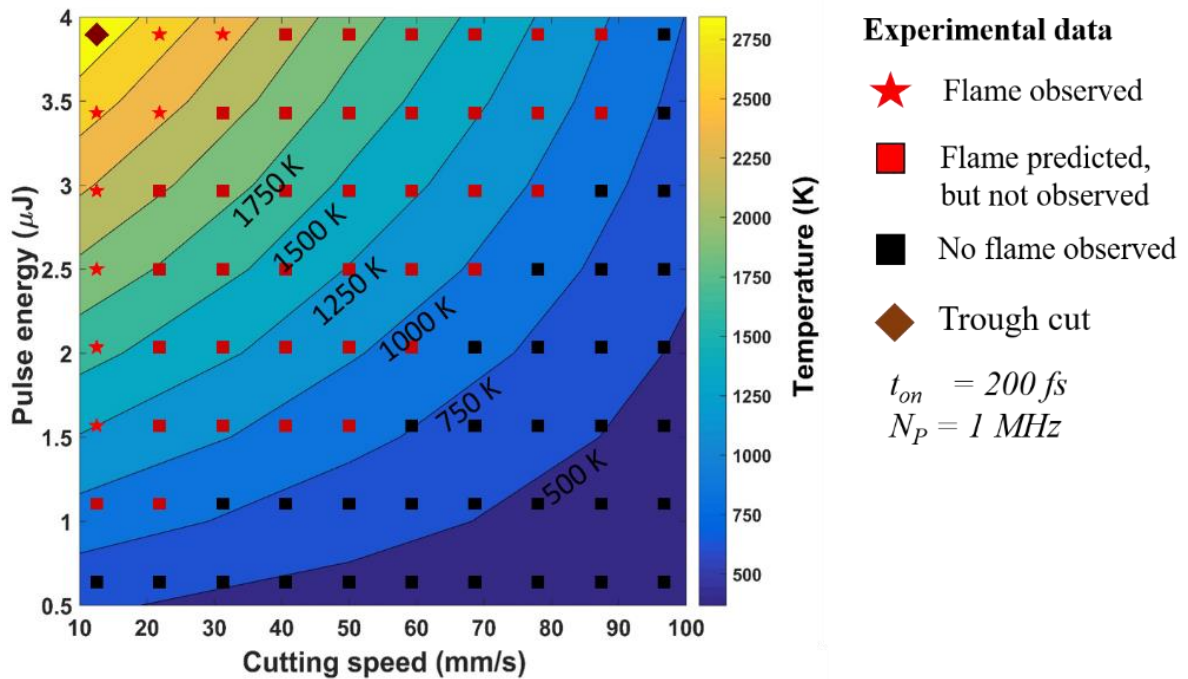


Figure 3.5: A process parameter map containing theoretical isotherms and experimental results to delineate different physical effects such as through cut and burning observed during the interaction between the ultrafast laser and PP workpiece.

During the experiments, burnings of PP, i.e. flames, were observed for low cutting speeds (10 mm/s) at high pulse repetition rates (1 MHz). Burning is caused by the self-ignition of the

material when the temperature exceeds a threshold temperature of self-ignition which is  $> 850$  K for PP [2]. Fig. 3.5 represents a laser-material interaction map based on experimental data and the thermal model to predict the occurrence of burning. The effects of four different experimental conditions are analyzed in Fig. 3.5. The experimental data show that PP self-ignites at a low cutting speed (10 mm/s) around a temperature of 1150 K. No burning is observed at higher cutting speeds and higher pulse energies (e.g., 60 mm/s and 4  $\mu$ J). The model, however, predicts the occurrence of burning under these conditions since the thermal energy carried away by the vaporized material is neglected in the model. It is postulated that when the cutting speed is high, more materials are expelled from the laser-material interaction zone and they remove a large amount of the energy deposited by the laser on the workpiece. Therefore, the temperature never reaches the self-ignition temperature.

During the cutting process, the polymeric material undergoes various phase changes, including thermal degradation, chemical decomposition of the atomic bonds in the polymeric chains, polymer vapor, and a plasma plume consisting of both positive and negative ions and neutral elements. The absorption of laser energy will, therefore, change during the cutting process, and this effect can be included in the model by considering temperature-dependent or time-dependent absorptivity. It should be noted that the thermophysical properties of the substrate, i.e., the thermal conductivity, density, and specific heat capacity, are also temperature-dependent. These properties including the absorptivity are, however, considered constant in this study to simplify the thermal analysis of the ultrashort pulse cutting process.

The absorptivity is assumed to be 20% to obtain all of the above-mentioned results from the thermal model. However, the absorptivity is expected to vary with temperature depending on various cutting conditions. This effect is examined in Fig. 10, showing that different values of



absorptivity can be estimated for different cutting conditions by comparing the experimental cut depths with the model prediction for the depth of heating. The theoretical temperature distribution yields a critical depth at which the temperature is just the decomposition temperature (601 K) of PP, and higher temperature occurs at lower depths. Therefore, the kerf will form due to material removal up to the critical depth. The temperature distribution is determined by varying the absorptivity in the mathematical model to match the critical depth with the experimental cut depth as shown in Fig. 3.6.

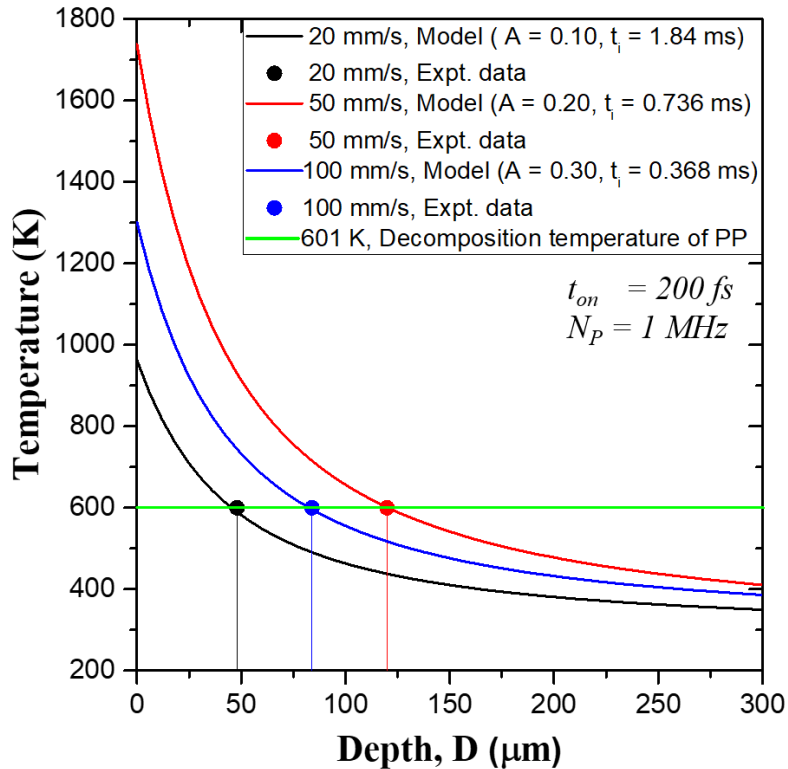


Figure 3.6: Estimation of absorptivity by fitting the theoretical results to experimental data on partial cut depths at  $r = 0$  for different cutting speeds.

The absorptivities are estimated as 0.1, 0.2 and 0.3 for 20 mm/s, 50 mm/s and 100 mm/s, respectively, at 1 MHz repetition rate. The optical properties of PP are expected to vary with the laser processing conditions since vapor and possibly plasma plume is generated at high pulse

repetition rates and low cutting speeds. The vapor and plasma plume can reflect and absorb the laser energy as the beam passes through these media and, therefore, reduces the amount of laser energy reaching the surface of the material [3]. This effect is modeled by lowering the absorptivity so that a lesser amount of the incident laser energy is deposited as heat in the workpiece.

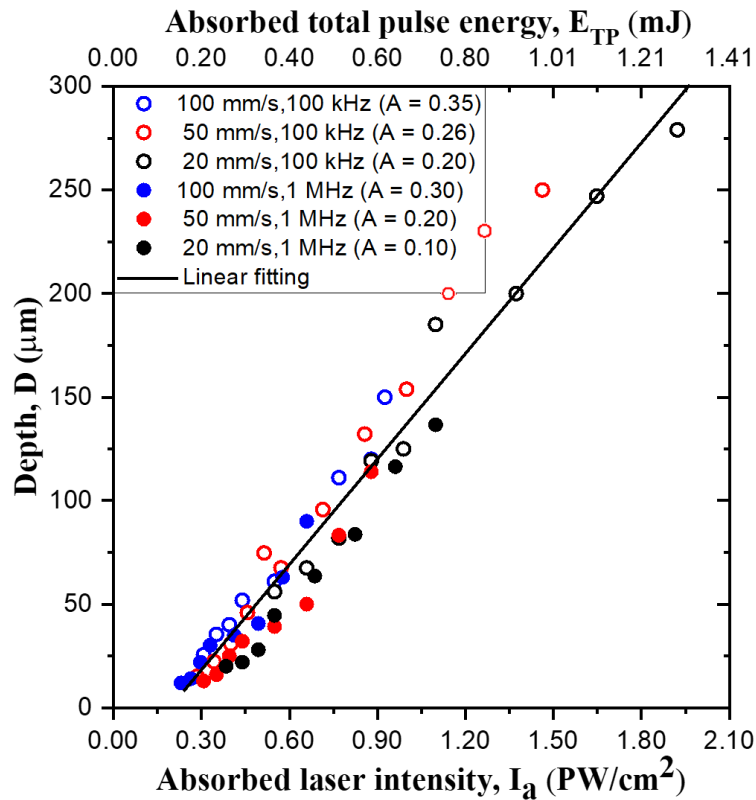


Figure 3.7: Experimental data for the depth of the cavity formed during laser cutting at different speeds and repetition rates, showing that the cut depths follow the same trend as a function of absorbed intensity.

Experiments were performed to examine the effects of various processing parameters such as the repetition rate, scanning speed, pulse energy and the laser beam diameter. Fig. 3.7 shows the depth of cut as a function of the “absorbed total pulse energy” (upper  $x$ -scale),  $E_{TP} = \frac{2\omega_0 A E_p N_p}{v}$  and the “absorbed laser intensity [4]” (lower  $x$ -scale),  $I_a = \frac{2A E_p N_p}{\omega_0 v t_{on}}$ . The depth of the cavity formed by the removed material coincides to a single straight line in Fig. 3.7 for different values of

absorptivity under various laser-PP interaction conditions, indicating that the thermal effects of different laser parameters are similar but the optical effects, i.e., the optical response of the material to the laser parameters, are different. The absorptivities for different processing conditions can be estimated by comparing the results of HCM with the experimental results of the cavity depth as explained in Fig. 3.6. The experimental data are fitted as the following linear equation

$$D = b(I_a - I_{a_o}) \quad (3.1)$$

where the slope,  $b$ , and the threshold absorbed intensity for material removal,  $I_{a_o}$ , are found to be  $0.0178 \text{ cm}^3/\text{PW}$  and  $0.21 \text{ PW}/\text{cm}^2$ , respectively. Using this linear relationship, one can estimate the “total energy or total intensity” to cut any thickness of PP sheet.

To study the effect of the absorbed power on the volume of material removed during the cutting process, an Overall Energy Model (OEM) is presented by considering an energy balance between the total amount of absorbed laser energy and the heat losses due to conduction in the workpiece and the heating of the vaporized material as discussed. The heat loss,  $H_l$ , occurs due to conduction through the two side walls of the kerf, and the heating energy loss,  $H_e$ , occurs due to the heating of the removed material from room temperature to the vaporization temperature. This model yields by following equation:

$$v w_k D = \frac{1}{H_e} (A E_p N_p) - \frac{H_l}{H_e} \quad (3.2)$$

where  $w_k$  is the kerf width produced during partial-depth cutting of the workpiece. Here,  $H_e$  and  $H_l$  are the heating energy and the heat energy loss, respectively.

Eq. (3.2) is derived by considering an overall energy balance per unit time for the absorbed laser energy, loss of energy due to heat conduction in the substrate and the amount of energy used

for heating the removed material from room temperature to a final temperature  $T_f$  so that  $T_f$  is higher than the vaporization temperature of the material. The quasi-steady state energy balance over a time  $t$  is written as

$$\begin{aligned}
 N_p E_p A t = & \frac{1}{2} v w_k D \rho [c_p (T_m - T_o) + H_m + H_v + c_p (T_f - T_m)] t + k \frac{(T_f - T_o)}{\sqrt{\alpha t_{on}}} v t_{on}^2 N_p d_p t \\
 & + k \frac{(T_f - T_o)}{2\sqrt{\alpha t_{off}}} v (t_{on} + t_{off}) d_p t_{off} N_p t
 \end{aligned} \tag{3.3}$$

where the first term on the left-hand side is the absorbed laser energy. The first term on the right-hand side is the total amount of energy required to heat a volume of material to produce the kerf. The kerf profile is considered to have a triangular shape of width  $w_k$  and depth  $D$ . The second and third terms are the heat losses through the two side walls of the kerf due to conduction during the pulse-on and pulse-off times respectively. Since the temperature of the side walls decreases rapidly during the pulse-off time, an average temperature  $(T_f + T_o)/2$  is considered to estimate the conduction heat loss due to a linear thermal gradient over a thermal boundary layer of width  $2\sqrt{\alpha t_{off}}$ , where  $\alpha$  is the thermal diffusivity. Also, the conduction heat loss occurs during the pulse-off time over the side wall length of  $v t_{on}$  produced during the pulse-on time and the length of  $v t_{off}$  created during the pulse-off time, which appears in Eq. (3.3) as  $v(t_{on} + t_{off})$ .

In Eq. (3.3),  $d_p = \frac{v D}{2N_p \omega_o}$ ,  $T_f$ ,  $T_m$  and  $k$  are the kerf depth created per pulse, the final temperature reached during the cutting process, the melting temperature and thermal conductivity of the material, respectively. The other variables  $H_m$ ,  $H_v$ , and  $t_{off}$  represent the latent heats of

melting and vaporization, and the pulse-off time, respectively.  $H_m$  and  $H_v$  are irrelevant for the case of ablating PP [5].

Eq. (3.3) can be simplified to Eq. (3.2) with the following expressions for  $H_e$  and  $H_l$ :

$$H_e = \frac{1}{2} \rho [c_p(T_f - T_o) + H_m + H_v];$$

$$H_l = \sqrt{k\rho c_p} \frac{(T_f - T_o) v^2 D}{4 \omega_o} [2t_{on}^{3/2} + t_{off}^{3/2} + t_{on}\sqrt{t_{off}}]$$

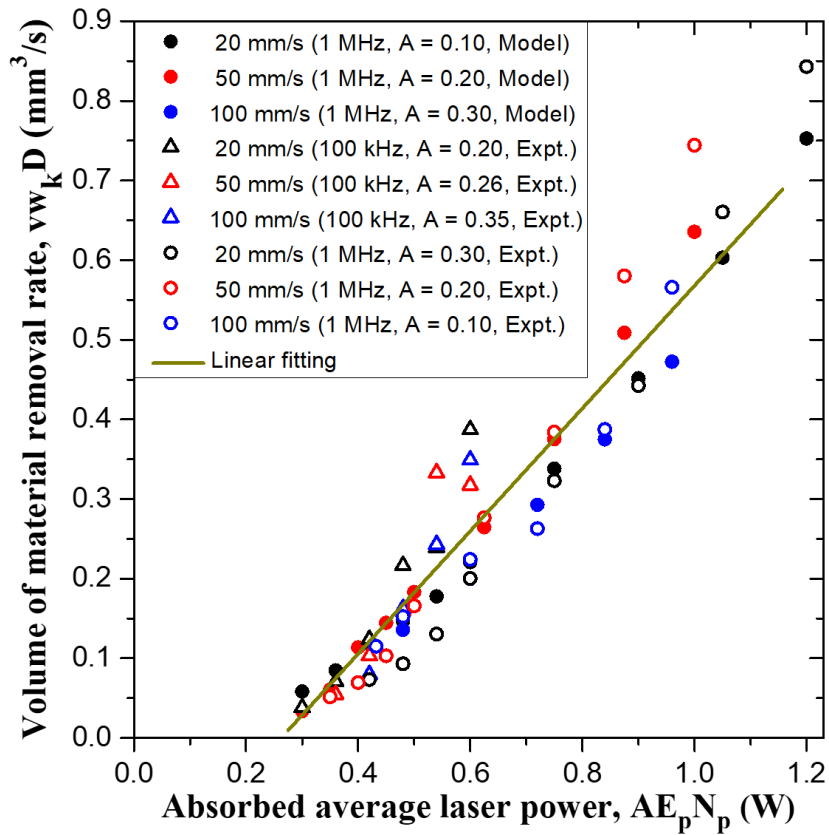


Figure 3.8: Comparison between the experimental data for the material removal rate as a function of absorbed average power during laser cutting and the corresponding linear trend predicted by an overall energy balance model.

Fig. 3.8 compares this linear relationship, Eq. (3.2), with experimental results and yields the heating energy  $H_e = 1.28 \text{ J/mm}^3$  as the slope of the straight line and the heat energy loss  $H_l =$

0.263 W as the intercept of the straight line on the x-axis at which  $D = 0$ . Therefore,  $H_l$  can be interpreted as the threshold absorbed laser power for material removal, i.e.,  $H_l = (AE_p N_p)_o$ , and Eq. (3.2) can be rewritten as  $v w_k D = \frac{(AE_p N_p) - (AE_p N_p)_o}{H_e}$ . Two significant unknown parameters in Eq. (3.2) are the absorptivity  $A$  and the final temperature  $T_f$  besides the thermophysical properties of the material.  $T_f$  and  $A$  can be estimated using the HCM as discussed in Fig. 3.6. The values of  $T_f$ , which were determined for different pulse energies 1 to 4  $\mu\text{J}$ , vary from 612 to 1555 K for 20 mm/s, 717 to 1974 K for 50 mm/s, and 629 to 1625 K for 100 mm/s cutting speeds. While the HCM provides a detailed analysis of the thermal energy distribution by the heat conduction mechanism during laser heating, the OEM yields a simple linear equation to analyze experimental data for determining the energy loss due to conduction and the utilization of energy for vaporization.

### 3.4 Summery

An analytical solution to the governing equation for heat transfer in ultrashort laser pulse heating of solid PP sheets is obtained using the integral transform method and Duhamel's theorem. The temperature distributions for radial and axial locations are modeled, and the effects of repetition rate and scanning speed are investigated. The calculation using the model and the measured the depth of cut and kerf width are in good agreement. From experimental studies, it is observed that a repetition rate of 100 kHz is capable of producing clean, through cut at pulse energies of tens of  $\mu\text{J}$ . The depths of cavities under partial-depth cutting conditions with different laser parameters collapse into a single straight line as a function of intensity. A simple overall energy balance model is presented, showing that the volumes of vaporized material also coincide

on a single straight line as a function of the absorbed laser power. Experimental data can be analyzed using this overall energy model to determine the conduction loss of energy and the utilization of energy for vaporizing the removed material.

### 3.5 References

1. H. A. Maddah, "Polypropylene as a promising plastic: A Review," *Am. J. Polym. Sci.* **6**(1), 1-11 (2016).
2. R. Anandjiwala, L. Hunter, R. Kozlowski, and G. Zaikov, *Textiles for sustainable development*, (Nova Science Publishes, 2007), Chap. 19.
3. A. Kar, J. A. Rothenflue, and W.P. Latham, "Scaling laws for thick-section cutting with a chemical oxygen-iodine laser," *J. Laser Appl.* **9**(6), 279 - 286 (1997).
4. A. Kar and J. Mazumder, "Two-dimensional model for material damage due to melting and vaporization during laser irradiation," *J. Appl. Phys.* **68**(8), 3884-3891 (1990).
5. C. Zang, I. A. Salman, N. R. Quick, and A. Kar, "Two-dimensional transient modeling of CO<sub>2</sub> laser drilling of microvias in high density flip chip substrates," in *ICALEO (LIA, 2005)*, pp. 404-411.

## **CHAPTER 4: TIME-RESOLVED MEASUREMENTS OF ULTRAFAST LASER INTERACTION WITH POLYPROPYLENE**

(This Chapter is mostly based on the Author's publication: Arifur Rahaman, Aravinda Kar, and Xiaoming Yu, "Time-resolved measurements of optical properties in ultrafast laser interaction with polypropylene," *Opt. Express* **28**(2), 2640-2648 (2020).)

### 4.1 Introduction

Ultrafast lasers have been used widely for high precision material processing in fundamental research and industrial applications since the 1980s [1, 2]. High-power ultrashort laser pulses are used in various types of material processing including laser drilling [3], cutting [4], surface hardening [5], polishing [6,7], cleaning [8] and micro/nano machining [9,10]. When an ultrafast laser pulse is focused onto a target material with the energy density (i.e., fluence) exceeding the damage threshold of that material, vaporization and eventually the formation of plasma (consisting of atoms, positive and negative ions, molecules, nanoparticles, clusters and agglomerates [11]) can form resulting in luminous light emission [11,12]. Laser-produced plasmas (LPPs) has a great advantage in a variety of applications including laser-induced breakdown spectroscopy [13], high-order harmonic generation [14], attosecond pulse generation [15], nanoparticle generation [16] and material analysis[17]. However, LPPs might deteriorate laser processing quality and efficiency (especially for polymers, which typically have a low melting point) by absorbing and reflecting laser energy as the beam passes through the plasma, thereby reducing the amount of laser energy reaching the surface of material [18]. Therefore, it is essential to understand the dynamics of ultrafast laser interaction with polymers for improving processing quality. In addition, optical properties such as reflectance, transmittance and absorptance are crucial in selecting laser-processing parameters, and such properties become fluence (intensity) dependent for high pulse energies.



The optical properties and dynamics of laser-material interaction depend on laser wavelength, pulse duration, intensity, temporal and spatial pulse shape, pulse repetition rate, ambient environment, and material properties [19]. The characteristics vary with time and space rapidly, so optical properties and LPPs are transient effects that are not easy to measure and detect. To understand the dynamics of ultrafast laser-material interaction, time-resolved measurements are essential. Researchers have used various methods for such measurements, including shadowgraph, holography, interferometry, beam deflection, and probe beam diagnostics [20]. The most commonly used approaches are pump-probe beam diagnostics and shadowgraphy. Pump-probe experiments are complicated involving multiple-beam paths and the reconstruction of the event requires delay scan, which can be time-consuming [21]. In the case of the optical shadowgraphy, the duration of the probe beam is required to be short to image a fast event with a suitable detector (such as a CCD camera) with approximate magnification [22]. Although Z-scan is a simple and effective technique to measure the nonlinear refraction and absorption coefficients, it requires scanning the sample which is also time-consuming [23, 24]. To analyze the elementary composition of a target, researchers are using laser-induced breakdown spectroscopy (LIBS) technology, which can reveal the physical processes that lead to the formation of high-temperature plasma induced by a short pulse [25]. During the plasma cooling period, light emits from the plasma cloud as the electrons of the atoms and ions at the excited states fall down to the ground state. The ellipsoidal mirror-based method can also be used to detect such events if the sample is irradiated with sufficient fluence (intensity) to create a plasma cloud.

In our previous study, it was found that heat accumulation and plasma or surface vaporization due to high repetition rate deteriorates the processing quality of polypropylene (PP) [26], an important material in many industrial applications, such as packaging for consumer's products,

plastic parts for various industries (including automotive industry), special devices like hinges and fabrics [27]. In this study, time-resolved measurements of the interaction between ultrafast lasers with PP is performed with an ellipsoidal reflector. The absorptance is determined by analyzing the transmitted and reflected signals detected by photodiodes and a GHz-bandwidth oscilloscope. The dynamics of ultrafast laser interaction with polypropylene are studied experimentally in the single-shot configuration. The experimental results are explained with a model that accounts for different effective absorption channels and the nonlinear absorption coefficient is estimated, which suggests that the nonlinear absorption originates from two-step or two-photon (where two photons are simultaneously absorbed) absorption through overtones [28].

## 4.2 Experimental setup

The interaction of a Yb: KGW (Pharos, Light Conversion) laser, delivering ultrashort laser pulses of pulse length 170 fs and center wavelength 1030 nm, with white opaque PP sheets were studied. Each sheet was 300  $\mu\text{m}$  thick containing small amounts of several impurities Si, C, Li, Na, Al, K, and  $\text{SiO}_2$  that exhibited characteristic peaks in the secondary ion mass spectroscopic spectrum. The experimental setup for time-resolved measurements is shown in Fig. 4.1. In this system, the femtosecond laser beam, whose diameter is enlarged to  $\sim 10$  mm by a beam expander and pulse energy-adjusted by a variable neutral density filter (attenuator, in Fig. 4.1), is focused onto the sample with a lens of 250 mm focal length. A beam splitter is used to reflect 6.5% of the beam, which is used as a reference beam to determine the incident laser pulse energy.

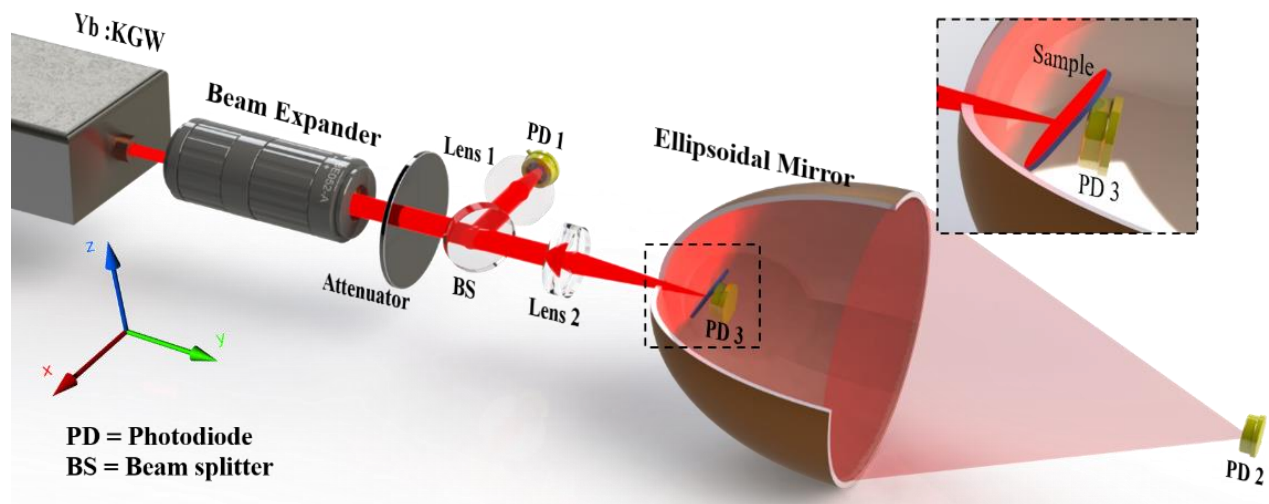


Figure 4.1: Schematic for experimental set up for time-resolved measurement

Three photodiodes (PD 1-3, Thorlabs, FDS100) are used in the experiment, and data acquisition is through a 1-GHz oscilloscope (Tektronics, MDO3104). The PP sheet is placed on the top of a fixture, which is used to hold both the PP sample and PD 3. The PP sheet is irradiated with a single laser pulse and the reflection signal of the irradiated pulse is captured by an ellipsoidal reflector (E180, Optiforms) with silver coating. We choose to use an ellipsoidal reflector because it enables to collect most of the reflected light [29, 30] and to have easy access to the sample. In this system, the sample is placed at lens 2's focus, which coincides with the internal (first) focal point of the ellipsoidal reflector. The surface normal of the sample is tilted with an angle of  $17^\circ$  with respect to the laser beam to reduce light backscattering through the entrance hole of the ellipsoidal reflector, while both specular and diffusive reflections are collected by this ellipsoidal reflector and detected by PD 2, which is located near the external (second) focal point of the ellipsoidal mirror. To position PD 2, the ellipsoidal mirror is held with a fixture that is mounted on a 3D stage. By adjusting the 3D stage, the light reflected by the ellipsoidal mirror is focused on PD 2 at low intensity. Then, the signal from PD 2 is maximized by tuning the position of PD 2.

The active area for the photodiode is  $3.6 \text{ mm} \times 3.6 \text{ mm}$ . PD 3 is placed at the back of the PP sheet to detect the transmission signal. A fixture attached to a 3D stage is used to move the sample to ensure a fresh surface for each laser shot. The rise/fall time,  $t_r$ , of this photodiode (FDS100) is 2.12 ns, which is calculated using the load resistance  $R_{load} = 40 \text{ } \Omega$  and junction capacitance  $C_j = 24 \text{ pF}$ . The impulse response time is measured as 3.23 ns, which is the FWHM of the shortest pulse measured by the oscilloscope for this photodiode. Compared to other techniques such as pump-probe and Z-scan, our setup does not require scanning of delay or sample position, which is time-consuming. The presented setup can be modified to collect spectral data by replacing PD 2 with a spectrometer.

### 4.3 Experimental Results

Fig. 4. 2(a) shows the output signal recorded by the oscilloscope for the incident, reflected and plasma, and transmitted beam by PD 1, PD 2, and PD 3, respectively. The signal is obtained when a pulse with an energy of  $20 \text{ } \mu\text{J}$  and peak fluence of  $3.76 \text{ J/cm}^2$  irradiates the sample. As mentioned before, 6.5% of the incident light is obtained as the reference beam and 86% reaches the sample. To avoid saturation in PD 2 the reflection signal is attenuated by 10 times by using an ND filter in front of PD 2. The shaded regions are integrated area at FWHM for each of the signals and the integrated area for each signal is shown in the inset. The temporal behavior of the PD 2 signal exhibits features different from the incident and transmission signal. It can be seen from Fig. 4.2(a) that PD 2 outputs two peaks, a large (“main”) peak between  $t=0$  and 40 ns, and a small peak centered around  $t = 90 \text{ ns}$ . Here, the first peak corresponds to the reflection of the laser pulse itself and second peak is attributed to plasma emission [11] due to the laser-material interaction as the emission is not observed below the damage threshold. Although our experimental setup cannot

detect plasma emission in the UV wavelength due to the silver coating of the ellipsoidal mirror and the responsivity of the silicon photodiodes, the measurement of reflectance is not influenced by the plasma because only the first peak is used in the analysis, while the second peak, which is attributed to plasma emission, is ignored.

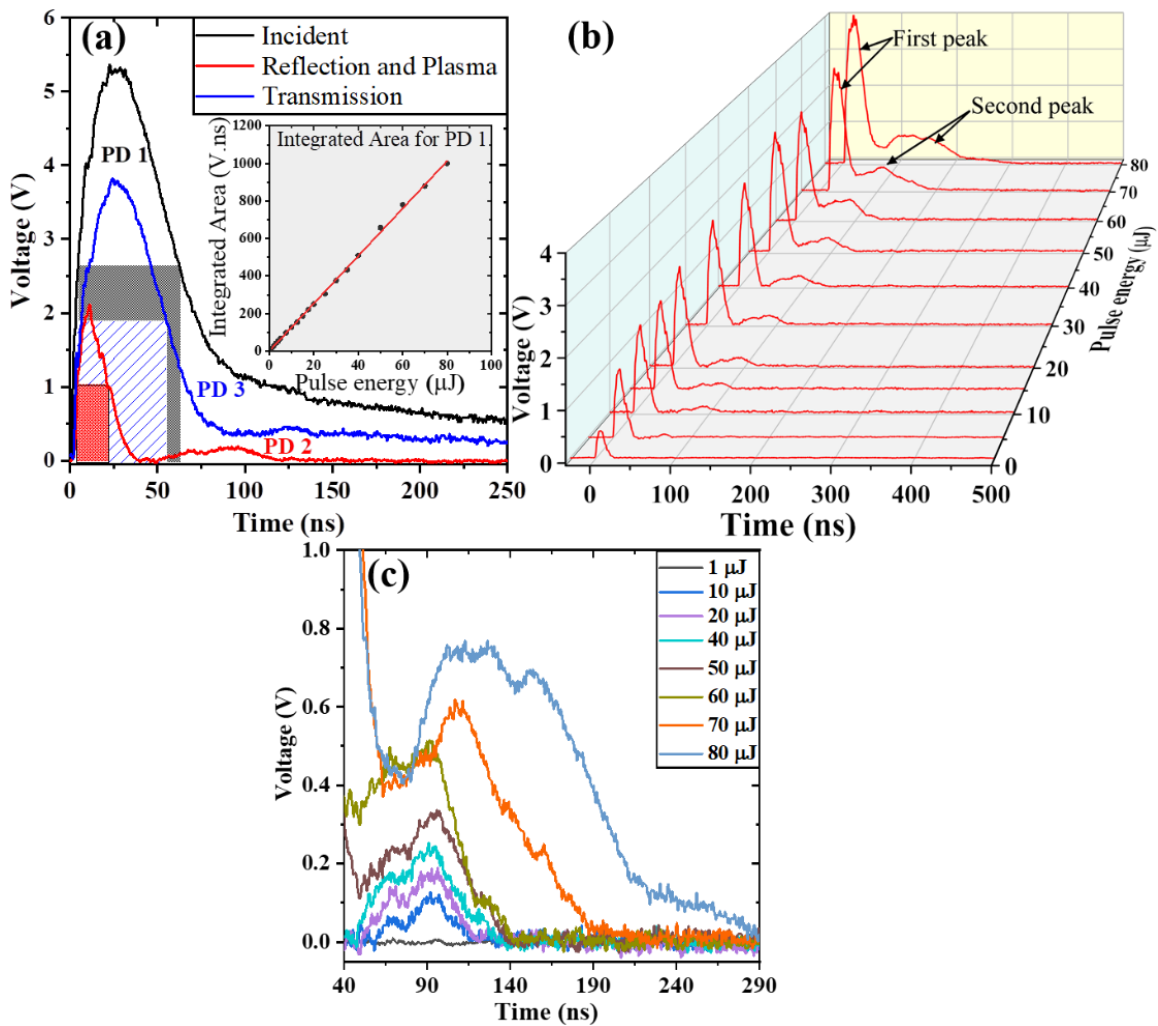


Figure 4.2: PD signals observed on the oscilloscope (a) Incident, reflected, and transmitted signal for 20- $\mu\text{J}$  pulse energy. The signals are scaled by 6.5%, 10%, and 100%, respectively. Shaded region for each of the signals represents the FWHM integrated area. The inset shows the linearity of the PDs (only PD 1 is shown here). (b) The signal detected by PD 2 for different pulse energies. (c) Second peaks with different pulse energies.

However, events that occur shorter than ns might not be detected due to the slow response of photodiodes (ns response time). Fig. 4.2(b) shows the PD 2 signal as a function of pulse energies. It can be seen from Fig. 4.2(c) that the signal of the second peak increases with higher pulse energy due to increased plasma formation. The second peak signals are absent for peak fluence  $< 0.56 \text{ J/cm}^2$ , which corresponds to  $3 \mu\text{J}$  pulse energy, where the damage threshold is found to be  $0.15 \text{ J/cm}^2$ , which corresponds to pulse energy of  $800 \text{ nJ}$ .

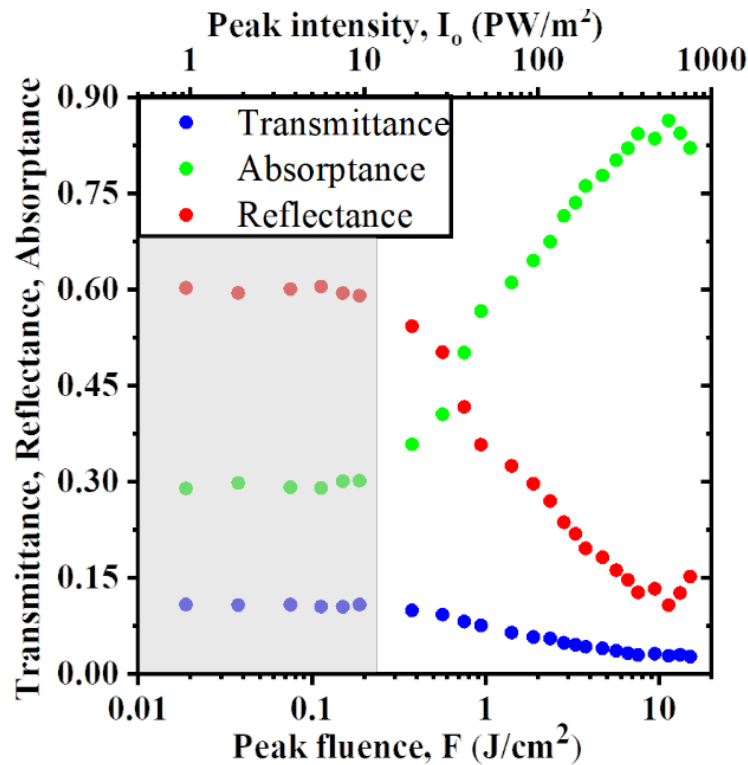


Figure 4.3: Reflectance (R), transmittance (T), and absorptance (A) of PP sheet as a function of laser fluence.

Fig. 4.3 shows the total reflectance,  $R$  (specular and diffusive), transmittance,  $T$  and absorptance,  $A$  as a function of peak fluence and peak intensity. In calculating  $R$  and  $T$ , integrated areas at FWHM of the PD traces for reflection and transmission are used with proper scaling based on their attenuation. Then, the integrated areas for reflection and transmission are divided by the

corresponding integrated area of the incident signals to get  $R$  and  $T$ , respectively. In determining  $R$ , only the first peak of the PD 2 signal is considered. Absorbance,  $A$  is calculated as  $A = I - T - R$ . It is found that the reflectance of the sample remains constant ( $R = 0.6$ ) for peak fluence  $< 0.3 \text{ J/cm}^2$ , because the material surface does not undergo any change. The reflectance begins to decrease quickly after the damage threshold peak fluence  $0.15 \text{ J/cm}^2$  is reached, and continues to decrease beyond the threshold of plasma formation,  $0.56 \text{ J/cm}^2$  (discussed in Fig. 4.2). Since the damage doesn't occur below the damage threshold fluence, the transmittance in Fig. 4.3 and the absorbance in Fig. 4.3 remain constant until the damage threshold peak fluence is reached. This regime is called the "linear absorption region", which is marked with shade in Fig. 4.3. As the peak fluence increases, the reflectance drops because of non-linear absorption, which will be explained in detail in the next section.

#### 4.4 Model and Discussion

Although ultrafast lasers are suited for processing polymeric material [20], understanding of several fundamental questions, including the relative significance of different linear and nonlinear absorption processes, is still lacking. In the case of focusing femtosecond laser pulses into polymers, a photon may not have enough energy to promote an electron from the valance band to the conduction band at low laser intensity. However, for wide band-gap material like polymers, absorption of laser is a mix of linear (single-photon) and nonlinear (multiphoton) processes. The equation describing the attenuation of the ultrafast laser pulse with an intensity  $I(z)$  passing through the material undergoing single-photon and two steps absorption or two-photon absorption is given by

$$\frac{dI(z)}{dz} = -\alpha_1 I(z) - \alpha_2 I^2(z) \quad (4.1)$$

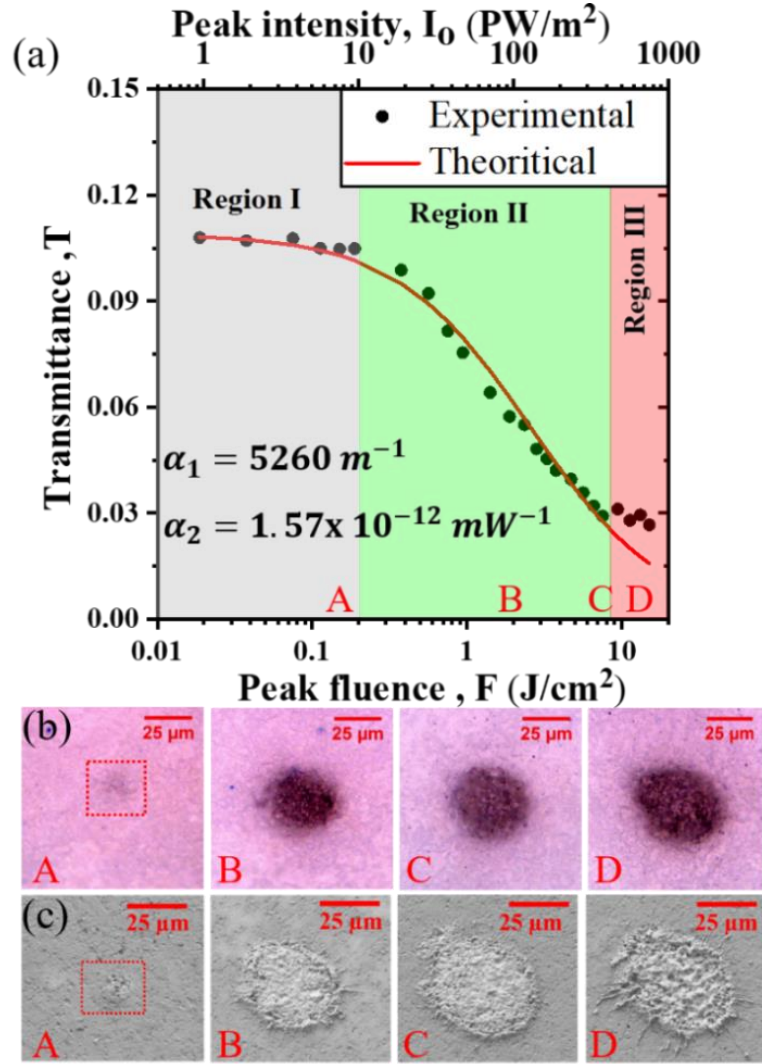


Figure 4.4: (a) Fitting of the experimental results using Eq. 4.2. The laser intensity used in this experiment can be divided into three regions (Region I, II and III). Damage observed by (b) optical and (c) scanning electron microscopy (SEM) at corresponding intensities 9.4 (A), 94.1 (B), 378.3 (C) and 658.2 (D) PW/ m<sup>2</sup> shown in (a).

where  $\alpha_1$  is the linear absorption coefficient and  $\alpha_2$  is the third-order nonlinear absorption coefficient. The transmittance of the ultrafast laser pulse through the sample can be found from the solution to the differential equation (4.1), which can be written as



$$T = \frac{I(z)}{I_o} = \frac{(1-R)e^{-\alpha_1 z}}{1 + \frac{\alpha_2}{\alpha_1}(1-R)I_o(1 - e^{-\alpha_1 z})} \quad (4.2)$$

where  $R$  and  $I_o = F/t_{on}$  are the reflectance and the peak intensity of the laser pulse, respectively, with the peak fluence  $F = \frac{2E}{\pi w_o^2}$ . Here,  $E$ ,  $w_o$  and  $t_{on}$  are the laser pulse energy, the radius of the incident beam, and pulse duration, respectively.

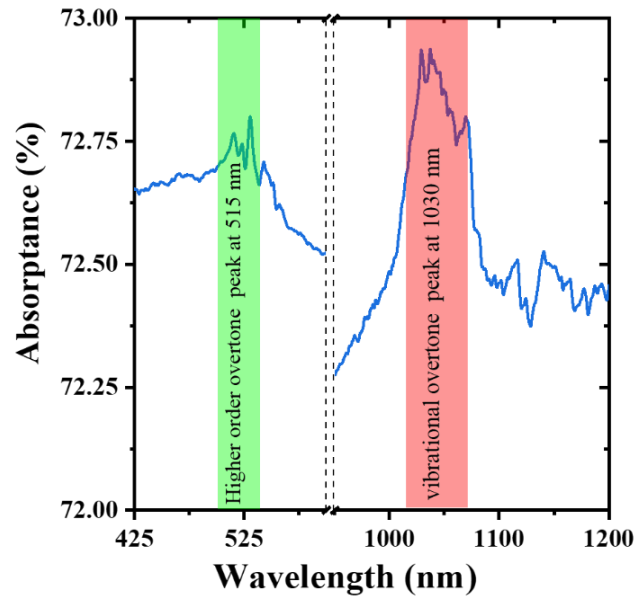


Figure 4.5: Absorbance,  $A$  of impure PP sample is determined from the transmittance,  $T$ , and the specular reflection measurement,  $R_s$  of PP sample by using a spectrophotometer (Cary 500).

Fig. 4.4(a) shows experimental data on transmittance,  $T$ , that can be classified into three regions. In Region I,  $T$  remains nearly constant up to an ablation threshold fluence (or intensity), and then  $T$  decreases as the fluence increases in Region II indicating nonlinear laser-matter interaction. In Region III, however, the data fluctuates but the average value exhibits nearly fluence-independent transmittance indicating linear absorption. The absorption spectrum in Fig.

4.5 reveals the degree of nonlinear absorption in Region II due to the presence of two absorption peaks at 1030 and 515 nm. While the peak at 1030 nm indicates the vibrational overtone absorption of the incident laser photons, the peak at 515 nm provides a mechanism for two-step or two-photon absorption through overtone [28]. To determine the linear absorption coefficient  $\alpha_1$ , the two-photon absorption coefficient  $\alpha_2$  was set to zero in Eq. (4.2) to obtain the solution of single-photon absorption,  $T = (1-R)e^{-\alpha_1 L}$ . This equation was fitted to the experimental data in Region I using the values of R as a function of  $I_0$  from Fig. 4.3 and  $L = 300 \mu\text{m}$ , and  $\alpha_1$  was found to be  $5260 \text{ m}^{-1}$ . Using this value of  $\alpha_1$ , Eq. (4.2) was fitted to the experimental data in both Regions I and II for the nonlinear absorption coefficient,  $\alpha_2 = 1.57 \times 10^{-12} \text{ mW}^{-1}$ . This value is consistent with previously found values for polymers [31, 32].

The reversal of nonlinear absorption to linear absorption in Region III, which begins at the peak intensity  $470 \text{ PW/m}^2$  in this study, may be attributed to air breakdown in front of the substrate surface at high intensities. Several studies [33-36] have reported the air breakdown threshold peak intensity in the range of 100 to  $1000 \text{ PW/m}^2$  for femtosecond laser with pulse duration 100 – 200 fs and wavelength 800 nm. The air plasma formed in front of the substrate due to this breakdown can reflect and absorb much of the incident laser energy. Therefore, the actual laser intensity at the substrate surface is reduced significantly, resulting in linear absorption in the substrate. Figs. 4.4(b, c) show laser damages on the surfaces of the PP sheet at the fluences 0.15, 1.88, 7.52, and  $13.16 \text{ J/cm}^2$  for damages A, B, C, and D, respectively. Damage A corresponds to the damage threshold fluence/intensity in Region I, whereas damage D corresponds to Region III. Damages B and C indicate that the damage size changes with fluencies/intensities in Region II, whereas the damage size was found to be nearly the same as the damage size D in Region III. This effect of

intensity on damage size correlates with the measured transmittance very well since the transmittance decreases steadily in Region II but remains almost constant in Region III.

#### 4.5 Summery

In summary, time-resolved measurements of reflectance, transmittance, and absorptance are performed for laser intensity ranging from well below to well-above the damage threshold. An ellipsoidal mirror enables the collection of the majority of the reflected light (>98.2 %) while providing easy access to the sample compared to an integration sphere. We observe in the reflection signal a distinct “double-peak” feature, which is interpreted as light emission from laser-induced plasma. A model that includes linear and nonlinear absorption explains the experimental data. Accordingly, the laser intensity used for processing polymers can be divided into three regions, each with a dominant absorption channel. This study provides information for designing and optimizing laser processing systems for polymers.

#### 4.6 References

1. W. Sibbett, A. A. Lagatsky, and C. T. A. Brown, "The development and application of femtosecond laser systems," *Opt. Express* **20**(7), 6989 - 7001 (2012).
2. K. Sugioka and Y. Cheng, "Ultrafast lasers - reliable tools for advance materials processing", *Light Sci. Appl.* **3**, e149 (2014).
3. X. Zhao, and Y.C. Shin, "Femtosecond laser drilling of high - aspect ratio microchannels in glass," *Appl. Phys. A* **104**, 713-719 (2011).
4. A. N. Fuchs, M. Schoeberl, J. Tremmer, and M.F. Zaeh, "Laser cutting of carbon fiber fabrics," *Phys. Procedia* **41**, 372 - 380 (2013).
5. A. K. Nath, A. Gupta, and F. Benny, "Theoretical and experimental study on laser surface hardening by repetitive laser pulses," *Surf. Coat. Tech.* **206** (8-9), 2602 - 2615 (2012).
6. M. Malinauskas, A. Žukauskas, S. Hasegawa, Y. Hayasaki, V. Mizeikis, R. Buividas and S. Juodkazis, "Ultrafast laser processing of materials: from science to industry," *Light Sci. Appl.* **5**, e16133 (2016).
7. L. L. Taylor, J. Xu, M. Pomerantz, T. R. Smith, J. C. Lambropoulos, and J. Qiao, "Femtosecond laser polishing a germanium," *Opt. Express* **9**, 4165 - 4177 (2019).
8. T. Ersoy, T. Tunay, M. Uğuryol, G. Mavili, and S. Akturk, "Femtosecond laser cleaning of historical paper with sizing," *J. Cult. Herit.* **15**(3), 258- 265 (2014).
9. R.R. Gattass and E. Mazur, "Femtosecond laser micromachining in transparent materials," *Nat. Photonics* **2**, 219 - 225(2008).
10. W. Jia, Y. Luo, J. Yu, B. Liu, M. Hu, L. Chai, and C. Wang, "Effects of high-rate femtosecond laser micromachining on the physical and chemical properties of polylactide (PLA)," *Opt. Express* **23**(21), 26932 - 26939 (2015).
11. B. Verhoff, S.S. Harilal, J.R. Freeman, P.K. Diwakar, and A. Hassanein, "Dynamics of femto- and nanosecond laser ablation plumes investigated using optical emission spectroscopy," *J. Appl. Phys.* **112**, 093303 (2012).
12. S. Sankaranarayanan and A. Kar, "Nonlinear effects of laser-plasma interaction on melt-surface temperature," *J. Phys. D. Appl. Phys.* **32** (7) , 777 – 784 (1999).
13. S.S. Harilal, B.E. Brumfield, N.L. Lahaye, K.C. Hartig, and M.C. Phillips, "Optical spectroscopy of laser – produced plasmas for standoff isotopic analysis," *Appl. Phys. Rev* **5**, 021301 (2018).
14. R.A. Ganeev, "High-order harmonic generation in a laser plasma: a review of recent achievements," *J. Phys. B At. Mol. Opt. Phys.* **40**(22), R213 - R253 (2007).
15. G. Ma, W. Yu, M.Y. Yu, B. Shen, L. Veisz, "Intense circularly polarized attosecond pulse generation from relativistic laser plasmas using few-cycle laser pulses," *Opt. Express* **24**(9), 10057-10065 (2016).
16. S. Amoroso, G. Ausanio, R. Bruzzese, M. Vitiello, and X. Wang, "Femtosecond laser

- pulse irradiation of solid targets as a general route to nanoparticle formation in a vacuum,” *Phys. Rev. B - Condens. Mater. Phys.* **71**, 033406 (2005).
17. F.C. D. Lucia and J. L. Gottfried, “Rapid analysis of energetic and geo-materials using LIBS,” *Mater. Today* **14** (6), 274-281 (2011).
  18. A. Kar and J. Mazumder, “Two-dimensional model for material damage due to melting and vaporization during laser irradiation,” *J. Appl. Phys.* **68**, 3884-3891 (1990).
  19. M. H. Mahdih and M. Akbari Jafarabadi, “Dynamics of optical breakdown in air induced by single and double nanosecond laser pulses,” *Phys. Plasmas* **22**(12), 123117 (2015).
  20. M.H. Mahdih, M.A. Jafarabadi, and D. Katoozi, “Time-resolved optical probing of nanosecond laser-induced breakdown plasma in polymethylmethacrylate (PMMA),” *Appl. Phys. B Lasers Opt.* **124**(26), 1-9 (2018).
  21. J. Solis, J. Siegel, and C. N. Afonso, “Real-time optical measurements with picosecond resolution during laser induced transformations,” *Rev. sci. instrum.* **71**(4), 1595-1601 (2000).
  22. P. A. Naik, V. Arora, Y. B. S. R. Prasad, J. A. Chakera, and P. D. Gupta, “Materials under intense laser irradiation,” in *Materials under extreme conditions*, A. K. Tyagi, S. Banerjee, (Elsevier, 2017).
  23. M. Sheik-bahae, A. A. Said, and E. W. Van Stryland, “High-sensitivity, single beam  $n_2$  measurements,” *Opt. Lett.* **14** (17), 955-957 (1989).
  24. G. Tsigaridas, M. Fakis, I. Polyzos, P. Persephonis, and V. Giannetas, “Z-scan technique through beam radius measurements,” *Appl. Phys. B* **76**, 83-86 (2003).
  25. Q. Wang, A. Chen, H. Qi, S. Li, Y. Jiang and M. Jin, “Femtosecond laser-induced breakdown spectroscopy of a preheated Cu target,” *Opt. laser Technol.* **121**, 105772 (2019).
  26. A. Rahaman, A. Kar, and X. Yu, “Thermal effects of ultrafast laser interaction with polypropylene,” *Opt. Express* **27**(4), 5764-5783 (2019).
  27. H. A. Maddah, “Polypropylene as a promising plastic: A Review,” *Am. J. Polym. Sci.* **6**(1), 1-11 (2016).
  28. M. Asobe, I. Yokohama, and T. Kaino, S. Tomaru and T. Kurihara., “Nonlinear absorption and refraction in an organic dye functionalized main chain polymer waveguide in the 1.5  $\mu\text{m}$  wavelength region,” *Appl. Phys. Lett.* **67**(7), 891-893 (1995).
  29. A.Y. Vorobyev and C. Guo, “Reflection of femtosecond laser light in multipulse ablation of metals,” *J. Appl. Phys.* **110**, 043102 (2011).
  30. O. Benavides, O. Lebedeva, and V. Golikov, “Reflection of nanosecond Nd:YAG laser pulses in ablation of metals”, *Opt. Express* **19**(24), 21842 – 21848 (2011).
  31. S. Polyakov, T. Pauchard, G. Stegeman, J. Berréhar, and M. Schott, “Two photon absorption and photo-induced polymerization in partially polymerized crystals of polydiacetylene poly [4,6-dodecadiyn-1, 10-diol-bis(*n*-butoxycarbonylmethylurethane),” *J. Chem. Phys.* **118**, 4341-4344 (2003).

32. W. M. K. P Wijekoon, K. S. Lee, and P. N. Prasad, "Nonlinear Properties of Polymers," in *Physical Properties of Polymers Handbook*. J. E. Mark, (Springer, 2007).
33. H. Zhang, F. Zhang, X. Du, G. Dong, and J. Qiu, "Influence of laser-induced air breakdown on femtosecond laser ablation of aluminum," *Opt. Express* **23**(2), 1370-1376 (2015).
34. H. Mlejnek, M. Kolesik, J. V. Moloney, and E. M. Wright, "Optically turbulent femtosecond light guide in air," *Phys. Rev. Lett.* **83**, 2938-2941 (1999).
35. V. V. Bukin, S. V. Garnov, A. A. Malyutin, and V. V. Strelkov, "Femtosecond laser optical breakdown microplasma: the ionisation and postionisation dynamics," *Quantum Electron* **37**(10), 961-966 (2007).
36. A. E. Martirosyan, C. Altucci, A. Bruno, C. de Lisio, A. Porzio, and S. Solimeno, "Time evolution of plasma afterglow produced by femtosecond laser pulses," *J. Appl. Phys.* **96**(10), 5450-5455 (2004).

# **CHAPTER 5: MECHANISMS OF ULTRAFAST LASER INTERACTION WITH OPAQUE AND TRANSPARENT POLYPROPYLENE**

## 5.1 Introduction

The interaction of intense ultrafast laser pulses with materials, including dielectrics (such as polymers, glass, etc.), semiconductors, and metals leads to applications such as precision micro/nano-processing [1-5]. Ultrafast laser pulses have the ability to confine energy deposition in a small region, which offers precision, flexibility, and robustness in various types of laser material processing including drilling [6], cutting [7], surface hardening [8], polishing [9,10], cleaning [11] and micro/nano machining [12,13]. However, material processing with ultrafast laser is complicated as various linear and nonlinear mechanisms are involved [14]. In terms of the interaction between ultrashort laser pulses with matters, many challenging fundamental problems remain unanswered [15,16]. Specifically, ultrafast laser processing of polymers with high precision and control is still challenging due to the dynamic behavior of the interaction of ultrashort pulses with polymers. Therefore, it is important to have a better understanding of the dynamics of ultrafast laser interaction with different polymers to make ultrafast laser compatible with polymer processing in science and industrial applications.

The dynamics of ultrafast laser interaction with polymeric material is intricate due to different photo-physical, photo-thermal, photochemical, mechanical, and optical properties and the effect of plasma plume for different polymers [17]. The dynamics of ultrafast laser-material interaction depends on different laser parameters, such as pulse duration, laser wavelength, intensity, temporal and spatial pulse shape, pulse repetition rate (PRR), ambient environment, and material properties [18,19]. To understand the dynamic of the interaction of ultrafast laser pulses

with polymers, researchers have focused on both experimental and theoretical studies to develop ultrafast laser material processing for various applications [20-22]. The dynamics of ultrafast laser interaction with polymers remains controversial among researchers in near-infrared wavelengths. In addition, optical properties of the material such as reflectance, transmittance, and absorptance become fluence (intensity) dependent for high pulse energies, and therefore these are crucial in selecting laser processing parameters. In our previous study, the time-resolved single-shot measurement was performed to determine the reflectance, transmittance, and absorptance in ultrafast laser interaction with opaque polypropylene (PP), which contains a small amount of several impurities such as Si, C, Li, Na, Al, K, and SiO<sub>2</sub>, for a wide range of laser pulse energy [23]. Polypropylene has a wide range of applications including packaging for consumer products (medical industry), plastic parts for various industries (including automotive industry), and special devices like hinges, household products, battery cases, and fabrics [24]. However, the mechanism of ultrafast laser processing is different for transparent and opaque PP, where opaque PP mostly reflects and absorbs irradiated laser energy as opaque PP contains different pigments, which can be organic or inorganic [25].

In this study, the dynamics behavior of ultrafast laser interaction with transparent and opaque PP is observed experimentally by performing time-resolved measurement of optical properties in ultrafast laser interaction with PP. The experiment is performed in a single-shot configuration in near-infrared wavelength of ultrafast laser and an ellipsoidal mirror is used to collect both specular and diffusive reflection. It is found that the mechanisms responsible for processing transparent and opaque PP are distinct from each other, which are confirmed with different experimental tests, and the experimental results are explained with a model that accounts



for both linear and non-linear absorptions. This study will help to understand possible micro/nano processing of polymers for both transparent and opaque PP with a near-infrared ultrafast laser.

## 5.2 Experimental design

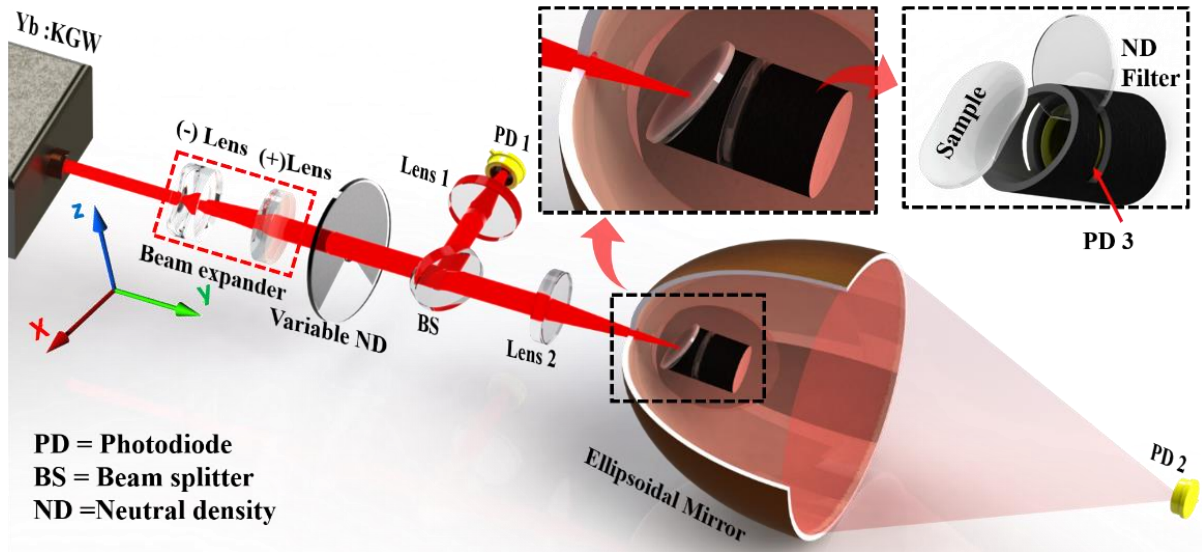


Figure 5.1: Schematic for experimental set up for measuring optical properties of ultrafast laser interaction with transparent material

In this study, a Yb: KGW (Pharos, Light Conversion) femtosecond laser is used, which delivers ultrafast laser pulses of pulse duration 170 fs with the central wavelength of 1030 nm. Single-shot measurements are performed to determine the reflectance,  $R$ , transmittance,  $T$ , and absorptance,  $A$ , in the ultrafast laser interaction with white opaque PP sheet, which mostly reflects and absorbs irradiated laser energy, and transparent PP sheet, which transmits most of the light, when the laser intensity is low.

Fig. 5.1 shows an experimental setup for time-resolved measurements of  $R$  and  $T$ . In this system, the diameter of the output femtosecond laser beam is 4 mm, which is enlarged to 10 mm by a beam expander (a combination of negative (-) and positive (+) lenses) and a variable neutral

density (ND) filter is used to adjust pulse energy. The collimated laser beam is splitted in two arms, where 6.5% of the beam is used as the reference arm to determine the incident laser pulse energy, and the other arm is focused with a lens of 250 mm focal length. The diameter of the spot size is measured to be  $36.8 \mu\text{m}$  at  $1/e^2$ -point. For data acquisition, three photodiodes (PD 1-3, Thorlabs, FDS100) and a 1-GHz oscilloscope (Tektronics, MD03104) are used. A home-build fixture is used to hold the sample, PD 3, and 0.5" ND filter, where the PP sheet is placed on the top of the fixture, and both ND and PD 3 are placed after the sample. An ellipsoidal reflector (E180, Optiforms) is used to capture most of the reflected light (both specular and diffusive reflections) from the sample [26, 27] and both specular and diffusive reflections are detected by PD 2, which is located near the external (second) focal point of the ellipsoidal mirror. To reduce the backscattering through the entrance hole of the ellipsoidal mirror, the surface of the normal of the sample is tilted with an angle of  $17^\circ$  with respect to the laser beam. An ND filter is placed after the sample to attenuate the transmitted light from the transparent PP sheet to avoid saturation in PD 3. Detailed procedure on placing the sample at the first focus of the ellipsoidal mirror and placing PD 2 on the second focus of the ellipsoidal mirror is discussed elsewhere [23]. A 3D stage is used to move the sample to ensure a fresh surface for each laser shot. The fixture is attached to the 3D stage from the back of the black fixture, which is shown in the inset of the Fig. 5.1.

### 5.3 Experimental Results to compare opaque and transparent PP

In this experiment, both opaque and transparent PP sheets are irradiated with a single-shot femtosecond pulse with pulse duration 170 fs. Fig. 5.2 shows the laser damages on the front surface of both opaque PP (top row) and transparent PP (bottom row). The top row of Fig. 5.2 shows damages for opaque PP at fluences  $F= 0.19, 1.88, 7.52$  and  $11.3 \text{ J/cm}^2$  for pictures A, B, C and D,

respectively, whereas the bottom row shows damages for transparent PP at  $F = 1.88, 4.70, 9.40$  and  $18.8 \text{ J/cm}^2$  for damage A, B, C and D, respectively. Damage A in both cases corresponds to the damage threshold fluence ( $F_{th}$ ), which is much higher for transparent PP than opaque PP as most of the light transmits through transparent PP. Damage B, C and D indicate that the damage size changes with fluencies/intensities, where damage C and D in top row is found to be nearly the same size. It is obvious from Fig. 5.2 that damage morphology in the opaque PP surface and the transparent PP surface are different, which is discussed next.

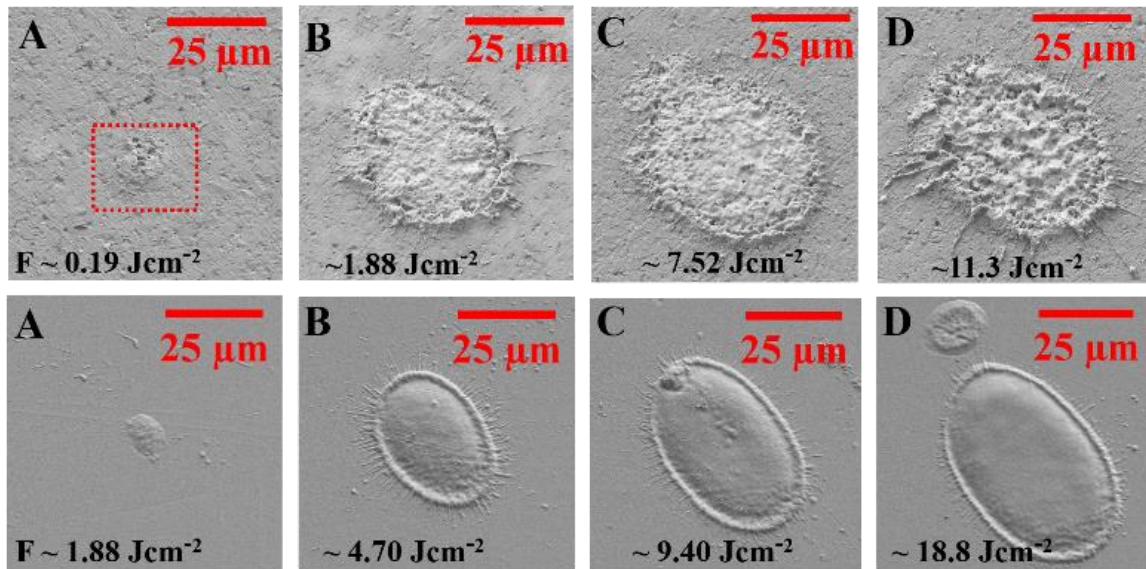


Figure 5.2: Damage observed by scanning electronic microscopy (SEM) on the surface of opaque (top row) and transparent (bottom row) PP sample with different fluences

It can be seen from Fig. 5.2 that craters are observed for opaque PP and dome-like structures are observed for transparent PP. 2D profilometer (Dektak XT, Bruker) measurements are performed to confirm the damage profile, which is shown in Fig. 5.3(a) for both opaque and transparent case. The peak fluences used on opaque (top damage in Fig. 5.3(a)) and transparent PP (bottom damage in Fig. 5.3(a)) are  $9.40 \text{ J/cm}^2$  and  $6.58 \text{ J/cm}^2$ , respectively. The profilometer

measurement shows that the depth of the damage in opaque PP is around 1.5  $\mu\text{m}$  corresponding to the fluence 9.4  $\text{J}/\text{cm}^2$ , where the height of the dome in transparent PP corresponding to the fluence 6.58  $\text{J}/\text{cm}^2$  is 1.1  $\mu\text{m}$ .

Ultrashort laser pulse irradiation leads to the instantaneous heating<sup>28,29</sup> and expansion<sup>30,31</sup> on the surface of the polymers. Micro/nano splashes have been observed on the surface of the PP sample in Fig. 5.3(a) due to localized melting and explosive boiling. After thermalization of the laser energy in the PP sample (on the ps time scale), a two-phase liquid-gas mixture develops, which then undergoes hydrodynamics expansion, arising in material ejection and resolidification on the ns time scale [28, 31, 32]. This creates micro/nano-void as well as dome-shaped swelling [33-35]. The formation of voids near the surface of a transparent PP sample induced by single-shot irradiation with femtosecond laser with duration 170 fs is confirmed with focused ion beam (FIB) milling, which is shown in Fig. 5.3(b-d). The cross-sectional analysis of a transparent PP sample with FIB milling (pulse energy 20  $\mu\text{J}$ ) is shown in Fig. 5.3(c,d) to observe the formation of voids. The diameter of these voids increases with the irradiated pulse energy and the diameter of these voids is between 0.2 to 3  $\mu\text{m}$  corresponding to the pulse energy from 12.5  $\mu\text{J}$  to 100  $\mu\text{J}$ . Fig. 5.3(d) shows the central part of irradiated place on the surface of the sample, where the size of the voids is larger and also the density of the voids is higher. It can be seen from the right side of Fig. 5.3 (c) that there is no void, where the surface of the sample is not irradiated with a laser pulse.

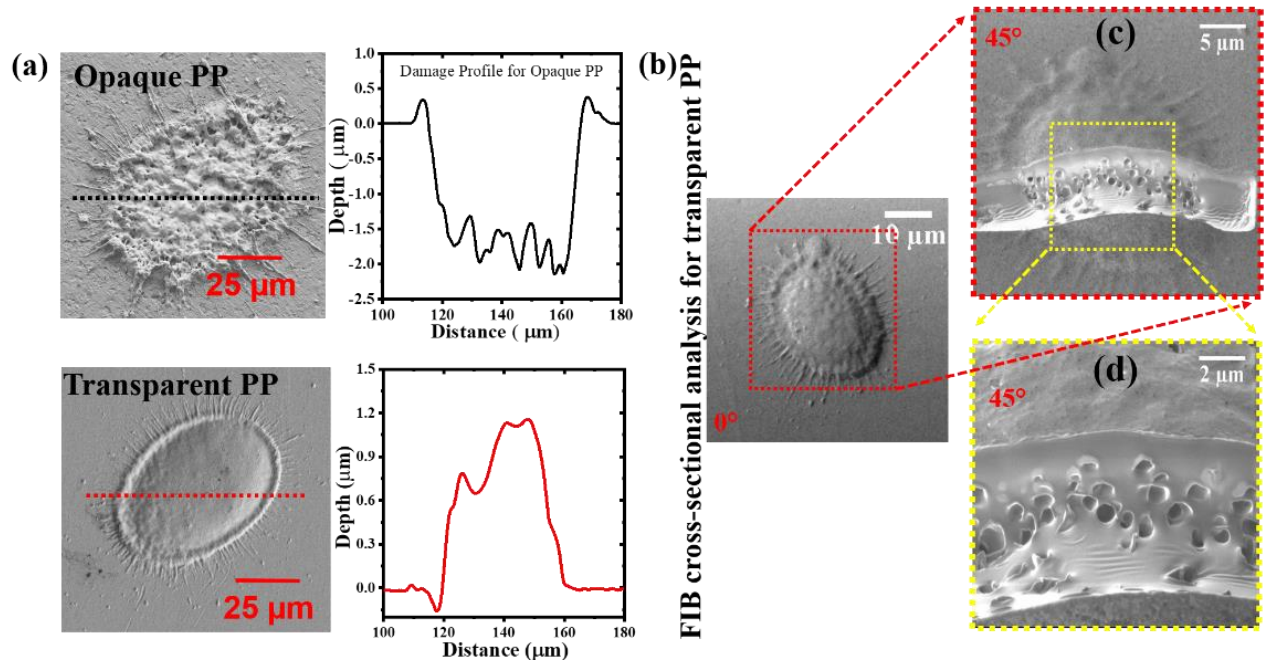


Figure 5.3: (a) SEM images of the damage in opaque (top) and transparent (bottom) surface, and its corresponding damage profile on the surface of the material. (b-d) Cross-sectional analysis of transparent PP sample with FIB (focused ion beam) milling, which is irradiated with pulse energy 20 μJ.

The experimental value of total reflectance (specular and diffusive) for transparent PP,  $R_{tr}$  and opaque PP,  $R_{op}$ , the transmittance of transparent PP,  $T_{tr}$  and opaque PP,  $T_{op}$  and the absorptance of transparent PP,  $A_{tr}$  and opaque PP,  $A_{op}$  are shown in Fig. 5.4. The transmittance and reflectance are determined from the integrated areas at FWHM of the PD traces obtained from the 1-GHz oscilloscope for reflected and transmitted light. The determination of transmittance and reflectance is explained elsewhere [23]. Absorptance of the material for a wide range of the peak fluence is calculated as  $A = 1 - T - R$ . Fig. 5.4 shows that both reflectance,  $R_{tr}$  and  $R_{op}$  remain constant at around 0.6 and 0.044, respectively, as the material surface does not undergo any change until  $F = 0.19 \text{ J/cm}^2$  and  $1.88 \text{ J/cm}^2$  (which are shown in Fig. 5.3, first damage picture in top and bottom row) for opaque and transparent PP, respectively. The peak fluence of the damage threshold

for transparent PP is much higher than the opaque PP as most of the light transmits through the sample for transparent PP. Similarly, the transmittance and the absorbance remain constant until the damage threshold peak fluence is reached. This constant region is defined as a “linear absorption region”. However, the reflectance and transmittance start to drop due to the non-linear absorption mechanisms as the peak fluence increases, which is explained more details in the next section. However, the reflectance and transmittance show very random behavior at very high fluence  $F > 10 \text{ J/cm}^2$  and absorbance can be seen to decrease with increasing fluence. Note that the maximum fluence used in this study for opaque and transparent PP sample are 15.04 and 18.8  $\text{J/cm}^2$ , respectively.

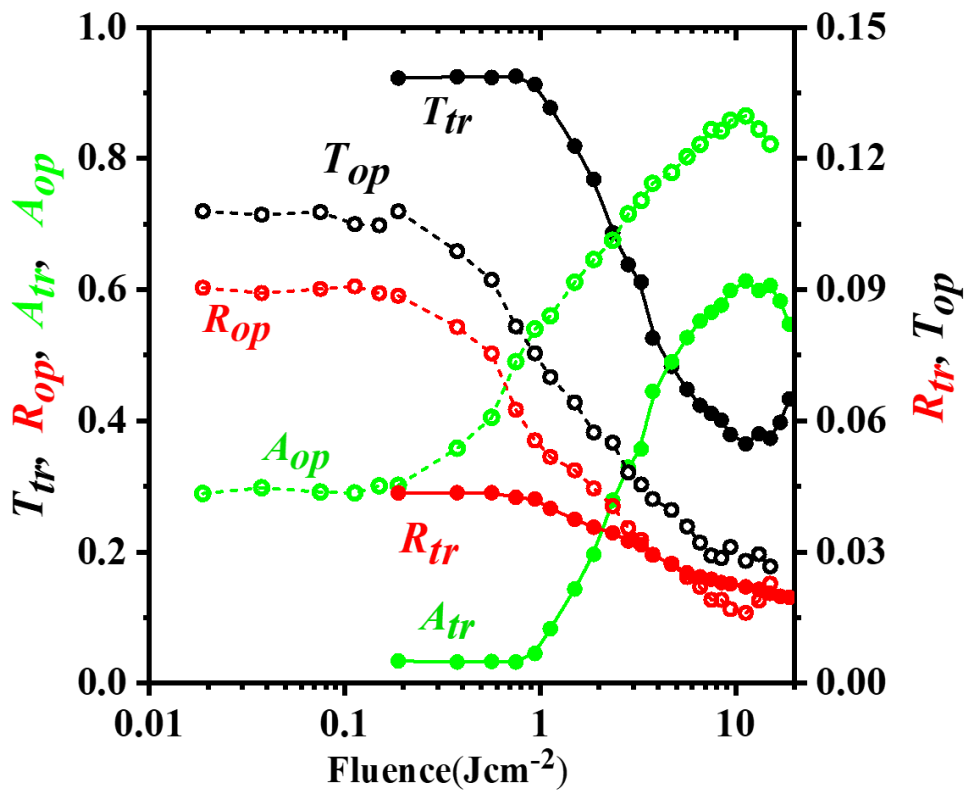


Figure 5.4: Reflectance, transmittance, and absorbance for transparent PP sample are  $R_{tr}$ ,  $T_{tr}$ , and  $A_{tr}$ , respectively and  $R_{op}$ ,  $T_{op}$ , and  $A_{op}$  for opaque PP, respectively, as functions of laser fluence and intensity

## 5.4 Model and discussion

To make ultrafast lasers compatible with polymer processing, it is required to understand the dynamic behavior of ultrashort pulse with a polymeric material and relative significance of different linear and nonlinear absorption processes. However, the fundamental understanding of ultrafast laser interaction with polymers in near-infrared (NIR) wavelength is still lacking. The absorption mechanism of ultrashort laser pulses during polymer processing with NIR wavelength is both linear (single-photon) and nonlinear (multi-photon) processing [23,36] due to vibrational overtone or combination absorption [37]. The equation, which describes the attenuation of the ultrafast laser pulse  $I(r, z, t)$  passing through the material undergoing single-photon, two-photon or two – steps or three-photon or three-steps absorption is given by

$$\frac{dI(r_i, z_i, t)}{dz_i} = -\alpha_1 I(r_i, z_i, t) - \alpha_2 I^2(r_i, z_i, t) - \alpha_3 I^3(r_i, z_i, t) \quad (5.1)$$

Where  $\alpha_1$ ,  $\alpha_2$  and  $\alpha_3$  are the linear, two-photon, or two-steps nonlinear and three-photon or three-steps nonlinear absorption coefficient, respectively. Fig. 5.5 shows the multiple reflections of initial incoming intensity,  $I_{0I}(r, 0, t)$  at different surfaces, where

$$I_{0I}(r, 0, t) = I_0 e^{-\frac{2r^2}{\omega_0^2}} e^{-4\ln 2 \frac{t^2}{t_{0n}^2}} \quad (5.2)$$

Where  $\omega_0$  and  $t_{0n}$  are the radius of the spot size at the focus and the duration of the femtosecond laser pulse, respectively.

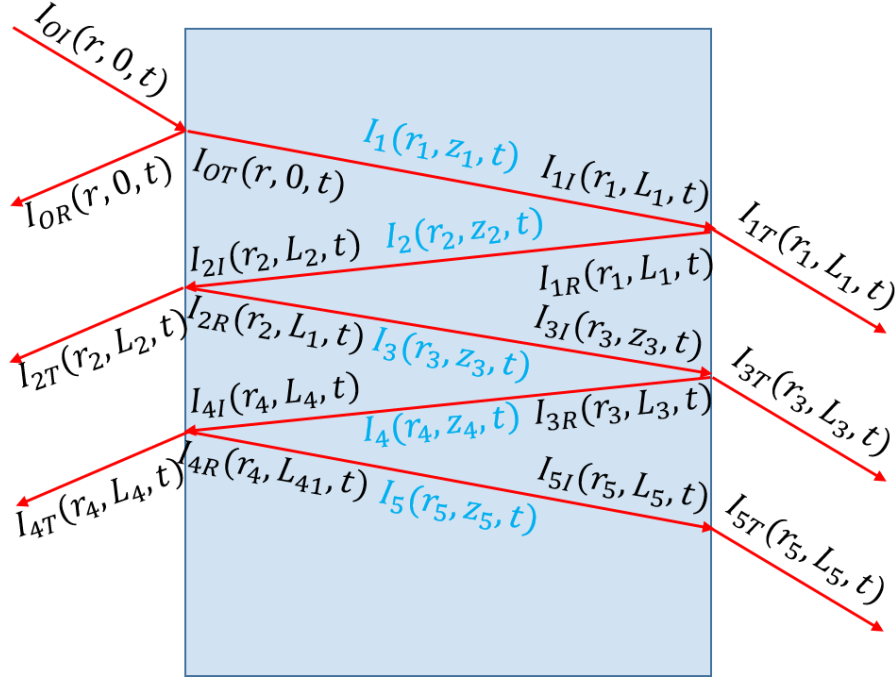


Figure 5.5: The multiple reflection is considered as an inclined laser beam that is irradiated on the sample.

The analytical solution of the above differential equation after passing through the material can be expressed as

$$I_{iI}(r_i, z_i, t) = \frac{1}{3a_i(r_i, z_i, t)} \left( Q_i(r_i, z_i, t) + \frac{\Delta_{oi}(r_i, z_i, t)}{Q_i(r_i, z_i, t)} - b_i(r_i, z_i, t) \right) \quad (5.3)$$

where  $I_{iI}(r_i, L_i, t)$  is the incident intensity at the different interfaces except for the first incident point. All the variables in the above equation are defined in appendix 5.8.

The total transmitted intensity at the exit side of the sample is given by

$$I_T(r, z, t) = \sum_{m=0}^{\infty} I_{(2m+1)T}(r_{(2m+1)}, L_{(2m+1)}, t) \quad (5.4)$$

Here, the transmitted light at each of the points are  $I_{iT}(r_i, L_i, t)$ .



The transmittance,  $T$  of the ultrafast laser pulse through the PP sample can be found from the above solution in Eq. (5.1), which can be expressed in term of output pulse energy,  $E_{out}$  and input pulse energy,  $E_{in}$  as below:

$$T = \frac{E_{out}}{E_{in}} = \frac{2\pi}{E_{in}} \int_0^{\infty} \int_{-t_{on}}^{t_{on}} I_T(r, z, t) r dr dt \quad (5.5)$$

Fig. 5.6 shows the experimental results which are fitted with theoretical calculation, where transmittance, as well as absorptance, can be divided into three regions (Region I, Region II and Region III) of peak fluence or peak intensity. Here, Region I represents the linear absorption region, where transmittance remains nearly constant up to the damage threshold peak fluence,  $F$ , which are  $0.15 \text{ J/cm}^2$  and  $0.94 \text{ J/cm}^2$  for opaque and transparent PP, respectively. After the damage threshold peak fluence, transmittance decrease as peak fluence increases, which is shown in Fig. 5.5 and region II for both opaque and transparent PP cases. The decrease in transmittance as peak fluence increases is indicative of nonlinear interaction of PP samples and ultrafast laser pulses. Experimental results in region III are mostly random, which is not dependent on peak fluence or peak intensity.

Fig. 5.7 shows the absorption spectrum of transparent PP sample, which indicates vibrational overtone/combination non-resonant absorption at 1030 nm and 515 nm, respectively, and resonant absorption peak around 353 nm and 373 nm which suggests nonlinear absorption in Region II [23,37].

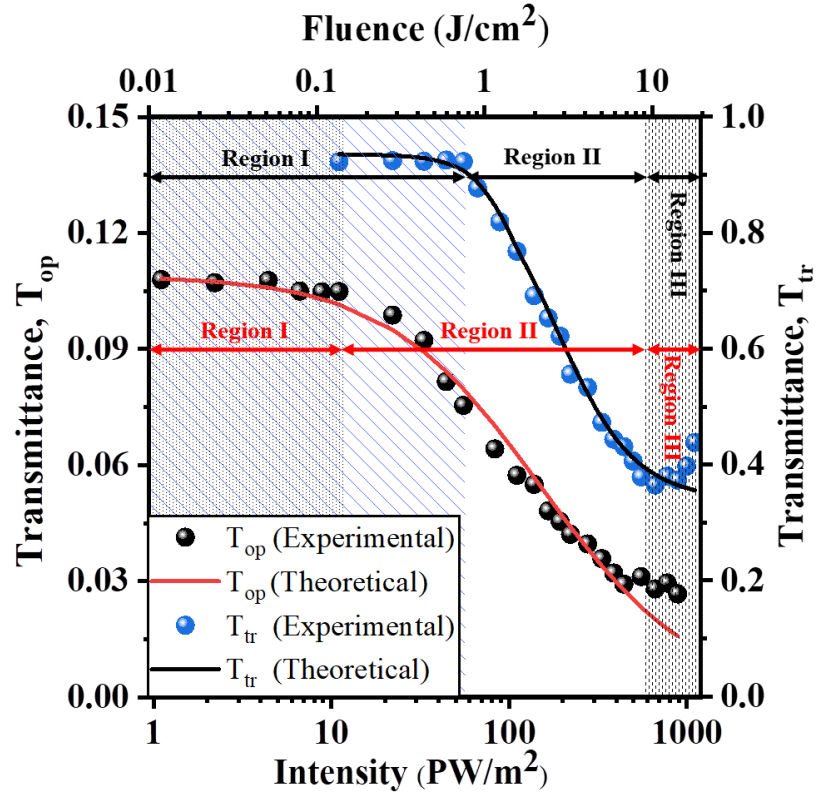


Figure 5.6: (a) Fitting of the experimental results for opaque PP sample and transparent PP sample. The laser intensity used in this experiment can be divided into three regions (Region I, II, and III).

The absorption coefficient for single-photon (linear), two-steps, or two-photon (nonlinear) and three-steps or three-photon (nonlinear) is determined from the fitting of experimental data with numerical values of Eq. (5.5). The linear absorption coefficient  $\alpha_1$  are found to be  $\alpha_1 = (110.85 \pm 3) \text{ m}^{-1}$ , which agrees with the experimental value for the thickness of the transparent sample,  $L = 450 \text{ }\mu\text{m}$ . The nonlinear absorption coefficient for two-steps or two-photon and three-steps and three-photon are found to be  $\alpha_2 = (7.14 \pm 2.09) \times 10^{-13} \text{ mW}^{-1}$  and  $\alpha_3 = (3.31 \pm 1.5) \times 10^{-29} \text{ m}^3 \text{W}^{-2}$ , respectively, for transparent PP. The nonlinear refractive indexes are determined from the fitting are  $n_2 = (3.32 \pm 1.11) \times 10^{-20} \text{ m}^2 \text{W}^{-1}$ , and  $n_3 = (2.69 \pm 0.36) \times 10^{-37} \text{ m}^4 \text{W}^{-2}$ , where the linear refractive index is 1.49. Determining the absorption coefficients and nonlinear refractive indexes will be

discussed in detail in Chapter 6 and Chapter 7. The absorption coefficients and nonlinear refractive indexes are consistent with previously found values for polymers [38, 39]. Similarly, the linear (single-photon) and two-steps or two-photon absorption coefficient for opaque PP are found to be  $\alpha_1 = 5269 \text{ m}^{-1}$  and  $\alpha_2 = 1.391 \times 10^{-13} \text{ mW}^{-1}$ . The absorption spectrum for opaque PP sample can be found in our publication [23], where the peaks at 1030 nm indicate the vibrational overtone or combination absorption of the incident laser photons and the peak at 515 nm provides a mechanism for two-step or two-photon overtone or combination absorption.

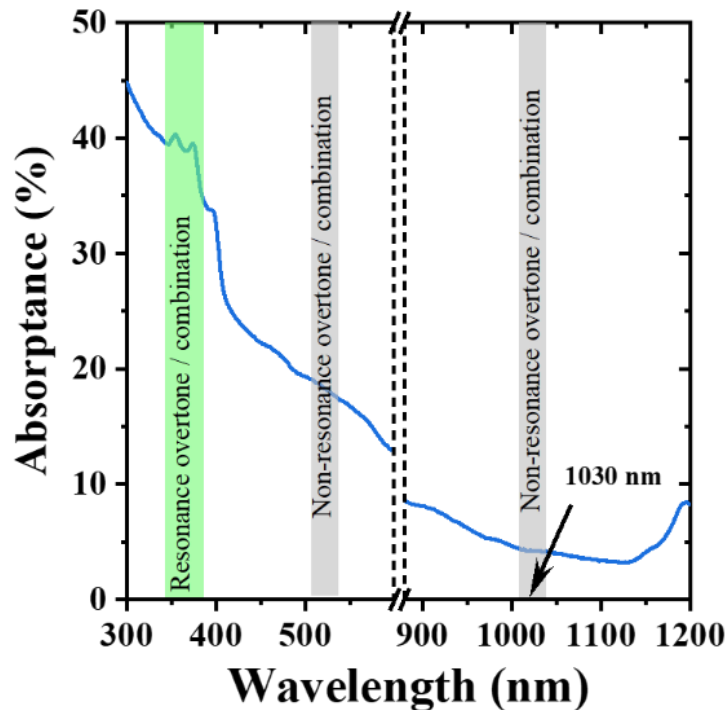


Figure 5.7: Absorbance,  $A$ , of transparent PP sample is determined from the transmittance,  $T$ , and the specular reflectance measurement,  $R_s$ , by using linear spectroscopic measurement.

## 5.5 Self-phase modulation (SPM) responsible for wavelength shift

When a high-intensity laser pulse propagates through a nonlinear medium, an ultrashort pulse accumulates the temporal phase as it propagates, which is known as self-phase modulation (SPM), which is a nonlinear phenomenon due to nonlinear refractive index change inside the medium. The theoretical framework of the self-phase modulation effect can be described by the time-dependent angular frequency,  $\omega(t)$  is defined as

$$\omega(t) = \frac{d\varphi(t)}{dt} \quad (5.6)$$

where the temporal phase,  $\varphi(t) = \omega_0 t - k_0 n(t)z$  and  $n(t)$  is the time nonlinear refractive index which can be defined as below

$$n(t) = n_1 + \Delta n = n_1 + n_2 I(t) + n_3 I^2(t)$$

Substituting  $n(t)$  and  $\varphi(t)$  into equation (1)

$$\omega(t) = \omega_0 - \frac{2\pi}{\lambda_0} n_2 z \frac{dI(t)}{dt} - \frac{4\pi}{\lambda_0} n_3 z I(t) \frac{dI(t)}{dt} \quad (5.7)$$

where  $\omega(t) = \frac{2\pi c}{\lambda(t)}$  and  $\lambda(t)$  is the instantaneous wavelength. After solving  $\lambda(t)$  from the above equation (2),  $\lambda(t)$  express can be written as

$$\lambda(t) = \frac{\lambda_0}{1 - \frac{n_2 z}{c} \frac{dI(t)}{dt} - \frac{2n_3 z I(t)}{c} \frac{dI(t)}{dt}} \quad (5.8)$$

where  $\frac{dI(t)}{dt}$  is the slope of the temporal laser pulse.

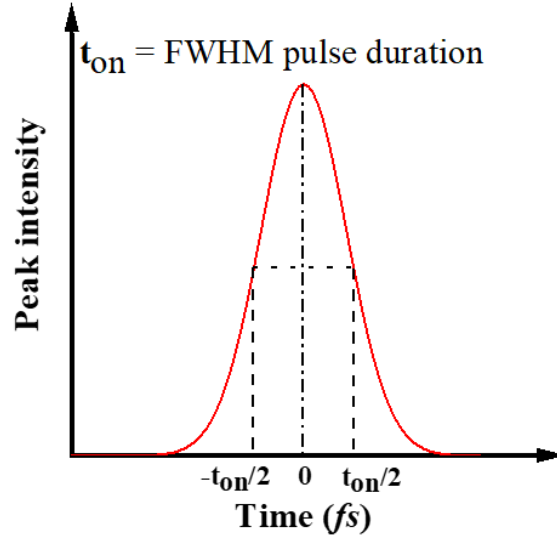


Figure 5.8: Schematic of the temporal Gaussian pulse

Therefore, the wavelength shifting due to high-intensity laser pulse can be written as below

$$\lambda(t) - \lambda_o = \lambda_o \left( \frac{n_2 \frac{dI(t)}{dt} + 2n_3 I(t) \frac{dI(t)}{dt}}{\frac{c}{z} - n_2 \frac{dI(t)}{dt} - 2n_3 I(t) \frac{dI(t)}{dt}} \right) \quad (5.9)$$

The above equation (4) can be used to calculate wavelength shift during the ultrafast laser interaction with polypropylene for different peak intensities at different depths inside the sample.

The fundamental wavelength used in this study is 1030 nm, so the third-harmonic of the fundamental wavelength could be around 343 nm. However, the absorption peak from linear spectroscopic measurement is found to be at 353 nm and 373 nm. Fig. 5.9 shows the wavelength shift due to the slope of the temporal pulse at different times,  $t = -\frac{t_{on}}{2}$ ,  $t = 0$ , and  $t = \frac{t_{on}}{2}$ .

The maximum wavelength shift corresponding to the maximum peak intensity 1061 PW/m<sup>2</sup> is found to be around  $\pm 30$  nm, which covers both peaks at 353 nm and 373 nm. Therefore, three-steps or three-photon absorption are suggested to have happened through vibrational overtone absorption mechanism by shifting wavelength at a very high intensity of the laser beam.

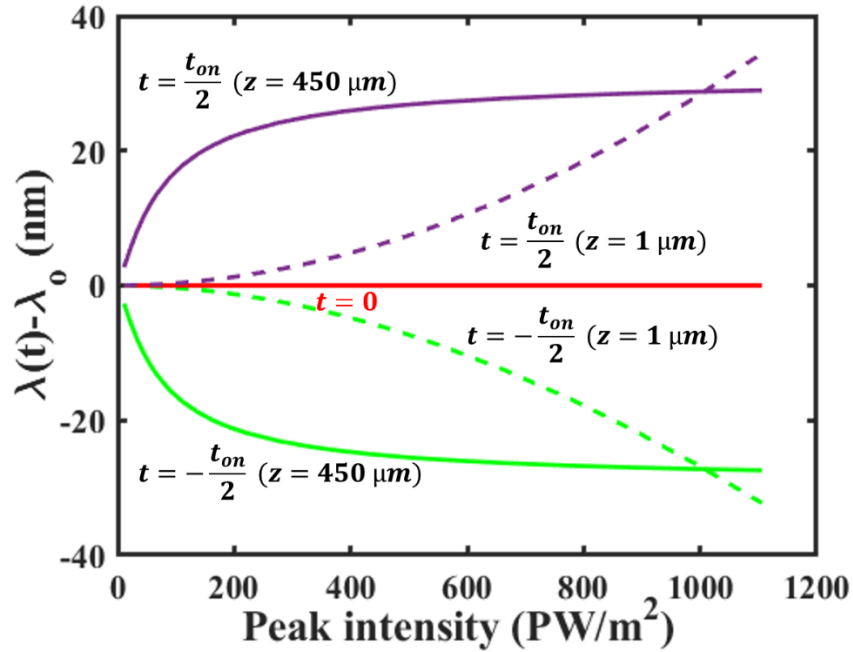


Figure 5.9: The wavelength shifting with various intensity at different slope values of the intense temporal pulse.

## 5.6 Summary

In summary, time-resolved measurements of optical properties, i.e. reflectance, transmittance, and absorptance, are performed for a wide range of intensities to understand the dynamics of the ultrafast laser interaction with transparent and opaque PP. We observe micro/nano voids formation under the surface of the sample when ultrafast laser pulses are irradiated on transparent PP, which leads to the formation of swelling at the irradiated surface. The experimental results are explained with a model that accounts for both linear and nonlinear absorption and nonlinear absorption coefficients are estimated from this model. This study provides information that will help to understand possible micro/nano processing of polymeric material with an ultrafast laser.

## 5.7 References

1. K. Sugioka and Y. Cheng, "Ultrafast lasers - reliable tools for advance materials processing", *Light Sci. Appl.* **3**, e149 (2014).
2. W. Sibbett, A. A. Lagatsky, and C. T. A. Brown, "The development and application of femtosecond laser systems," *Opt. Express* **20**(7), 6989 - 7001 (2012).
3. A. Rahaman, X. Du, B. Zhou, H. Cheng, A. Kar, and X. Du, "Absorption and temperature distribution during ultrafast laser micro-cutting of polymeric materials" *J Laser Appl.*, **32**, 022044 (2020).
4. R.R. Gattass and E. Mazur, "Femtosecond laser micromachining in transparent materials," *Nat. Photonics* **2**, 219 - 225(2008).
5. B. Zhou, A. Rahaman, X. Du, H. Cheng, Y. Chai, A. Kar, M. J. Soileau, and X. Yu, "Optical breakdown and sub-optical-cycle dynamics of ultrafast laser-induced damage in fused silica" in *Laser-based Micro-and Nanoprocessing XIII*, Vol. 10906 of Proc. SPIE (International Society for Optics and Photonics, 2019), 109061R.
6. X. Zhao, and Y.C. Shin, "Femtosecond laser drilling of high - aspect ratio microchannels in glass," *Appl. Phys. A* **104**, 713 (2011).
7. A. N. Fuchs, M. Schoeberl, J. Trimmer, and M.F. Zaeh, "Laser cutting of carbon fiber fabrics," *Phys. Procedia* **41**, 372 - 280 (2013).
8. A. K. Nath, A. Gupta, and F. Benny, "Theoretical and experimental study on laser surface hardening by repetitive laser pulses," *Surf. Coat. Tech.* **206**(8-9), 2602 - 2615 (2012).
9. M. Malinauskas, A. Žukauskas, S. Hasegawa, Y. Hayasaki, V. Mizeikis, R. Buividas and S. Juodkazis, "Ultrafast laser processing of materials: from science to industry," *Light Sci. Appl.* **5**(8), 1-14 (2016).
10. L. L. Taylor, J. Xu, M. Pomerantz, T. R. Smith, J. C. Lambropoulos, and J. Qiao, "Femtosecond laser polishing a germanium," *Opt. Express* **9**, 4165 - 4177 (2019).
11. T. Ersoy, T. Tunay, M. Uğuryol, G. Mavili, and S. Akturk, "Femtosecond laser cleaning of historical paper with sizing," *J. Cult. Herit.* **15**(3), 258- 265 (2014).
12. W. Jia, Y. Luo, J. Yu, B. Liu, M. Hu, L. Chai, and C. Wang, "Effects of high-rate femtosecond laser micromachining on the physical and chemical properties of polylactide (PLA)," *Opt. Express* **23**(21), 26932 - 26939 (2015).
13. J. Cheng, C. S. Liu, S. Shang, D. Liu, W. Perrie, G. Dearden, K. Watkins, " A review of ultrafast laser materials micromachining" *Opt. Laser. Technol.* **46**, 88-102(2013).
14. R. Menzel, *Photonics: Linear & nonlinear interactions of laser light and matter* (Springer, 2007).

15. K. Sugioka, "Progress in ultrafast laser processing and future prospects," *Nanophotonics* **6**(2), 393 – 413 (2017).
16. M. V. Shugaev, C. Wu, O. Armbruster, A. Naghilou, N. Brouwer, D. S. Ivanov, T. J. Y. Derrien, N. M. Bulgakova, W. Kautek, B. Rethfeld and L. V. Zhigilei, "Fundamentals of ultrafast laser-interaction," *MRS Bull.* 41(12), 960 – 968 (2016).
17. B. Stepak, M. Gazinska, M. Nejbauer, Y. Stepanenkko, and A. Antonczak, "Diverse nature of femtosecond laser ablation of poly(L-lactide) and the influence of filamentation on the polymer crystallization behavior," *Sci. Rep.* **9**, 3069(2019).
18. M. Benton, M. R. Hossan, P. R. Konari, and S. Gamagedara, "Effect of process parameters and material properties on laser micromachining of microchannels," *Macromachines* **10** (2), 123(2019).
19. M. H. Mahdih and M. Akbari Jafarabadi, "Dynamics of optical breakdown in air induced by single and double nanosecond laser pulses," *Phys. Plasmas* **22**(12), 123117 (2015).
20. A. Rahaman, A. Kar, and X. Yu, "Thermal effects of ultrafast laser interaction with polypropylene," *Opt. Express* **27**(4), 5764-5783 (2019).
21. J. Kruger, W. Kautek, "Ultrashort pulse laser interaction with dielectrics and polymers," in *Polymer and Light*, T. K. Lippert, ed. (Springer, 2004).
22. A. E. Martirosyan, C. Altucci, A. Bruno, C. de Lisio, A. Porzio, and S. Solimeno, "Time evolution of plasma afterglow produced by femtosecond laser pulses," *J. Appl. Phys.* **96**(10), 5450-5455 (2004).
23. A. Rahaman, A. Kar, and X. Yu, "Time-resolved measurements of optical properties in ultrafast laser interaction with polypropylene" *Opt. Express*, 28(2), 2640-2648(2020).
24. H. A. Maddah, "Polypropylene as a promising plastic: A Review," *Am. J. Polym. Sci.* **6**(1), 1-11 (2016).
25. A. Riveiro, R. Soto, J. del Val, R. Comesana, M. Boutinguiza, F. Quintero, F. Lusquinos, and J. Pou, "Texturing of polypropylene (PP) with nanosecond lasers," *Appl. Sur. Sci.* **374**, 379-386(2016).
26. A. Y. Vorobyev and C. Guo, "Reflection of femtosecond laser light in multipulse ablation of metals," *J. Appl. Phys.* **110**(4), 043102 (2011).
27. O. Benavides, O. Lebedeva, and V. Golikov, "Reflection of nanosecond Nd:YAG laser pulses in ablation of metals," *Opt. Express* **19**(22), 21842–21848 (2011).
28. F. Baset, A. Villafranca, J. M. Guay and R. Bhardwaj, "Femtosecond laser induced porosity in poly-methyl methacrylate" *Appl. Sur. Sci.*, **282**, 729-734(2013).



29. V. V. Zhakhovskil, K. Nishihara, S. I. Anisimov and N. A. Inogamov, “Molecular-dynamics simulation of rarefaction waves in media that can undergo phase transitions” *JETP Let.*, **71**(4), 167-172 (2000).
30. F. Baset, K. Popov, A. Villafranca, J. M. Guay, Z. A-Rekabi, A. E. Pelling, L. Ramunno and R. Bhardwaj, “femtosecond laser induced surface swelling in poly-methyl methacrylate” *Opt. Express* **21**(10), 12527- 12538(2013).
31. S. Lai, M. Ehrhardt, P. Lorenz, D. Hirsch, J. Zajadacz, J. Lu, B. Han and K. Zimmer, “Submicron bubbles/voids formation in the subsurface region of soda-lime glass by single pulse fs laser-induced spallation” *Appl. Sur. Sci.* **502**, 144134(2019).
32. S. I. Anisimov, N. A. Inogamov, A. M. Oparin, B. Rethfeld, T. Yabe, M. Ogawa, and V. E. Fortov, “Pulsed laser evaporation: Equation-of-state effects,” *Appl. Phys. A* **69**, 617–620 (1999).
33. E. G. Gamaly, S. Juodkazis, H. Misawa, B. L. Davies, A. V. Rode, L. Hallo, P. Nicolai, and V. T. Tikhonchuk, “Formation of nano-voids in transparent dielectrics by femtosecond lasers” *Appl. Phys.* **8**, 412-415 (2008).
34. F. Baset, K. K. Popov, A. Villafranca, J. M. Guay, Z. Al-Rekabi, A. E. Pelling, L. Ramunno and R. Bhardwaj, “Femtosecond laser induced surface swelling in poly-methyl methacrylate” *Opt. Express* **21**(10), 12527-12538(2013).
35. J. Li, W. Wang, X. Mei, X. Sun, and A. Pan, “The formation of convex microstructures by laser irradiation of dual-laser polymethymethacrylate (PMMA),” *Opt. Laser Technol.* **106**, 461-468 (2018).
36. T. Viertel, L. Pabst, M. Olbrich, R. Ebert, A. Horn and H. Exner, “Generation of nano-voids inside polylactide using femtosecond laser radiation” *Appl. Phys. A* **123**, 789(2017).
37. M. Asobe, I. Yokohama, T. Kaino, S. Tomaru, and T. Kurihara, “Nonlinear absorption and refraction in an organic dye functionalized main chain polymer waveguide in the 1.5  $\mu\text{m}$  wavelength region” *Appl. Phys. Lett.* **67**, 891 (1995).
38. T. Chang, X. Zhang, X. Zhang, and H. L. Cui, “Accurate determination of dielectric permittivity of polymer from 75 GHz to 1.6 THz using both S- parameters and transmission spectroscopy” *Appl. Opt.* **56**, 3287 (2017).
39. C. Schnebelin, C. Cassagne, C. B. D. Araujo, and G. Boudebs, “Measurements of the third- and fifth-order optical nonlinearities of water at 532 and 1064 nm using the  $D4\sigma$  method” *Opt. Lett.* **39**, 5046 (2014).

## 5.8 Appendix

The differential equation (5.1) can be written as below

$$\frac{dI(r_i, z_i, t)}{dz_i} = -\alpha_1 I(r_i, z_i, t) - \alpha_2 I^2(r_i, z_i, t) - \alpha_3 I^3(r_i, z_i, t) \quad (5.10)$$

After performing integration, Eq. (5.10) can be written as a general cubic equation as below

$$a_i I^3(r_i, z_i, t) + b_i I^2(r_i, z_i, t) + c_i I(r_i, z_i, t) + d_i = 0 \quad (5.11)$$

Where  $a_i$ ,  $b_i$  and  $c_i$  can be expressed as below

$$\begin{aligned} a_i(r_i, z_i, t) &= \frac{2\alpha_3}{\alpha_1} - \frac{2\alpha_3^2}{\alpha_1^2} k_i(r_i, z_i, t) \\ b_i(r_i, z_i, t) &= N - \left( \frac{\alpha_2 \alpha_3}{\alpha_1^2} + \frac{\alpha_3 M}{\alpha_1} \right) k_i(r_i, z_i, t) \\ c_i(r_i, z_i, t) &= - \left( \frac{2\alpha_3}{\alpha_1} + \frac{\alpha_2 M}{\alpha_1} \right) k_i(r_i, z_i, t) \\ d_i(r_i, z_i, t) &= -M k_i(r_i, z_i, t) \end{aligned} \quad (5.12)$$

Here, M, N, and k are

$$\begin{aligned} M &= \frac{\alpha_2}{\alpha_1} - \frac{\alpha_2}{\alpha_1} \sqrt{1 - \frac{4\alpha_1 \alpha_3}{\alpha_1^2}} \\ M &= \frac{\alpha_2}{\alpha_1} + \frac{\alpha_2}{\alpha_1} \sqrt{1 - \frac{4\alpha_1 \alpha_3}{\alpha_1^2}} \end{aligned}$$

$k_i(r_i, z_i, t)$

$$= \frac{\left(\frac{2\alpha_3}{\alpha_1} I^3(r_i, z_i, t) + NI^2(r_i, z_i, t)\right) e^{-2\alpha_1 z_i}}{\frac{2\alpha_3}{\alpha_1} I(r_i, z_i, t) + \frac{2\alpha_3\alpha_2}{\alpha_1^2} I^2(r_i, z_i, t) + \frac{2\alpha_3^2}{\alpha_1^2} I^3(r_i, z_i, t) + \frac{\alpha_2 M}{\alpha_1} I(r_i, z_i, t) + \frac{\alpha_3 M}{\alpha_1} I^2(r_i, z_i, t)}$$

(5.13)

Therefore, the solution of the above equation (5.1 A) can be expressed for the incoming beam at every interface except the first incident point as

$$I_{il}(r_i, L_i, t) = \frac{1}{3a_i(r_i, z_i, t)} \left( Q_i(r_i, z_i, t) + \frac{\Delta_{oi}(r_i, z_i, t)}{Q_i(r_i, z_i, t)} - b_i(r_i, z_i, t) \right)$$

(5.14)

The other two roots of the cubic equation are ignored in this study as it is not applicable for our case. Here,  $Q_i(r_i, z_i, t)$  and  $\Delta_{oi}(r_i, z_i, t)$  in the above eq. (5.5 A) can be expressed as below

$$Q_i(r_i, z_i, t) = \sqrt[3]{\frac{\sqrt{\Delta_{1i}^2(r_i, z_i, t) - 4\Delta_{oi}^3(r_i, z_i, t)} - \Delta_{1i}(r_i, z_i, t)}{2}}$$

$$\Delta_{oi}(r_i, z_i, t) = b_i^2(r_i, z_i, t) - 3a_i(r_i, z_i, t)c_i(r_i, z_i, t)$$

$$\Delta_{1i}(r_i, z_i, t) = 2b_i^2(r_i, z_i, t) - 9a_i(r_i, z_i, t) + 27a_i^2(r_i, z_i, t)d_i(r_i, z_i, t)$$

(5.15)

The total transmitted intensity at the exit side of the sample is given by

$$I_T(r, z, t) = \sum_{m=0}^{\infty} I_{(2m+1)T}(r_{(2m+1)}, L_{(2m+1)}, t)$$

(5. 16)

The total reflected light intensity at the exit side of the sample is given by

$$I_R(r, z, t) = I_{OR}(r, 0, t) + \sum_{m=1}^{\infty} I_{(2m)T}(r_{(2m)}, L_{(2m)}, t)$$

(5. 17)

Here, the transmitted intensity at each of the points are  $I_{iT}(r_i, L_i, t)$  are related to  $I_{iI}(r_i, L_i, t)$  as

$$I_{iT}(r_i, L_i, t) = T_{ie}(I_{iI})I_{iI}(r_i, L_i, t)$$

$$I_{0T}(r, 0, t) = T_{0I}(I_{0I})I_{0I}(r, 0, t)$$

(5. 18)

Here,  $T_{0I}(I_{0I})$  and  $T_{ie}(I_{iI})$  are the transmission coefficients at the first incoming point and all others that can be expressed as

$$T_{0I}(I_{0I}) = \frac{4(n_1 + n_2 I_{0I} + n_3 I_{0I}^2)}{((n_1 + n_2 I_{0I} + n_3 I_{0I}^2)^2 + 1)^2 + \kappa^2}$$

$$T_{ie}(I_{iI}) = \frac{4(n_1 + n_2 I_{iI} + n_3 I_{iI}^2)}{((n_1 + n_2 I_{iI} + n_3 I_{iI}^2)^2 + 1)^2 + \kappa^2}$$

$$\kappa = \frac{\lambda(\alpha_1 + \alpha_2 I_{iI} + \alpha_3 I_{iI}^2)}{4\pi}$$

(5. 19)

Where,  $n_1$ ,  $n_2$ , and  $n_3$  are the real part of the linear, nonlinear third-order and nonlinear fifth-order refractive index, respectively, and  $\kappa$  is the imaginary part of the nonlinear refractive index.

Here, the reflected light at each of the points are  $I_{iR}(r_i, L_i, t)$  are related to  $I_{iI}(r_i, L_i, t)$  as

$$I_{iR}(r_i, L_i, t) = R_{ie}(I_{iI})I_{iI}(r_i, L_i, t)$$

$$I_{0R}(r, 0, t) = R_{oI}(I_{oI})I_{oI}(r, 0, t)$$

(5. 20)

Here,  $R_{oI}(I_{oI})$  and  $R_{ie}(I_{iI})$  are the transmission coefficient at the first incoming point and all others that can be expressed as

$$R_{oI}(I_{oI}) = \frac{((n_1 + n_2 I_{oI} + n_3 I_{oI}^2)^2 - 1)^2 + \kappa^2}{((n_1 + n_2 I_{oI} + n_3 I_{oI}^2)^2 + 1)^2 + \kappa^2}$$

$$R_{ie}(I_{ie}) = \frac{((n_1 + n_2 I_{iI} + n_3 I_{iI}^2)^2 - 1)^2 + \kappa^2}{((n_1 + n_2 I_{iI} + n_3 I_{iI}^2)^2 + 1)^2 + \kappa^2}$$

(5. 21)

## **CHAPTER 6: PULSE-TO-PULSE EVALUATION OF OPTICAL PROPERTIES IN ULTRAFAST LASER PROCESSING OF POLYPROPYLENE**

### 6.2 Introduction

Recent advances in ultrafast laser technology facilitate researchers to focus on understanding the physical process of ultrashort pulse interaction with materials and its applications for high-precision material processing in scientific and industrial applications [1-3]. Ultrafast lasers have been used in various types of material processing including laser cutting [4], drilling [5], polishing [6], cleaning [7], and micro/nano machining [8]. Ultrafast lasers produce minimal thermal damage to the material, which makes these lasers attractive for processing polymeric materials, which typically have a low melting temperature [9]. The interest of the ultrafast laser micro-processing of polymeric materials remains strong due to the high demand for using these materials in scientific and industrial applications [10-14]. However, material processing with ultrafast laser is quite complicated due to the dynamic behavior of laser-matter interaction, and there are pulse-to-pulse variations of the interaction mechanism. Therefore, ultrafast laser micro-processing of polymeric materials with high precision and control is still challenging [15, 16].

Laser processing with multiple ultrafast laser pulses has been already discussed in various articles [17-20]. Baset et al. [20] observed the morphological evolution and dynamics of femtosecond laser ablation of bulk polymethylmethacrylate (PMMA) irradiated with a pair of pulses with experimental and numerical studies. Hu et al. [21] showed that a second delayed pulse causes an increase in the ion emission from Si and enhanced absorption of the second pulse was suggested as the reason for increased ion emission. Researchers also found that the material

response and the ablation process have a significant dependence on the delay between the pulses [22]. Most of the studies were performed with metals and dielectrics by using the pump-probe technique. For polymers, the understanding of fundamental mechanisms involved is still lacking, especially in the near-infrared (NIR) wavelength. In addition, determining pulse-to-pulse interaction mechanisms, especially optical properties such as reflectance, transmittance, and absorption, is crucial for selecting laser-processing parameters to maximize energy efficiency for industrial applications.

In this study, the pulse-to-pulse evolution of optical properties, such as reflectance, transmittance, and absorptance, is determined by performing time-resolved measurements in ultrafast laser interaction with polypropylene. The time-resolved measurement is performed by using an ellipsoidal mirror-based system, which can collect both specular and diffusive reflection from the irradiated sample. The measurements are carried out for each of the pulses in a double-pulse configuration for a wide range of fluence and the measurement of optical properties is compared with observed damage morphology. The absorption is explained with a model that includes both linear and nonlinear mechanisms.

## 6.2 Experimental setup

The experimental setup is shown in Fig. 6. 1. A Yb: KGW (Yb-doped potassium gadolinium tungstate) femtosecond laser from Light Conversion at a central wavelength of 1030 nm is used as the laser source. It delivers 170 fs to 10 ps ultrashort pulses with the maximum pulse energy of 1 mJ and repetition rate tunable from a single pulse to 1 MHz. The output beam with a diameter of 4 mm is expanded by a beam expander to 10 mm in diameter and the laser power is controlled with a variable neutral density (ND) filter. The laser beam is split into two arms, one as

the reference arm, which has 6.5% of the incident light and is used to determine the incident laser pulse energy, and the other as the source arm, which is focused onto the sample with a lens with 250 mm focal length. The diameter of the spot size is measured to be  $36.8 \mu\text{m}$  at the  $1/e^2$ -point.

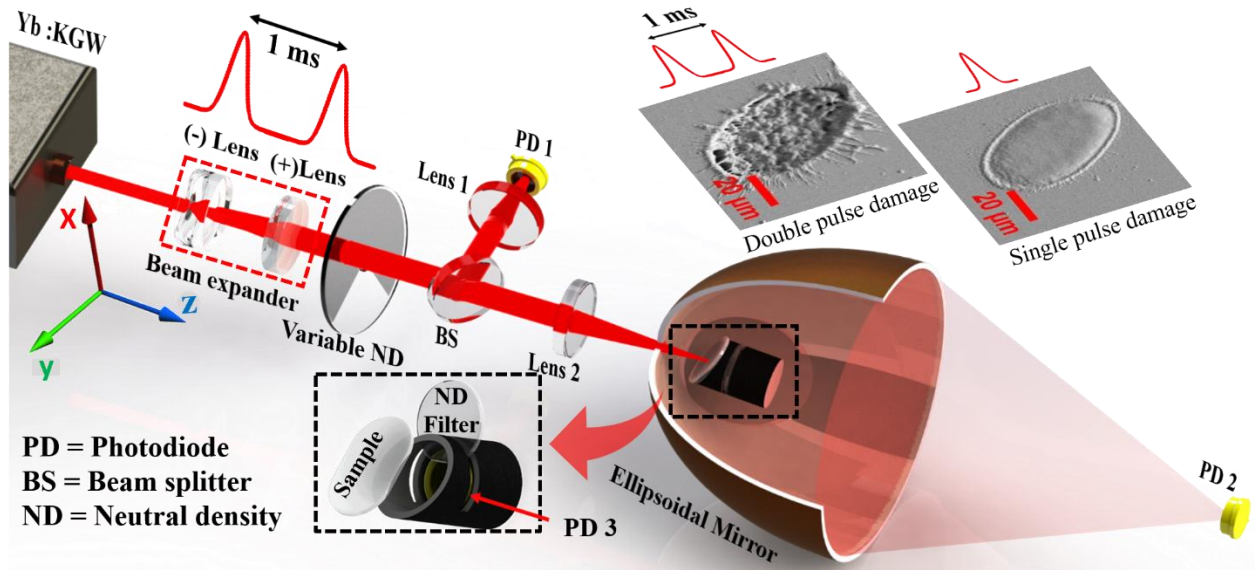


Figure 6.1: Experimental set up for measuring the optical properties of ultrafast laser interaction with transparent PP

A 1-GHz oscilloscope (Tektronics, MD03104), which is not shown in Fig. 6.1, and three photodiodes (PD 1-3, Thorlabs, FDS100) are used for data acquisition. Commercially available transparent PP sheets (PP301440, Goodfellow) of thickness  $450 \mu\text{m}$  are used in this experiment as samples, which are placed on the top of a fixture (Fig. 6.1 inset) and are close to the 1<sup>st</sup> focus of an ellipsoidal mirror. An ND filter with a diameter of 12.5 mm and PD 3 is placed in the fixture. To capture the reflected light (both specular and diffusive reflection) from the sample[23,24], an ellipsoidal mirror (E180, Optiforms) is used, and the reflected light is detected by PD 2 at the 2<sup>nd</sup> focus of the ellipsoidal mirror. The procedure to place PD 2 at the second focus of the ellipsoidal mirror has been discussed elsewhere [25]. To ensure a fresh surface for each laser shot, a 3D stage



is used to move the sample for irradiating with different pulse energies. The sample is irradiated with a total of two pulses and time-resolved optical properties, such as reflectance and transmittance, are measured experimentally. PD 2 is used to measure the reflectance light and PD 3 is used for the transmittance light. Fig. 6.1 also shows the damage profile for single pulse damage at the upper left and double-pulse damage in the upper right. As well be discussed next, a single pulse creates swelling and the double pulses create a crater.

### 6.3 Effect of 1<sup>st</sup> pulse and 2<sup>nd</sup> pulse during ultrafast interaction

To understand the pulse to pulse evolution of optical properties such as reflectance, transmittance, and absorptance of polymeric material, i.e. PP, the time-resolved measurements are performed for a wide range of peak fluences, which covers below the threshold and above threshold fluence. The sample is irradiated with a pair of identical pulses, where each of the pulse duration is 170 fs and the delay between two pulses is 1 ms. Both pulses are focused at the same spot of the sample and the surface of the normal of the sample is tilted with an incident angle  $17^\circ$  to reduce the backscattering through the entrance hole of the ellipsoidal mirror.

Fig. 6. 2 shows the damage on the surface of the transparent PP sample and corresponding damage profiles for both a single pulse and a pair of pulses. The left side of Fig. 6. 2 shows damages, which are irradiated with a single pulse, where damages A, B, C, and D are irradiated with the pulse energies of 20, 30, 50 and 100  $\mu\text{J}$ , respectively, that correspond to the peak fluences of 3.76, 5.64, 9.4, and 18.8  $\text{J}/\text{cm}^2$ , respectively. The 2D profilometer (Dektak, Bruker) measurements are performed to confirm the damage profiles, which are shown next to the SEM (scanning electronic microscopy) image of damage profile. It is obvious from both SEM image and profilometer measurements that single-pulse irradiation with fluence 3.76, 5.64, 9.4, and 18.8

$\text{J}/\text{cm}^2$  creates dome-like swelling on the surface of the transparent PP sample. The maximum height of the dome is around  $1.75 \mu\text{m}$  from the profilometer measurements.

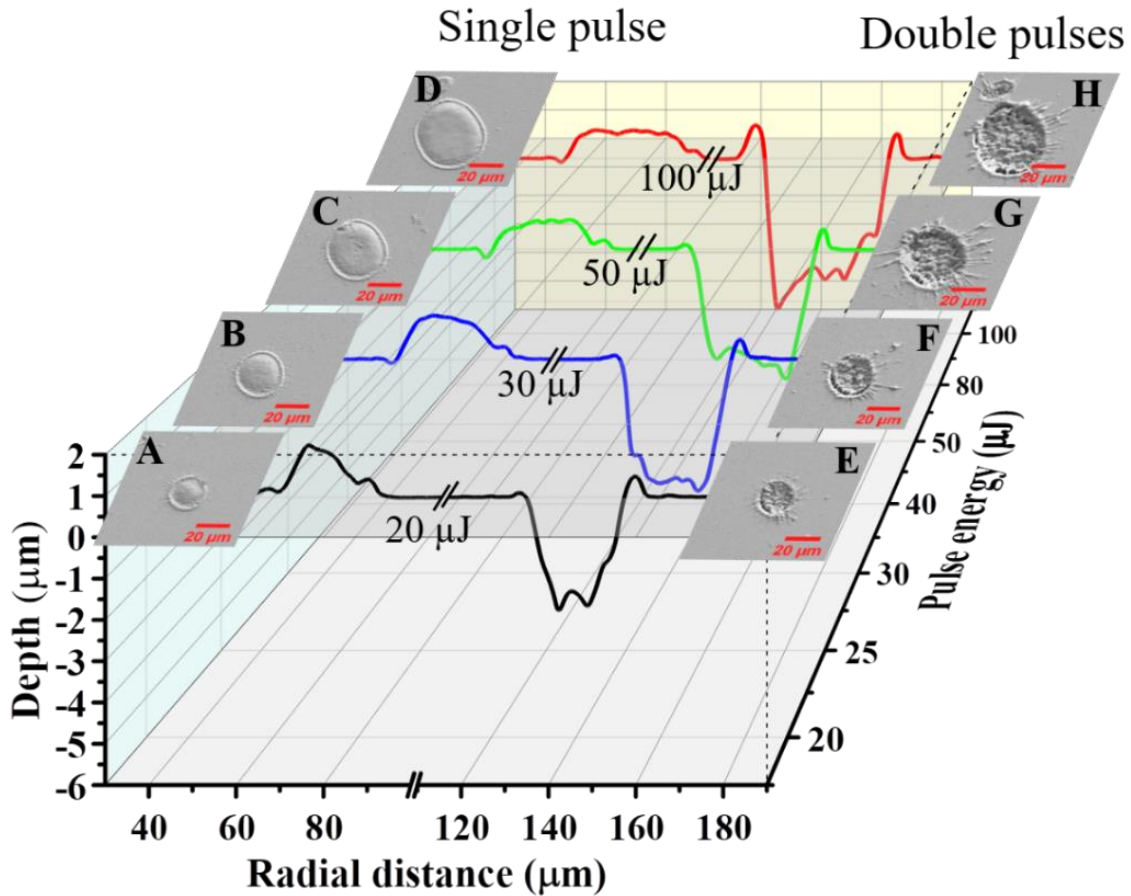


Figure 6.2: Damage A, B, C, and D (scanning electronic microscopy (SEM) images at the left) are irradiated with single pulse and damages E, F, G, and H (SEM images at the left) are irradiated with a pair of the identical pulse. The damage profiles are shown beside each of the damages.

Similarly, the right-hand side of Fig. 6.2 shows the damage with the double-pulse irradiation at the surface of the sample, where damages marked as E, F, G, and H are irradiated with fluences  $3.76$ ,  $5.64$ ,  $9.4$ , and  $18.8 \text{ J}/\text{cm}^2$  for each of the pulses, which are the same fluences used for single pulse irradiation. The profilometer measurements are shown next to the damages.

For the double-pulse case, craters are observed at the surface of the sample and the maximum depth of the crater is found to be 5.7  $\mu\text{m}$ , which is significantly different morphology than single pulse irradiation. It is found in this study that single-pulse irradiation creates void below the surface of the sample, which is shown and confirmed in Fig. 6.3.

Fig. 6. 3 shows the evidence of void formation near to the surface of the transparent sample induced by the single pulse irradiation of femtosecond laser with pulse duration 170 fs. The cross-sectional analysis of the irradiated sample is performed with focused ion beam (FIB) milling, where the sample is irradiated with a pulse energy of 80  $\mu\text{J}$ . The inset (a) in Fig. 6. 3 shows the center part of the irradiated place, where the formation of the voids is denser than the side as the intensity of the laser is higher at the center. The diameter of the voids is found to be increasing with pulse energy and the diameter of the voids is found to be 0.2 to 3  $\mu\text{m}$  corresponding to the pulse energy 12.5  $\mu\text{J}$  to 100  $\mu\text{J}$ . The inset (b) in Fig. 6. 3 shows the distinction between irradiated place at the surface, where the void formation is found near to the surface, while on the surface which receives no direct laser irradiation, no void is observed. Instantaneous heating [26, 27] and expansion [28, 29] occur due to the ultrashort pulse irradiation on the surface of the polymeric material. Micro/nano splashes are observed at the surface of the sample due to the localized melting and explosive boiling and a two-phase liquid-gas mixture develops after thermalization of the laser pulse in the polymeric sample in the ps time scale. Then material ejection takes place in the ns time scale [29, 30] due to hydrodynamics expansion, which is the reason responsible for the formation of micro/nano voids as well as dome-shaped swelling [31].

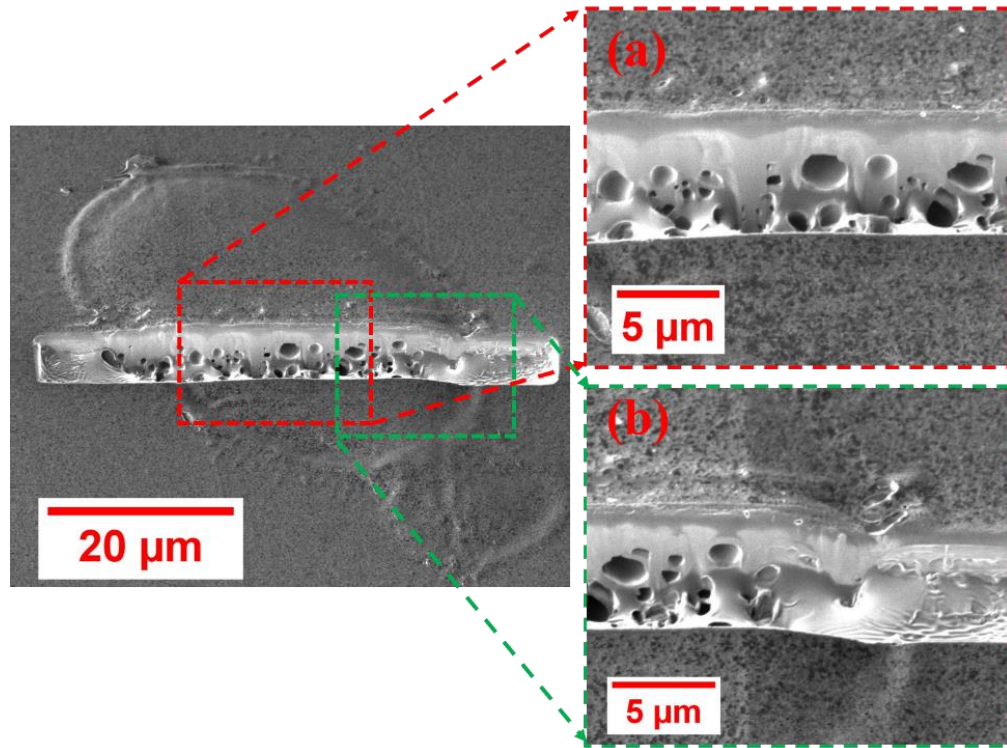


Figure 6.3: Cross-sectional analysis of transparent PP sample with Focused Ion Beam (FIB) milling, which is irradiated at pulse energy  $80 \mu\text{J}$

Fig. 6. 5 shows the total reflectance (specular and diffusive),  $R$ , transmittance,  $T$ , and absorptance,  $A$ , as a function of peak fluence for 1<sup>st</sup> pulse and 2<sup>nd</sup> pulse in multiple pulse cases with the delay 1 ms. To determine  $R$  and  $T$ , an integrated area at FWHM of the oscilloscope traces for PDs signal for reflection and transmission are used with proper scaling based on the ND attenuation and more discussion on determining  $R$ ,  $T$  and  $A$  can be found elsewhere [25]. In this study, it is observed that the threshold peak fluence for surface damage of the transparent PP sample is  $0.94 \text{ J/cm}^2$  with single pulse irradiation. The material surface doesn't undergo any surface modification  $< 0.94 \text{ J/cm}^2$ . Therefore, the reflectance and transmittance remain constant up to the peak fluence  $0.94 \text{ J/cm}^2$  for the first pulse in case of multi-pulse irradiation. Therefore, this constant peak fluence/intensity region is defined as a “linear absorption region” for single-

pulse absorption. Similarly, the absorptance remains constant for the peak fluence  $< 0.94 \text{ J/cm}^2$  as it is determined from the reflectance and transmittance,  $A = 1 - R - T$ . The transmittance and reflectance start to drop after the peak fluence reaches the threshold peak fluence due to the nonlinear absorption with high intensity, which will be discussed in the next section.

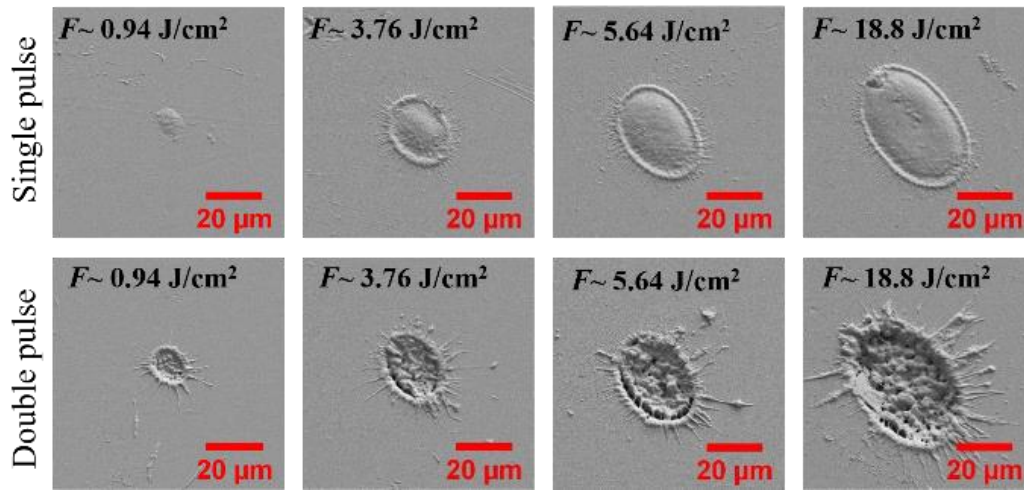


Figure 6.4: Surface damage with a single pulse (top) and double pulse (bottom) with different peak fluences

However, it can be seen from Fig. 6. 4 that 2<sup>nd</sup> irradiated pulse is not behaving exactly the same as 1<sup>st</sup> irradiated pulse due to modification formed on the surface and as well as inside the sample. The reflectance for 1<sup>st</sup> pulse and 2<sup>nd</sup> pulse look quite similar except at very high peak fluences, where the surface roughness has been changed, which can be seen from Fig. 6.4 and Fig. 6.2. As the sample in this study is a transparent material, which means most of the light is transmitted at low energy, the dominant factor that contributes to absorptance is transmittance.

It can be seen from Fig. 6.5 that the transmittance for 1<sup>st</sup> pulse and 2<sup>nd</sup> pulse is mostly distinct from each other. The formation of micro/nano voids with 1<sup>st</sup> pulse is suggested to be the reason for changed transmission inside the material for 2<sup>nd</sup> pulse. For low pulse energy, the size of

the voids is smaller inside the material, therefore transmitted light diffracted more inside the material, and transmission gets lower for 2<sup>nd</sup> pulse. However, the diameter of the voids increases with pulse energy, and more hollow regions are formed inside the material, which allows for transmitting more light for the higher fluence case of 2<sup>nd</sup> laser pulse.

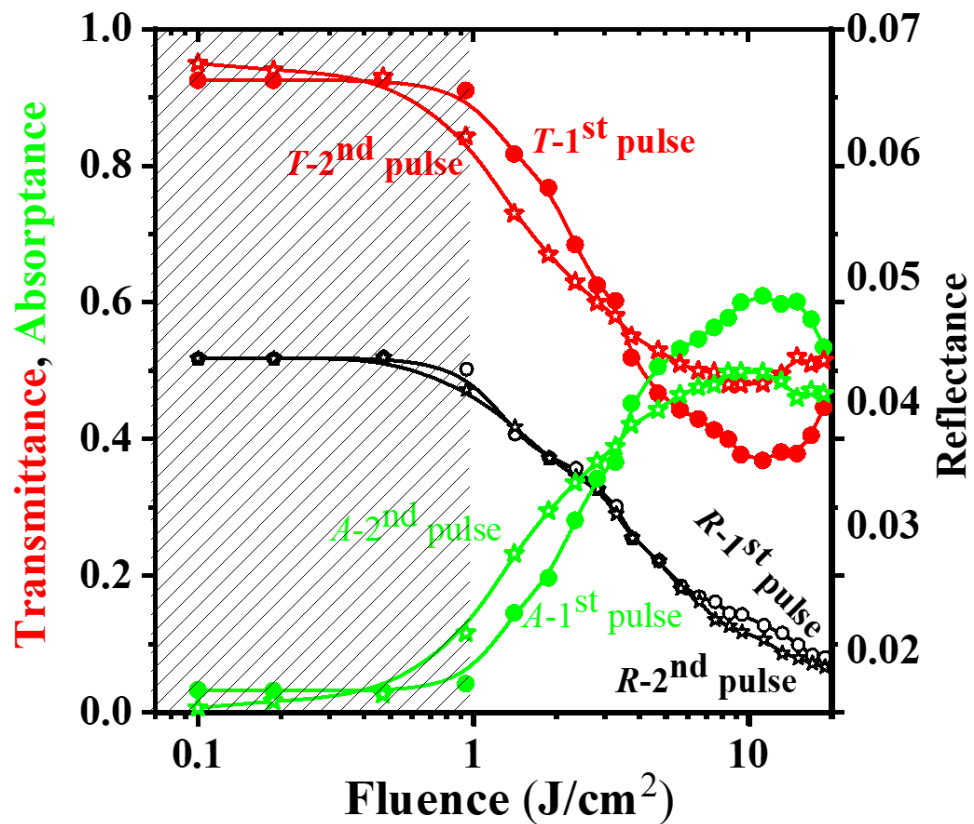


Figure 6.5: Reflectance (R), transmittance (T), and absorbance (A) as a function of peak fluence for 1<sup>st</sup> pulse (circular data point) and 2<sup>nd</sup> pulse (star data points) in double pulse case with the delay 1 ms.

#### 6.4 Theoretical Analysis

Ultrafast lasers have been used for various high precision polymer processing, but several fundamental questions, are still not clear. Therefore, it is required to understand those fundamental questions including the relative significance of different linear and nonlinear absorption regimes

and interaction mechanisms with different kinds of materials for high precision material processing. For polymeric materials, which have a wide bandgap, the absorption mechanism has the contribution of both linear (single-photon) and nonlinear (multi-photon) processes [25, 32]. However, the absorption mechanism for polymer processing with NIR wavelength due to vibrational overtone or combination absorption [33]. The equation that describes the attenuation of the spatial and radial intensity,  $I(r, z, t)$  of the ultrafast laser, which is passing through the material undergoing single-photon, two-photon or two-steps or three-photon or three-steps absorption is given by

$$\frac{dI(r, z, t)}{dz} = -\alpha_1 I(r, z, t) - \alpha_2 I^2(r, z, t) - \alpha_3 I^3(r, z, t) \quad (6.1)$$

where  $\alpha_1$ ,  $\alpha_2$  and  $\alpha_3$  are linear and nonlinear absorption coefficient for single-photon (linear), two-photon or two-steps (nonlinear) and three-photon or three-steps (nonlinear), respectively. Equation (6.1) enables to calculate nonlinear effects (e.g. the second and third-order) due to propagation of ultrafast pulse in dielectric and non-magnetic medium, and this approximation may no longer be valid in the case of higher-order nonlinear effects. Compared to the Maxwell equation, Equation (6.1) is easy and straightforward to apply to calculate intensity distribution inside the medium. The analytical solution of the above differential equation (6.1) can be express in compact form as below

$$I(r, z, t) = \frac{1}{3a} \left( Q + \frac{\Delta_o}{Q} - b \right) \quad (6.2)$$

The variables which are used in the above eq. (2) are defined in the previous chapter.

The transmittance,  $T$  of the ultrafast laser, which is passing through the PP sample can be expressed in terms of the above solution in eq. (6.1) as below

$$T = \frac{E_{out}}{E_{in}} = \frac{2\pi(1-R_e)}{E_{in}} \int_{r=0}^{\infty} \int_{-t_{on}}^{t_{on}} I(r, z, t) r dr dt \quad (6.3)$$

where  $R_e$  is the reflectance of the laser pulse at the exit of the sample.

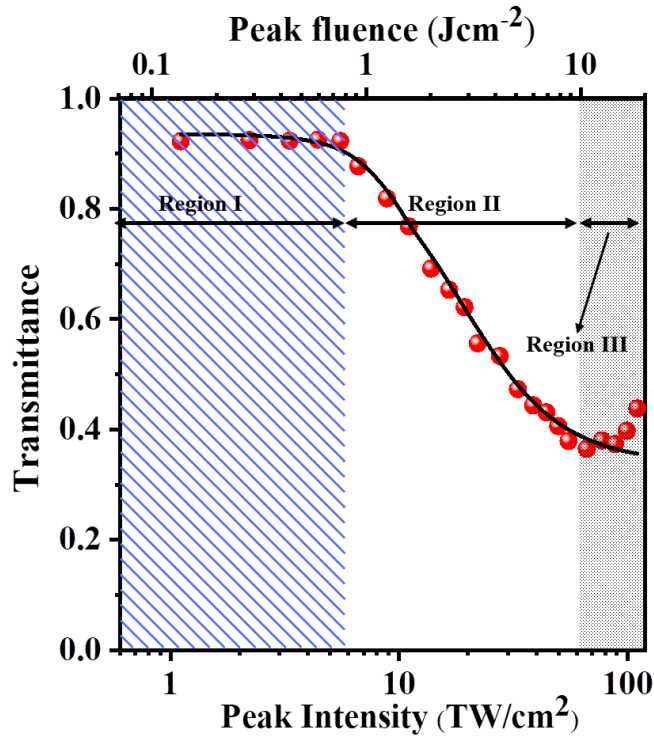


Figure 6.6: Fitting of the experimental results of 167 fs for transparent PP sample. The laser intensity used in this experiment can be divided into three regions (Region I, II, and III)

Fig. 6.6 shows the experimental results of transmittance fitted with theoretical calculation, where the transmittance is divided into three fluence/ intensity regions. Region I represents linear absorption region and Region II and III represent the nonlinear region as defined in the above



section. It can be seen that the transmittance remains constant until the fluence/intensity reaches to the damage threshold peak fluence/intensity, where the damage threshold peak fluence is found to be  $0.94 \text{ J/cm}^2$ . The transmittance starts to decrease after the damage threshold peak fluence as shown in Fig. 6.5, which indicates nonlinear absorption. The transmission keeps decreasing until the peak fluence reaches  $10 \text{ J/cm}^2$ . Note that the absorbance of the sample increases in Region II as the transmittance decreases.

In this study, the linear and nonlinear absorption coefficients are determined from the fitting results of the experimental data with the theoretical calculation of Eq. (6.3) for different pulse durations, i.e.  $167 \text{ fs}$ ,  $371 \text{ fs}$ , and  $1000 \text{ fs}$ , which is shown in fig. 6.6 (b). The average value of the linear (single-photon) absorption coefficient is found to be  $\alpha_1 = (110.85 \pm 3) \text{ m}^{-1}$ , which agrees with the experimental value determined from the linear spectroscopic measurement for the thickness of the transparent sample,  $L = 450 \text{ }\mu\text{m}$ . The linear refractive index of this transparent polypropylene sample is 1.49. Determination of the absorption coefficients and nonlinear refractive index will be discussed in more detail in the next chapter.

The average value of nonlinear absorption coefficient for two-photon or two-steps absorption and the three-photon or three steps are found to be  $\alpha_2 = (8.01 \pm 2.15) \times 10^{-13} \text{ mW}^{-1}$  and  $\alpha_3 = (3.21 \pm 1.0) \times 10^{-29} \text{ m}^3\text{W}^{-2}$ , respectively from the fitting result, those values are consistent with the previously reported value for the polymeric materials [34,35]. The average value of nonlinear refractive indexes are found to be  $n_2 = (3.22 \pm 1.15) \times 10^{-20} \text{ m}^2\text{W}^{-1}$  and  $n_3 = (2.64 \pm 1) \times 10^{-37} \text{ m}^4\text{W}^{-2}$ . This study suggests that the non-resonant vibrational overtone or combination absorption happened at  $1030 \text{ nm}$  and  $515 \text{ nm}$ , and resonant overtone or combination happened at  $353 \text{ nm}$ , which is shown in Fig. 6.7. The fundamental wavelength used in this study is  $1030 \text{ nm}$ , and

therefore, the third-harmonic of the fundamental wavelength could be around 343 nm. However, the absorption peak from linear spectroscopic measurement is found to be at 353 nm and 373 nm.

When a high-intensity laser pulse propagates through a nonlinear medium, an ultrashort pulse accumulates the temporal phase as it propagates, which is known as self-phase modulation (SPM), which is a nonlinear phenomenon due to nonlinear refractive index change inside the medium [36, 37] which is discussed in section 5.6. Therefore, the wavelength shift due to SPM phenomena can be written as below

$$\lambda(t) - \lambda_o = \lambda_o \left( \frac{n_2 \frac{dI(t)}{dt} + 2n_3 I(t) \frac{dI(t)}{dt}}{\frac{c}{z} - n_2 \frac{dI(t)}{dt} - 2n_3 I(t) \frac{dI(t)}{dt}} \right)$$

(4)

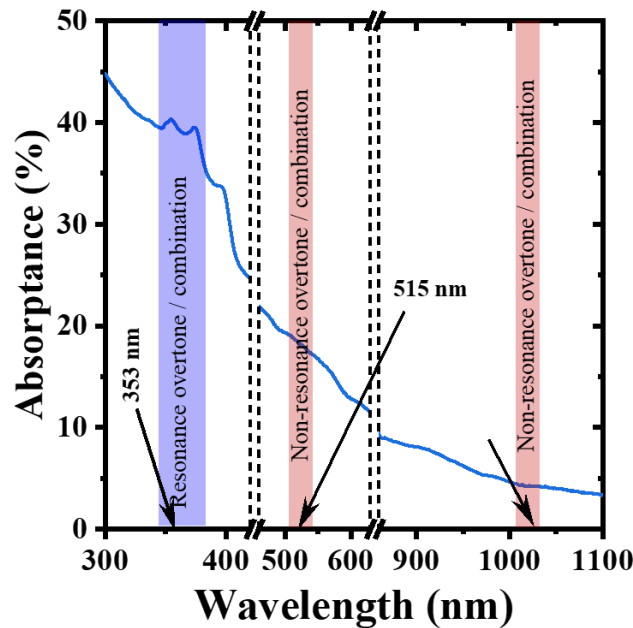


Figure 6.7: Absorptance, A, of transparent PP sample is determined from the linear spectroscopic measurement.

The maximum wavelength shifting corresponding to the maximum peak intensity  $106.1 \text{ TW/cm}^2$  is found to be around  $\pm 30 \text{ nm}$ , which covers both peaks at  $353 \text{ nm}$  and  $373 \text{ nm}$ . Therefore, three-steps or three-photon absorption are suggested to have happened through vibrational overtone absorption mechanism by shifting wavelength at a very high intensity of the laser beam.

## 6.5 Summery

In summary, the pulse-to-pulse evaluation of optical properties of polypropylene in ultrafast laser interaction is determined by performing time-resolved measurement for multiple pulse configuration for a wide range of intensity from below to well above the damage threshold. The measurements of the optical properties are showed a strong correlation with damage morphology. The experimental data is explained with a model that includes linear and nonlinear absorption mechanism and the absorption coefficient are determined. Our results could be useful to perform high precision polymer processing for scientific and industrial applications.

## 6.6 References

1. K. Sugioka and Y. Cheng, “Ultrafast lasers - reliable tools for advance materials processing,” *Light: Sci. Appl.* 3(4), e149 (2014).
2. W. Sibbett, A. A. Lagatsky, and C. T. A. Brown, “ The development and application of femtosecond laser systems, *Optics Express* 20(7), 6989-7001 (2012).
3. K. C. Phillips, H. H. Gandhi, E. Mazur, and S. K. Sundaram, “Ultrafast laser processing of materials: a review,” *Adv. Opt. Photonics* 7(4), 684–712 (2015).
4. A. N. Fuchs, M. Schoeberl, J. Tremmer, and M. F. Zaeh, “ Laser cutting of carbon fiber fabrics, *Phys. Procedia* 41, 372-380 (2013).
5. X. Zhao, and Y. C. Shin, Femtosecond laser drilling of high - aspect ratio microchannels in glass, *Appl. Phys. A* 104(2), 713–719 (2011).
6. L. L. Taylor, J. Xu, M. Pomerantz, T. R. Smith, J. C. Lambropoulos, and J. Qiao, “Femtosecond laser polishing germanium,” *Opt. Express* 9, 4165–4177(2019).
7. T. Ersoy, T. Tunay, M. Uğuryol, G. Mavili, and S. Akturk, Femtosecond laser cleaning of historical paper with sizing, *J. Cult. Herit.* 15, 258–265 (2014).
8. R. R. Gattass, and E. Mazur, Femtosecond laser micromachining in transparent materials,” *Nat. Photonics* 2, 219–225 (2008).
9. Godovsky, Y. K., (1992) *Thermophysical properties of Polymers*, (Springer).
10. A. Shibata, S. Yada, and M. Terakawa, “Biodegradability of poly (lactic-co-glycolic acid) after femtosecond laser,” *Sci. Rep.* 6, 27884 (2016).
11. M. Terakawa, “Femtosecond laser processing of biodegradable polymers, ”*Appl. Sci.* 8, 1123 (2018).
12. A. Rahaman, A. Kar, and X. Yu, “Thermal effects of ultrafast laser interaction with polypropylene,” *Opt. Express* 27(4), 5764-5783 (2019).
13. A. Rahaman, X. Du, B. Zhou, H. Cheng, A. Kar, and X. Yu., “Absorption and temperature distribution during ultrafast laser micro-cutting of polymeric materials”, *J Laser Appl.* 32, 022044 (2020).
14. B. Zhou, A. Rahaman, X. Du, H. Cheng, A. Kar, and X. Yu, “Laser processing of dielectrics using spatiotemporally tuned ultrashort pulses”, *J Laser Appl.* 32, 022041(2020).
15. K. Sugioka, “Progress in ultrafast laser processing and future prospects”, *Nanophotonics* 6(2), 393 – 413 (2017).
16. M. V. Shugaev, C. Wu, O. Armbruster, A. Naghilou, N. Brouwer, D. S. Ivanov, T. J. Y. Derrien, N. M. Bulgakova, W. Kautek, B. Rethfeld and L. V. Zhigilei, “Fundamentals of ultrafast laser-interaction”, *MRS Bull.* 41, 960 – 968(2016).

17. T., Donnelly, J. G., Lunney, S, Amoruso, R, Bruzzese, X, Wang, and X, Ni,) “Double pulse ultrafast laser ablation on nickel in a vacuum”, *Jour. Appl. Phys.* 106, 013304 (2009).
18. S., Amoruso, R., Bruzzese, and X., Wang, (2009) “Plume composition control in double pulse ultrafast laser ablation of metals,” *Appl. Phys. Lett.* 95, 251501(2009).
19. M. Li, S. Menon, J. P. Nibarger, and G. N. Gibson, “Ultrafast electron dynamics in femtosecond optical breakdown of dielectrics”, *Phys. Rev. Lett.* 82, 2394-2397(1999).
20. F. Baset, K. Popov, A. Villafranca, A. M. Alshehri, J. M. Guay, L. Ramunno, and V. R. Bhardwaj, “Nanopillar formation from two-shot femtosecond laser ablation of poly-methyl methacrylate,” *Appl. Sur. Sci.* 357, 273-281(2015).
21. Z. Hu, “Mechanism for the ablation of Si<111> with pairs of ultrashort laser pulses,” *Appl. Phys. Lett.* 90, 131910(2007).
22. M. E., Povarnitsyn, T. E., Itina, K.V., Khishchenko, and P. R., Levashov, Suppression of ablation in femtosecond double-pulse experiments, *Phys. Rev. Lett.* 103, 195002(2009).
23. A. Y. Vorobyev and C. Guo, (2011) Reflection of femtosecond laser light in multipulse ablation of metals, *J. Appl. Phys.* **110**, 043102 (2011).
24. O. Benavides, O. Lebedeva, and V. Golikov, (2011) Reflection of nanosecond Nd: YAG laser pulses in ablation of metals, *Opt. Express* **19**(22), 21842.
25. A. Rahaman, A. Kar, and X. Yu, “Time-resolved measurements of optical properties in ultrafast laser interaction with polypropylene”, *Opt. Express*, 28(2), 2640-2648(2020).
26. F. Baset, A. Villafranca, J. M. Guay, and R. Bhardwaj, “Femtosecond laser induced porosity in poly-methyl methacrylate,” *Appl. Sur. Sci.*, **282**, 729-734(2013).
27. V. V. Zhakhovskil, K. Nishihara, S. I., Anisimov, and N. A. Inogamov, “Molecular – dynamics simulation of rarefaction waves in media that can undergo phase transition,” *JETP Let.*, **71**(4), 167-172 (2000).
28. F. Baset, K. Popov, A. Villafranca, J. M. Guay, Z. A-Rekabi, A. E. Pelling, L. Ramunno, and R. Bhardwaj, “Femtosecond laser induced surface swelling in poly-methyl methacrylate,” *Opt. Express* **21**(10), 12527 (2013).
29. S. Lai, M. Ehrhardt, P. Lorenz, D. Hirsch, J. Zajadacz, J. Lu, B., Han, and K. Zimmer, “Submicron bubbles/voids formation in the subsurface region of soda-lime glass by single pulse fs laser-induced spallation,” *Appl. Sur. Sci.* **502**, 144134 (2019).

30. S. I. Anisimov, N. A. Inogamov, A. M. Oparin, B. Rethfeld, T. Yabe, M. Ogawa, and V. E. Fortov, "Pulsed laser evaporation: Equation-of-state effects", *Appl. Phys. A* **69**, 617-620(1999).
31. E. G. Gamaly, S. Juodkazis, H. Misawa, B. L. Davies, A. V. Rode, L. Hallo, P. Nicolai, and V. T. Tikhonchuk, "Formation of nano-voids in transparent dielectrics by femtosecond lasers," *Appl. Phys.* **8**, 412-415(2008).
32. T. Viertel, L. Pabst, M. Olbrich, R. Ebert, A. Horn, and H. Exner, "Generation of nano-voids inside polylactide using femtosecond laser irradiation" *Appl. Phys. A* **123**, 789 (2017).
33. M. Asobe, I. Yokohama, T. Kaino, S. Tomaru, and T. Kurihara, "Nonlinear absorption and refraction in an organic dye functionalized main chain polymer waveguide in the 1.5  $\mu\text{m}$  wavelength region" *Appl. Phys. Lett.* **67**, 891 (1995).
34. T. Chang, X. Zhang, X. Zhang, and H. L. Cui, "Accurate determination of dielectric permittivity of polymer from 75 GHz to 1.6 THz using both S- parameters and transmission spectroscopy," *Appl. Opt.* **56**, 3287 (2017).
35. C. Schnebelin, C. Cassagne, C. B. D. Araujo, and G. Boudebs, "Measurements of the third- and fifth-order optical nonlinearities of water at 532 and 1064 nm using the  $D4\sigma$  method" *Opt. Lett.* **39**, 5046 (2014).
36. M. Gu, A. Satija, and R. P. Lucht., "Effects of self-phase modulation (SPM) on femtosecond coherent anti-stoke Raman scattering spectroscopy" *Opt. Express* **27**, 33954-33966(2019).
37. I.W. Hsieh, X. Chen, J. I. Dadap, N. C. Panoiu, and R. M. Osgood, Jr., "Ultrafast-pulse self-phase modulation dispersion in Si photonic wire-waveguides" *Opt. Express* **14**, 12380-12387 (2006).

## **CHAPTER 7: EFFECT OF PULSE DURATION IN FRONT AND BACK SURFACE PROCESSING OF TRANSPARENT POLYPROPYLENE**

### 7.1 Introduction

In the last few years, ultrafast laser technologies have proved to be of great interest from material processing applications [1-3]. The interest of the ultrafast laser micro-processing of polymers has been grown significantly over the past few years due to the high demand for using polymers in scientific and industrial applications [4-8]. However, material processing with ultrafast laser is quite complicated due to the dynamic behavior of the interaction between the ultrashort pulse and polymeric material. Therefore, the ultrafast laser micro-processing of polymers with high precision and control is still challenging for the researcher [9,10].

A promising approach that can control laser-material interaction for high precision material processing is the temporal pulse shaping of the ultrashort pulses [11]. Researchers have already shown that the temporal pulse shaping enables enhanced optical properties, i. e. absorptance, of the materials [12, 13]. These various studies have provided some understanding on dynamics of laser-matter interactions, but most of the studies deal with ultrafast laser ablation of dielectrics especially pure silica, while ultrafast pulse shaping for polymer processing has investigated less even though polymers are one the first materials to be processed by ultrafast lasers. However, the nature of absorption for near-infrared laser beams is not fully understood, and therefore, it remains challenging to process polymers with high energy-efficiency.

In this chapter, the effect of the pulse duration is investigated during the ultrafast laser interaction with a transparent PP sample in a single-shot configuration. An analytical solution of the differential equation of ultrafast laser pulse propagation is applied considering the spatial and

temporal distribution of intensity to observe intensity distribution inside the sample. The enhancement of absorptance is investigated for different pulse durations by performing the time-resolved measurement of optical properties of the ultrafast laser-material interaction with polymer (i.e. polypropylene). Besides, the spatial and temporal distortion of ultrashort pulse propagation through the medium is investigated.

## 7. 2 The spatial and temporal distortion of ultrashort pulse

The equation, which describes the attenuation of the ultrafast laser pulse with spatial and radial intensity,  $I(r, z, t)$  passing through the material undergoing single-photon, two-photon or two – steps or three-photon or three-steps absorption is given by

$$\frac{dI(r_i, z_i, t)}{dz_i} = -\alpha_1 I(r_i, z_i, t) - \alpha_2 I^2(r_i, z_i, t) - \alpha_3 I^3(r_i, z_i, t) \quad (7.1)$$

where  $\alpha_1$ ,  $\alpha_2$  and  $\alpha_3$  are the linear, two-photon, or two-steps nonlinear and three-photon or three-steps nonlinear absorption coefficient, respectively.

The analytical solution of the above differential equation, which is developed in chapter 5, after passing through the material can be expressed as

$$I_{il}(r_i, z_i, t) = \frac{1}{3a_i(r_i, z_i, t)} \left( Q_i(r_i, z_i, t) + \frac{\Delta_{oi}(r_i, z_i, t)}{Q_i(r_i, z_i, t)} - b_i(r_i, z_i, t) \right) \quad (7.2)$$

where  $I_{il}(r_i, L_i, t)$  is the incident intensity at the different interfaces except for the first incident point. All the variables in the above equation are defined in the appendix in chapter 5.



The study of the propagation of an optical Gaussian pulse is important to control the process with an ultrafast laser. When a high-intensity ultrafast laser pulse propagates through an optical medium, the Gaussian pulse intensity is distorted temporally and spatially during the propagation due to the non-linear phenomena. To investigate the distortion of the Gaussian pulse, equation (7.2) is used and the intensity distribution is shown in Fig. 7.2.

Fig. 7.1 (a) shows the spatial distribution of the peak intensity of the ultrashort pulse during propagation through the transparent PP sample. It can be seen that the peak intensity of the Gaussian pulse reduces by 70% within 50  $\mu\text{m}$  distance inside the transparent sample and the shape of the Gaussian pulse changes to a different pulse shape, which is close to the flat top at near the back (exit) surface of the sample, where sample thickness is around 450  $\mu\text{m}$ .

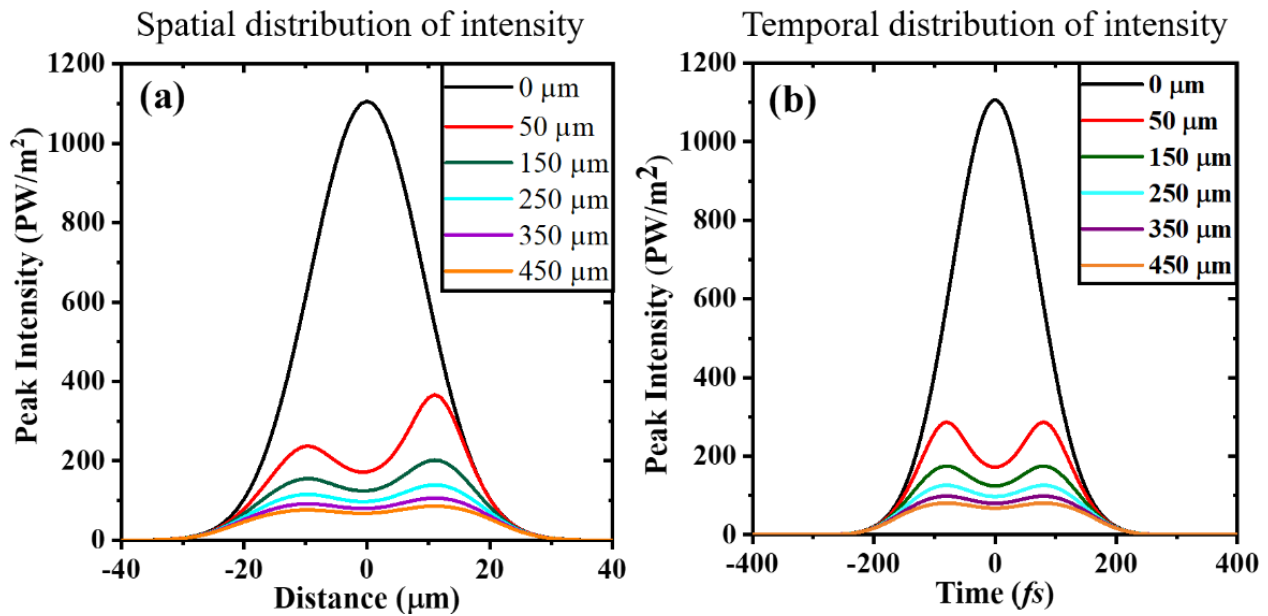


Figure 7.1: (a) spatial distribution, and (b) temporal distribution of the peak intensity of the ultrafast laser with pulse duration 167 fs.

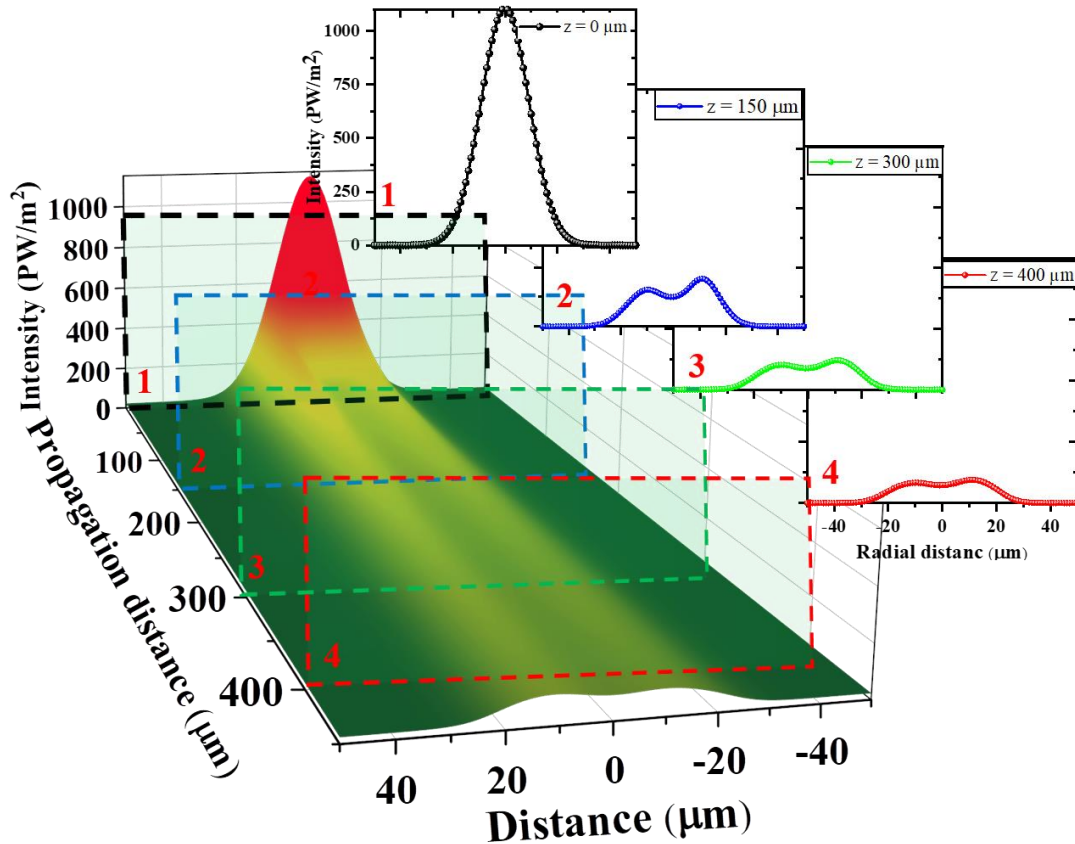


Figure 7.2: 3D representation of the peak intensity distribution of ultrafast laser during propagation through the transparent PP Sample.

The distribution of the peak intensity has two peaks at the different axial distance of the sample and the difference of the height of the peaks decreases as the pulse propagates through the medium because high-intensity pulse gets more distorted as it propagates through the medium than low intensity. It can be seen that peaks are not the same in the spatial distribution case, which could be due to the incident angle of the laser beam at the sample and two peaks could be due to the nonlinear refractive index change during high-intensity propagation. Fig. 7.2 (b) shows the distribution of the peak intensity at a different axial distance inside the medium with a pulse duration of 167 fs, where the distribution of the peaks also has similar behavior of the spatial case.

Fig. 7. 3, shows the 3D representation of the distribution of the spatial intensity distribution shown in 7.1 (a).

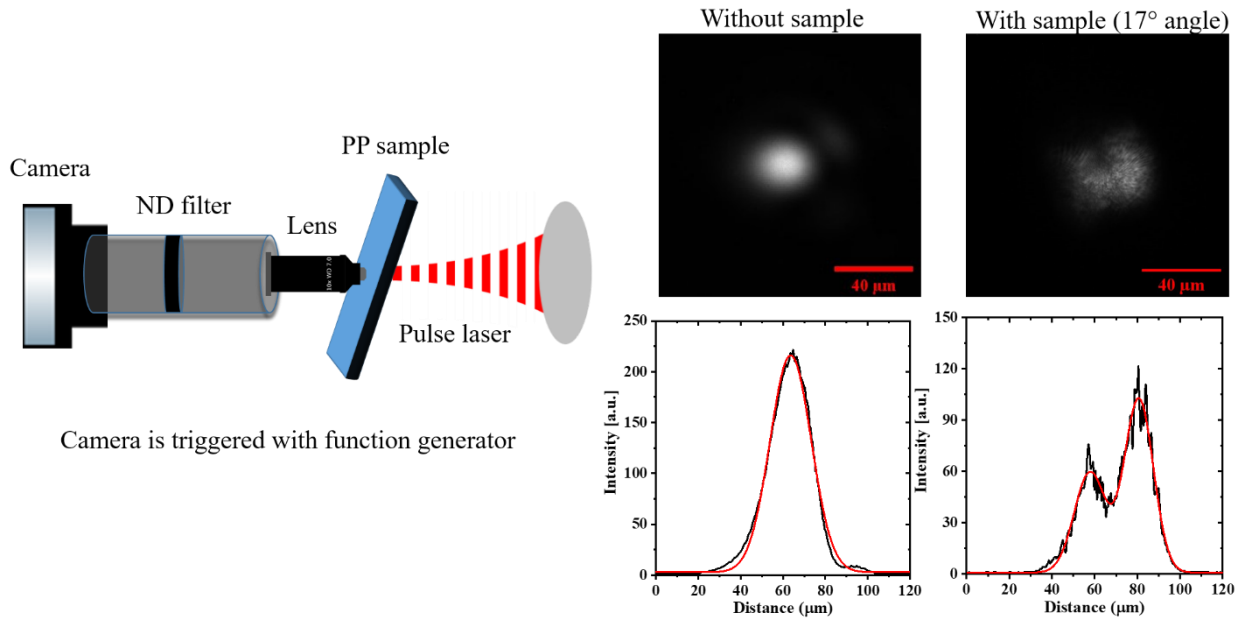


Figure 7.3: Experimental verification for double peaks with different heights , experimental setup in the left and camera images shown in right with and without sample

To verify the distinction in the peak heights for 167 fs case, a simple experimental design is developed by using a camera, objective lens, and a function generator. The function generator is used to trigger the camera to capture a single pulse irradiation. Here, the reference beam is shown to be nearly Gaussian, where the beam profile shows two peaks at the back surface of the sample as shown in Fig. 7.3.

### 7.3 The effect of pulse duration on ultrafast laser interaction

To investigate the effect of the pulse during on ultrafast laser interaction with PP sample, the experiments are performed with single pulse configuration for a wide range of pulse energies (1 μJ to 100 μJ) and the different pulse durations, i.e. 167 fs, 371 fs, 710 fs, and 1000 fs.

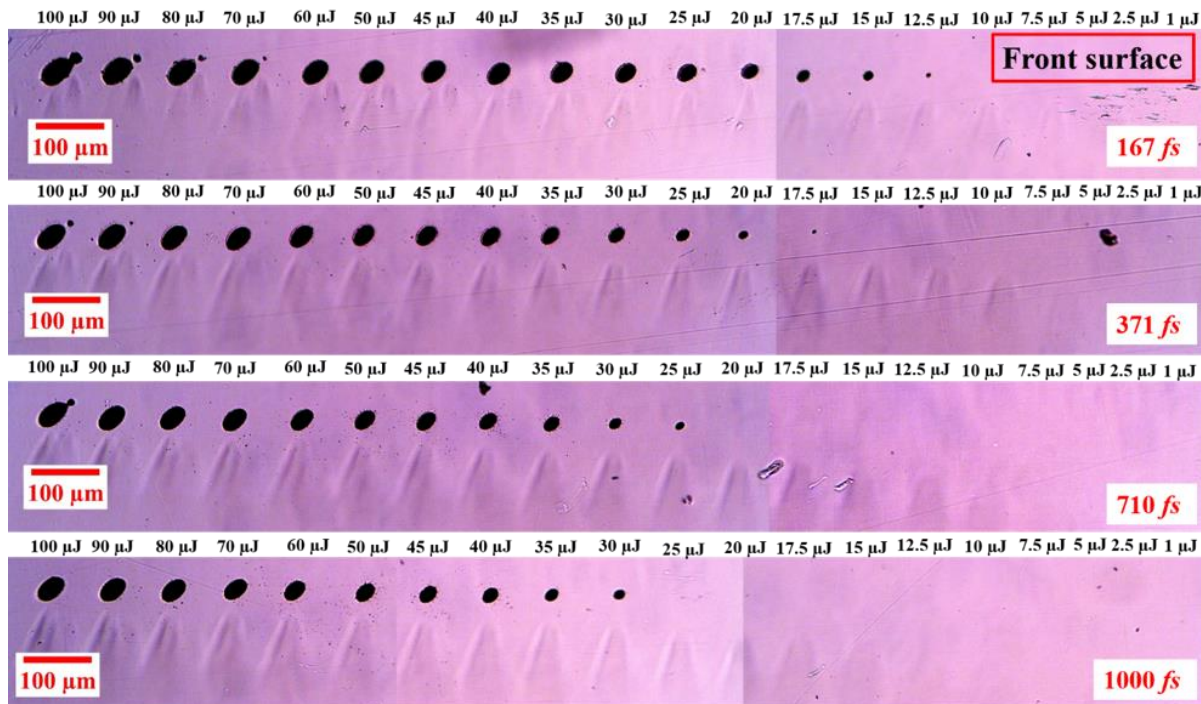


Figure 7.4 : The front surface damages the transparent PP sample with different pulse durations (i.e. 167, 371, 710, and 1000 fs) for a wide range of pulse energies (1  $\mu\text{J}$  to 100  $\mu\text{J}$ ).

Fig. 7.4 shows the front surface damages with the different pulse energies (1  $\mu\text{J}$  to 100  $\mu\text{J}$ ) and pulse durations (i.e. 167, 371, 710, and 1000 fs) and the front surface damage is dominant for 167 fs case since most of the energy absorbed at the surface of the sample due to high peak intensity, which has a higher nonlinear effect. Fig. 7.5 shows the back surface damage with the different pulse energies and pulse durations. Here, the back surface (or exit surface) damage is dominant in case of longer pulse duration (i.e. 1000 fs for this study) and there are no back surface damages for 167 fs pulse duration as mentioned above that most of the energy absorbed at the front surface for shorter pulse case (i.e. 167 fs).

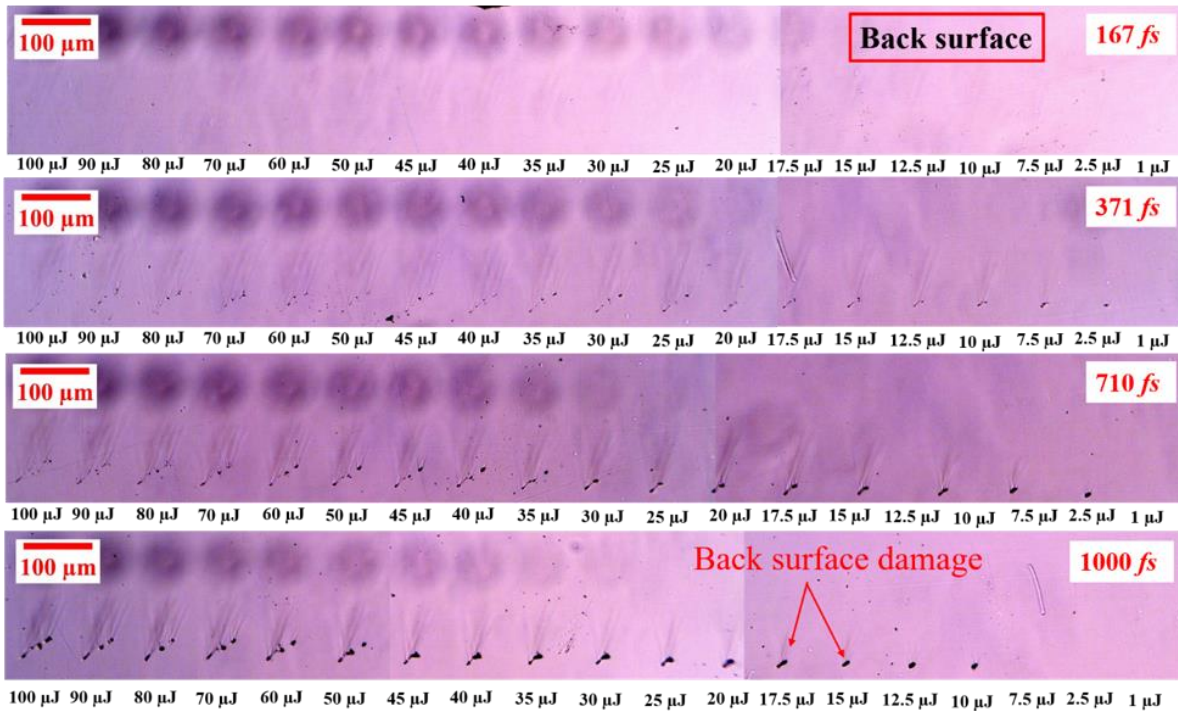


Figure 7.5: The back surface damages of the transparent PP sample with different pulse durations (i.e. 167, 371, 710, and 1000 fs) for a wide range of pulse energies (1  $\mu\text{J}$  to 100  $\mu\text{J}$ ).

Fig. 7.6 (a) shows the determination of damage area created by a single pulsed laser shot from the optical microscopic image of damages and Fig. 7.6 (b) shows the semilog graph of damage area as a function of peak intensities. This graph is used to determine the peak threshold damage intensity corresponding to the different pulse durations, where the highest peak threshold damage intensity is found to be  $12.9 \text{ TW}/\text{cm}^2$  with shorter pulse duration (i.e. 167 fs) and the lowest peak threshold damage intensity is obtained  $4.1 \text{ TW}/\text{cm}^2$  with longer pulse durations (i.e. 1000 fs). However, in the case of damage peak threshold fluence, the higher damage threshold fluence is obtained  $5.1 \text{ J}/\text{cm}^2$  for longer pulse duration, which is shown in fig. 7.7 and lower damage threshold fluence is found to be  $1.2 \text{ J}/\text{cm}^2$  for 167 fs case.

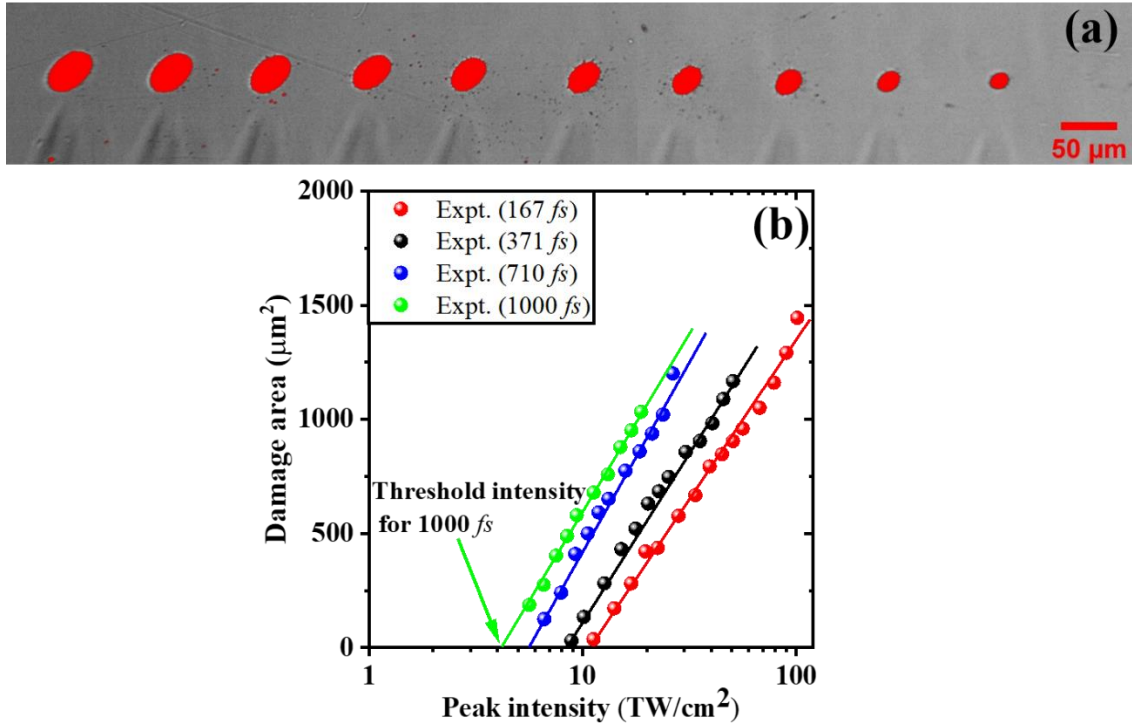


Figure 7.6: (a) Determining (a) damage area from optical microscopic images for the different pulse durations (i.e. 167, 371, 710, and 1000 fs) and (b) the damage threshold peak intensity with different pulse durations (i.e. 167, 371, 710, and 1000 fs).

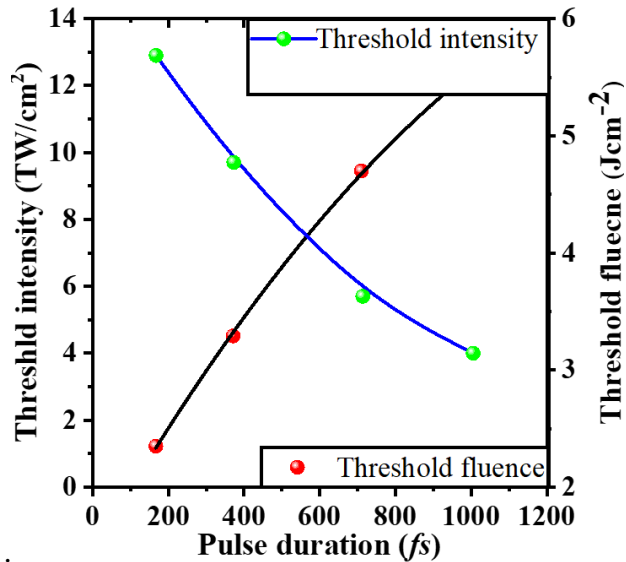


Figure 7.7: The damage threshold peak fluence/intensity with different pulse durations



The relation between the damage threshold peak fluence and pulse duration can be explained with simple scaling laws derived by Gamaly et al. [14] as  $F_{th} \sim t_{on}^\eta$ , where  $\eta$  can be found from the fitting of damaged peak fluence vs pulse duration ( $t_{on}$ ) graph which is found to be  $\eta = 0.23$  in this study that is similar to the literature value for shorter pulse cases [15]. Similarly, the relation between the damaged threshold peak intensity and pulse duration can be expressed as  $I_{th} \sim F_{th}/t_{on}$ .

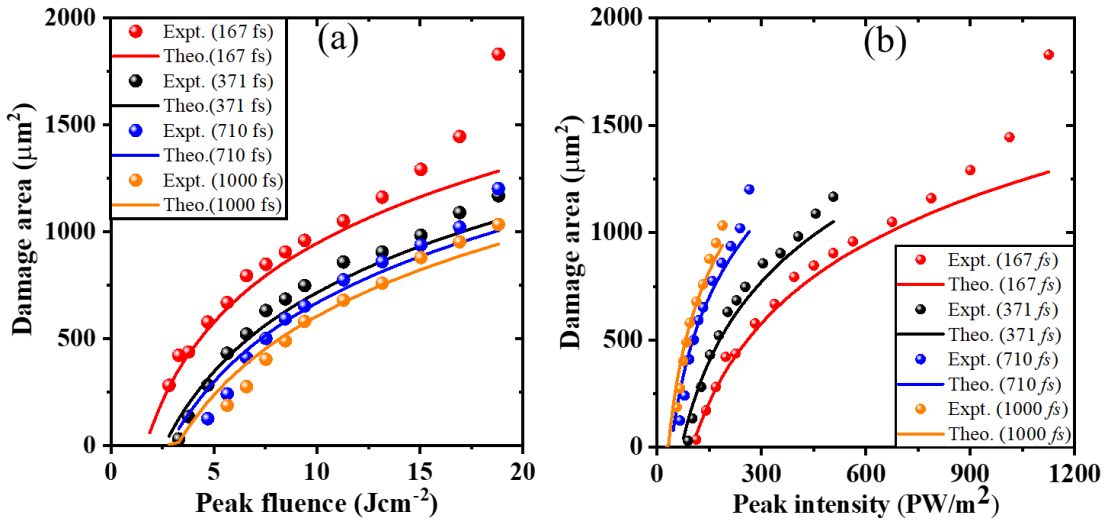


Figure 7.8: Comparing theoretical and experimental damaged area as a function of (a) peak fluence and (b) peak intensity.

To compare the front surface damage area of experimental results with theoretical calculation, the theoretical damage areas for different pulse duration are determined by using the following equation

$$A = \frac{1}{2} \pi \omega_o^2 \ln\left(\frac{I_o}{I_{th}}\right) \quad (7.3)$$

where  $I_o = \frac{2E_p}{\pi\omega_0^2 t_{on}}$  and  $I_{th}$  are the incident peak intensity and the damaged threshold peak intensity.

The damaged threshold peak intensity is obtained from Fig. 7.6. Fig. 7.8 shows the damaged area as a function of peak intensity and peak fluence for different pulse durations. Smaller damages are obtained with lower fluences, which agrees with the literature [16]. The theoretical calculation shows a good match with experimental results except for high intensities and shorter pulse durations, where the peak intensity is too high that leads to creating air ionization or other nonlinear phenomena, which is not considered in this calculation.

#### 7.4 Field enhancement and the back surface damage

Fig. 7.9 shows the front and back surface damage with 1000 fs pulse duration. For 1000 fs pulse duration case, strong back surface damage is observed with pulse energy  $< 30 \mu\text{J}$ , although the front surface damage appears at  $30 \mu\text{J}$  and no front surface damage  $< 30 \mu\text{J}$ . The possible reason could be explained with the electric field enhancement at the exit side and self-focusing due to the nonlinear refractive index change with an ultrafast laser pulse.

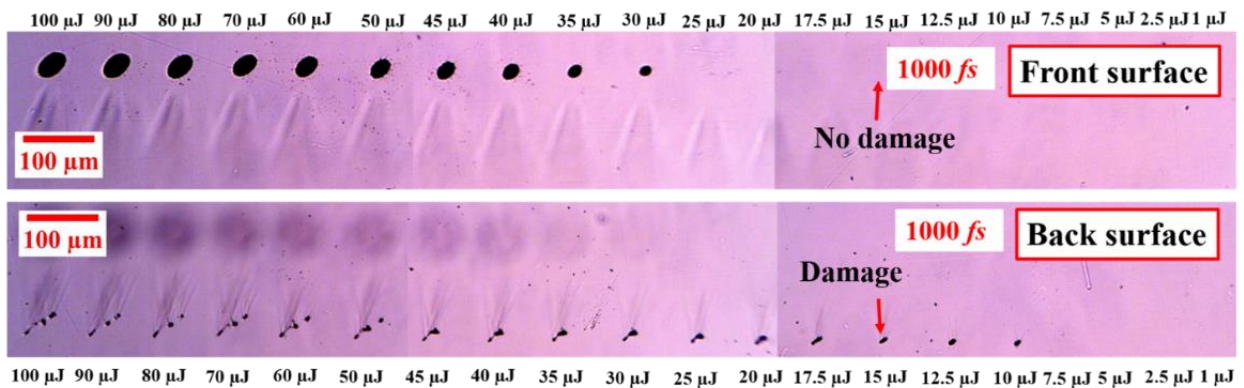


Figure 7.9: Front and back surface damage with 1000 fs pulse duration.

When light travels from a lower refractive index medium to a higher refractive index medium, the reflected electric field suffers a phase shift of  $180^\circ$  in relation to the incident light



wave. For traveling from a higher refractive index to a lower index medium, the reflected electric field has zero ( $0^\circ$ ) phase shift. To verify the electric field enhancement at the exit surface, Crisp et al. [17] gave a simple expression as below

$$\frac{S_{ent}^D}{S_{exit}^D} = \frac{4n^2}{(n+1)^2} \quad (7.4)$$

where  $S_{ent}^D$  is the incident power per unit area that corresponds to damage of the entrance face and  $S_{exit}^D$  is the incident power per unit area that corresponds to the damage of the entrance face. Since the Rayleigh length in this study is higher than the thickness of the sample,  $450 \mu\text{m}$ , and therefore, with the assumption of no self-focusing and a same beam diameter at the exit surface as the front surface, Equation (7.4) can be written as

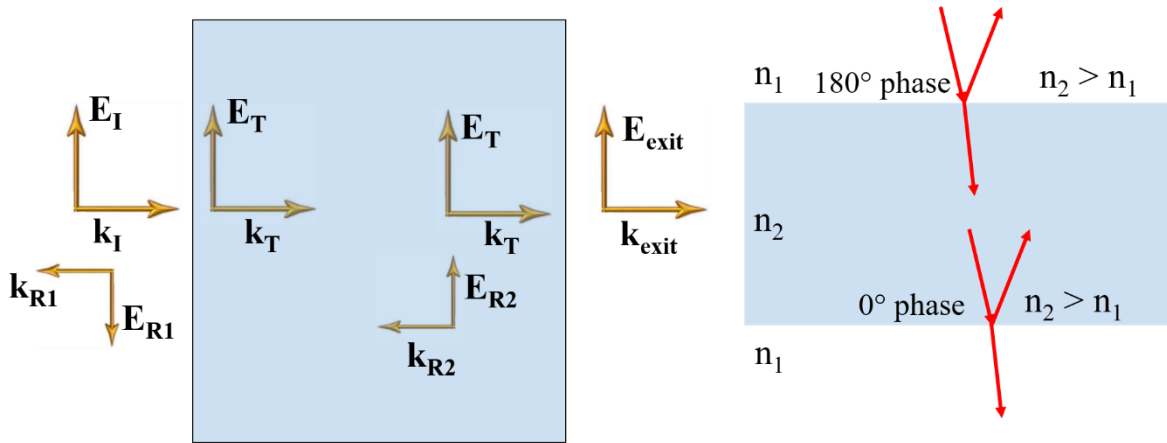


Figure 7.10: Electric fields at the entrance and back surface of the polymer surface. An incident angle is considered at a normal incident.

$$\frac{E_{ent}^D}{E_{exit}^D} = \frac{4n^2}{(n+1)^2}$$

(7.5)

where  $E_{ent}^D$  and  $E_{exit}^D$  are the threshold pulse energy at the entrance surface and threshold pulse energy at the exit surface, respectively. Here, the left side of the equation (7.7) is found to be  $\frac{E_{ent}^D}{E_{exit}^D} = 4$  from experimental results and the right-hand side are found to be 1.44 (where the linear refractive index is 1.44). Therefore, Equation (7.4) is not satisfied properly with our experimental results. To obtain the information on the diameter of the laser beam at the front surface and back surface from our experimental results, the damaged area at the front side and backside is plotted with  $M = \ln\left(\frac{2E_p}{t_{on}I_{th}}\right)$  and equation (7.6) is used to fit the experimental data.

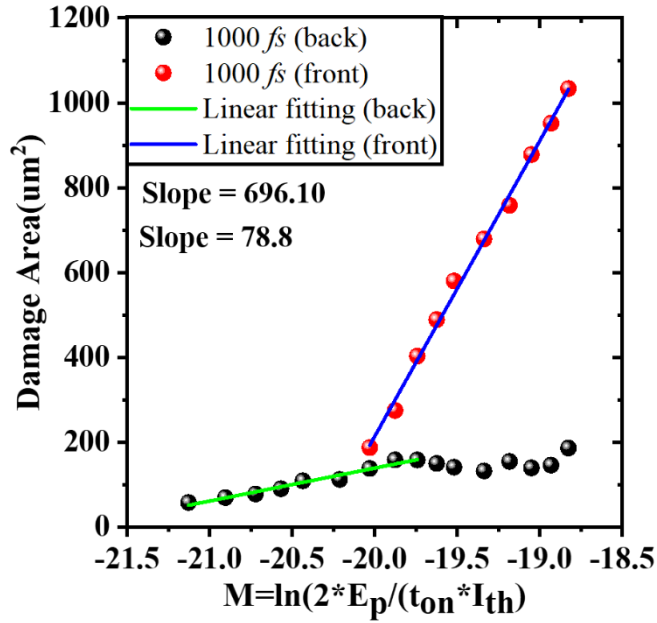


Figure 7.11: Determining the beam diameter at the front and the back surface from experimental damage diameter

$$\pi\omega_{damage}^2 = \pi\omega_{beam}^2 \ln\left(\frac{2E_p}{t_{on}I_{th}}\right) - \pi\omega_{beam}^2 \ln(A)$$

(7.6)

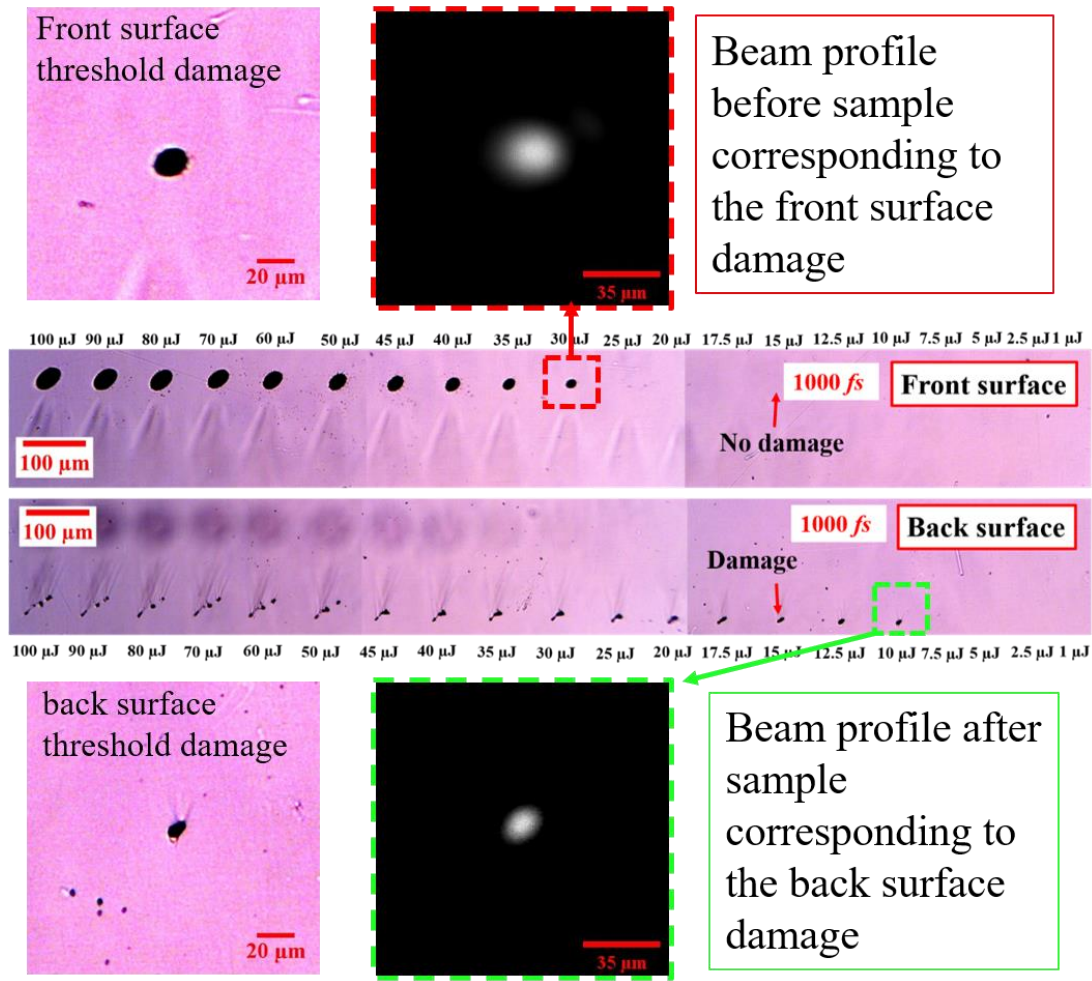


Figure 7.12: Camera image of the beam diameter at the entrance surface and the exit surface

The ratio of the entrance beam radius and the back surface beam radius is found to be 3.72

( $\frac{r_{entrance}}{r_{exit}} \approx 3.72$ ) from the slope value,  $\pi\omega_{beam}^2$  of the above in Fig. 7.11. This result indicates that

the diameter of the beam at the back surface is smaller than the beam diameter at the front surface.

To verify this result, a simple experiment is designed to measure the beam diameter at the front surface (without any sample) and the beam diameter at the back surface. Fig. 7.12 shows the

camera images at the front surface (without sample) and the back (exit) surface of the sample, which indicates also that the beam diameter at the back surface is much smaller than the front surface. From these experimental verifications, it is obvious that the field enhancement might not be the only reason for the back surface damage, and there might be a self-focusing effect[17,18], which leads to strong back surface damages.

### 7.5 Effect of the pulse duration on optical properties

Fig. 7.13 shows the reflectance ( $R$ ), transmittance ( $T$ ), and absorptance ( $A$ ) as a function of the peak fluences for the different pulse durations (i.e. 167 fs, 371 fs, 710 fs, and 1000 fs). As mentioned in Section 7.4 that the single-shot experiment is performed to see the effect of the pulse duration for a wide range of pulse energy from 1  $\mu\text{J}$  to 100  $\mu\text{J}$ , which corresponds to the fluence of 0.94  $\text{Jcm}^{-2}$  to 18.8  $\text{Jcm}^{-2}$ . Fig. 7.13 (a) shows the reflectance of the transparent PP sample as a function of the peak fluence of the incident laser beam, where reflectances are very low as the sample is mostly transparent. Note that the tolerance of this measurement is about  $\pm 0.012$ . Fig. 7.13 (a) shows that the reflectance with different pulse durations is within the tolerance limit, which indicates that the reflectance is not much dependent on pulse duration for a transparent PP sample case. It can be seen that the reflectance starts to decrease after a certain value of fluence from which the nonlinear absorption mechanism starts.

Fig. 7.13(b) and 7.13(c) show the transmittance ( $T$ ) and absorptance of the ultrafast laser beam through the transparent PP sample. At low fluences, the transmittances for all pulse durations have almost constant values, which indicates the linear absorption mechanism with low fluences. The transmittance starts to decrease after certain fluences, where nonlinear absorptions start to happen. However, the transmittance starts decreasing first for 167 fs pulse duration due to the high

peak intensity leading to nonlinear absorption with lower fluence that also supports the damage morphology shown in Section 7.4. Although the peak intensity for case 1000 fs is less, transmittance starts to decrease earlier than 371 fs and the 710 fs case, which might be the reason for strong back surface damage shown in Fig. 7.10.

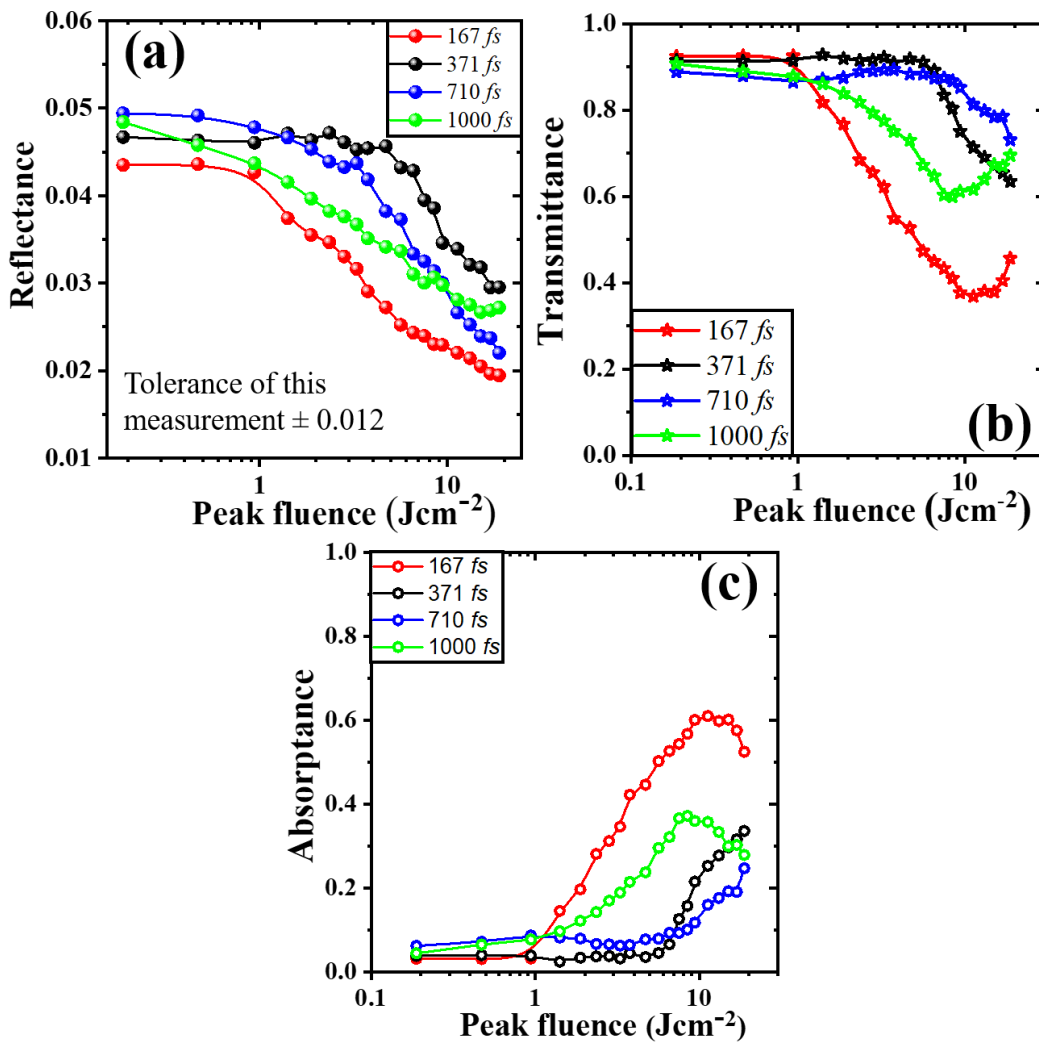


Figure 7.13: (a) Reflectance (R), (b) transmittance (T), and (c) absorptance (A) as a function of laser fluences with different pulse durations (i.e. 167 fs, 371 fs, 710 fs, and 1000 fs).

Fig. 7.13(C) shows the absorptance during the ultrafast laser interaction with a transparent PP sample, which is determined from the experimental value of transmittance and reflectance as  $A = 1 - T - R$ . As the reflectance of this study is very small, so the transmittance has a dominant effect in determining absorptance. As explained in the transmittance case, for low fluence the absorptance is constant for the linear absorption mechanisms and starts to increase after certain fluence ( i.e.  $1 \text{ Jcm}^{-2}$  for 167 fs pulse duration).

### 7.6 Theoretical analysis and discussion

The equation (7.2) describes the attenuation of the spatial and radial intensity,  $I(r, z, t)$  of the ultrafast laser, which is passing through the material undergoing single-photon, two-photon, or two-steps or three-photon or three-steps absorption considering multiple reflections as discussed in chapter 5.

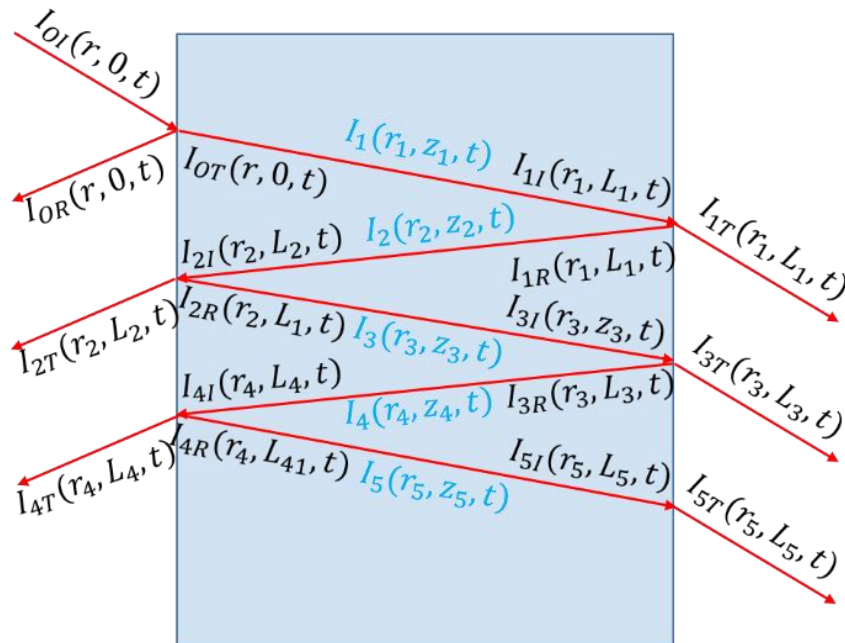


Figure 7.14: The multiple reflection is considered as an inclined laser beam that is irradiated on the transparent PP sample

The total transmitted intensity at the exit side of the sample is given by

$$I_T(r, z, t) = \sum_{m=0}^{\infty} I_{(2m+1)T}(r_{(2m+1)}, L_{(2m+1)}, t) \quad (7.7)$$

Here, the transmitted light at each of the points are  $I_{iT}(r_i, L_i, t)$ . The total reflected light intensity at the exit side of the sample is given by

$$I_R(r, z, t) = I_{OR}(r, 0, t) + \sum_{m=1}^{\infty} I_{(2m)T}(r_{(2m)}, L_{(2m)}, t) \quad (7.8)$$

The transmittance,  $T$ , and reflectance,  $R$ , of the ultrafast laser pulse through the PP sample can be found from the above solution in Eq. (7.2), which can be express in term of output pulse energy,  $E_{out}$  and input pulse energy,  $E_{in}$  as below:

$$T = \frac{I_T(r, z, t)}{I_{OI}(r, 0, t)}$$

$$R = \frac{I_R(r, z, t)}{I_{OI}(r, 0, t)} \quad (7.9)$$

Here,  $I_{OI}(r, 0, t)$ ,  $I_T(r, z, t)$  and  $I_R(r, z, t)$  are the incident, total transmittance, total reflectance laser intensity, respectively.

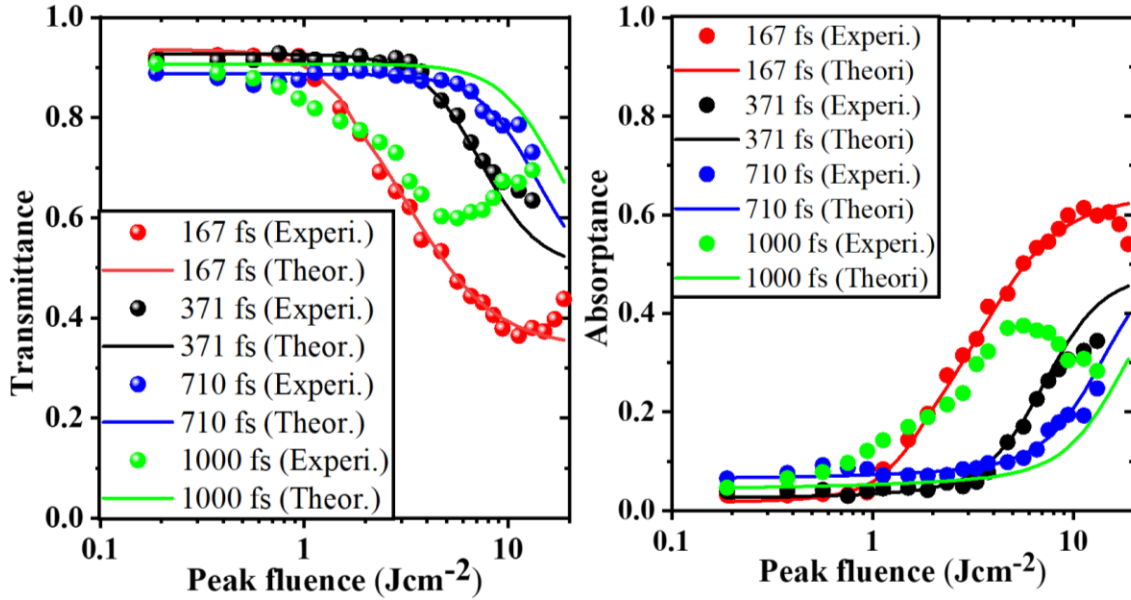


Figure 7.15: The experimental results of (a) transmittance and (b) absorbance ( $A = 1 - R - T$ ) for different pulse durations (i.e. 167 fs, 371 fs, 710 fs, and 1000 fs) are fitted with the theoretical calculation.

In this study, the linear and nonlinear absorption coefficients are determined from the fitting results of the experimental data of  $T$ , and  $A (= 1 - R - T)$  with the theoretical calculation of Eq. (7.12) for different pulse durations, i.e. 167, 371, 710, and 1000 fs, which is shown in fig. 7.15. The average value of the linear (single-photon) absorption coefficient for three pulse durations (i.e. 167, 371, and 710 fs) is found to be  $\alpha_1 = (110.45 \pm 3) \text{ m}^{-1}$ , which agrees with the experimental value determined from the linear spectroscopic measurement for the thickness of the transparent sample,  $L = 450 \text{ }\mu\text{m}$ . For 1000 fs case, strong back (exit) surface damage is observed. Possible reasons could be self-focusing, electric field enhancement or other nonlinear effects, which are not accounted for in this model. Therefore, the transmittance and absorbance for the 1000 fs case show differences between theoretical and experimental results.



This study suggests that the non-resonant vibrational overtone or combination absorption happens at 1030 nm and 515 nm, and resonant overtone or combination happens at 353 nm due to the wavelength shifting caused by the nonlinear self-phase modulation (SPM) that has been discussed in Chapter 5. The linear refractive index of this transparent PP sample is 1.49. The average (from three pulse duration) value of nonlinear absorption coefficients for two-photon or two-steps absorption and the three-photon or three steps are found to be  $\alpha_2 = (8.01 \pm 2.15) \times 10^{-13} \text{ mW}^{-1}$  and  $\alpha_3 = (3.21 \pm 1.0) \times 10^{-29} \text{ m}^3 \text{W}^{-2}$ , respectively from the fitting result, those values are consistent with the previously reported value for the polymeric materials[19,20]. The average (from three pulse duration) value of nonlinear refractive indexes are found to be  $n_2 = (3.22 \pm 1.15) \times 10^{-20} \text{ m}^2 \text{W}^{-1}$  and  $n_3 = (2.64 \pm 1) \times 10^{-37} \text{ m}^4 \text{W}^{-2}$ .

### 7.7 Summary

The effect of the pulse duration is investigated both experimentally and theoretically. This study showed the most effective energy region for processing transparent PP samples with ultrafast lasers with different pulse durations. The shorter pulse duration (167 fs) is preferred for surface processing, while longer pulses (~ 1 ps) create sub-surface and back-surface damages. The back surface damage with 1000 fs is suggested to happen due to self-focusing phenomena, which has lower critical power for a longer pulse. This study also shows that the shorter pulses have higher distortion than the longer pulse inside the material and most absorptances happen for the shorter pulse is at the surface of the material.

## 7.8 References

1. K. Sugioka and Y. Cheng, “Ultrafast lasers - reliable tools for advance materials processing,” *Light: Sci. Appl.* 3(4), e149 (2014).
2. R. R. Gattass and E. Mazur, “Femtosecond laser micromachining in transparent materials,” *Nat. Photonics* 2(4), 219–225 (2008).
3. K. C. Phillips, H. H. Gandhi, E. Mazur, and S. K. Sundaram, “Ultrafast laser processing of materials: a review,” *Adv. Opt. Photonics* 7(4), 684–712 (2015).
4. A. Shibata, S. Yada, and M. Terakawa, “Biodegradability of poly (lactic-co-glycolic acid) after femtosecond laser,” *Sci. Rep.* 6, 27884 (2016).
5. M. Terakawa, “Femtosecond laser processing of biodegradable polymers,” *Appl. Sci.* 8, 1123 (2018).
6. A. Rahaman, A. Kar, and X. Yu, “Thermal effects of ultrafast laser interaction with polypropylene,” *Opt. Express* 27(4), 5764-5783 (2019).
7. A. Rahaman, X. Du, B. Zhou, H. Cheng, A. Kar, and X. Yu., “Absorption and temperature distribution during ultrafast laser micro-cutting of polymeric materials”, *J Laser Appl.* 32, 022044 (2020).
8. B. Zhou, A. Rahaman, X. Du, H. Cheng, A. Kar, and X. Yu, “Laser processing of dielectrics using spatiotemporally tuned ultrashort pulses”, *J Laser Appl.* 32, 022041(2020).
9. K. Sugioka, “Progress in ultrafast laser processing and future prospects”, *Nanophotonics* 6(2), 393 – 413 (2017).
10. M. V. Shugaev, C. Wu, O. Armbruster, A. Naghilou, N. Brouwer, D. S. Ivanov, T. J. Y. Derrien, N. M. Bulgakova, W. Kautek, B. Rethfeld and L. V. Zhigilei, “Fundamentals of ultrafast laser-interaction”, *MRS Bull.* 41, 960 – 968(2016).
11. F. Bourquard, J. P. Colombier, M. Guillermin, A. S. Loir, C. Donnet, R. Stoian, and F. Garrelie, “Temporal pulse shaping effects on aluminum and boron ablation plumes generated by ultrashort pulsed laser ablation and analyzed by time- and space-resolved optical spectroscopy” *Appl. Sur. Sci.*, 258, 9374-9378 (2012).
12. R. Stoian, M. Boyle, A. Thoss, A. Rosenfeld, G. Korn, I.V Hertel, and E. E. B. Campbell “Laser ablation of dielectrics with temporally shaped femtosecond pulses” *Appl. Phys. Lett.* 80, 353-355 (2002).
13. M. Spyridaki, E. Koudoumas, P. Tzanetakis, and C. Fotakis, “Temporal pulse manipulation and ion generation in ultrafast laser ablation of silicon”, *Appl. Phys. Lett.*, 84, 1474 (2003).
14. E.G. Gamaly, A. V. Rode, and B. Luther-Davies, “Ablation of solids by femtosecond lasers: Ablation mechanism and ablation threshold for metals and dielectrics” *Physics of Plasma* 9, 949(2002).

15. A. Bendib, K. Bendib-Kalache, and C. Deutsch, "Optical breakdown threshold in fused silica with femtosecond laser pulses" *Laser and Particle Beams* 31, 523-529 (2013).
16. B. N. Chichkov, C. Momma, S. Nolte, F. V. Alvensleben, and A. Tunnermann, "Femtosecond, picosecond and nanosecond laser ablation of solids" *Appl. Phys.* 63, 109-115(1996).
17. S. Butkus, E. Gaizauskas, L. Macernyte, V. Jukna, D. Paipulas, and V. Sirutkaitis, "Femtosecond beam transformation effects in water, enabling increased throughput micromachining in transparent materials," *Appl. Sci.* 9, 2405 (2019).
18. D. M. Rayner, A. Naumov, and P. B. Corkum, " Ultrashort pulse non-linear optical absorption in transparent media," *Opt. Express* 9, 3208-3217(2005).
19. T. Chang, X. Zhang, X. Zhang, and H. L. Cui, Accurate determination of dielectric permittivity of polymer from 75 GHz to 1.6 THz using both S- parameters and transmission spectroscopy, *Appl. Opt.* 56, 3287 (2017).
20. C. Schnebelin, C. Cassagne, C. B. D. Araujo, and G. Boudebs, Measurements of the third- and fifth-order optical nonlinearities of water at 532 and 1064 nm using the  $D4\sigma$  method *Opt. Lett.* 39, 5046 (2014).

## CHAPTER 8: CONCLUSIONS

### 8.1 Conclusions

Ultrafast lasers are the predominant tool for high precision material processing. Although polymers were one of the first materials to be processed by ultrafast lasers, it remains still challenging to process polymers with high energy efficiency due to different linear and nonlinear absorption mechanisms during the ultrafast laser-material interaction. In this study, A Yb: KGW (Yb doped potassium gadolinium tungstate) femtosecond laser with near-IR wavelength is used to understand the ultrafast laser interaction with polypropylene (PP), which is an important material for different industrial and scientific applications. Experiments are carried out to understand the dynamics of the ultrafast laser interaction with polypropylene and experimental results are explained with the model that includes both linear and nonlinear phenomena, which leads to the following conclusions:

1. It is found that heat accumulation can be avoided with a proper choice of the processing conditions. It is common practice to run the ultrafast laser at a high repetition rate and hence high average power to make ultrafast laser materials processing compatible with the scale and throughput needed for industrial application. However, the heat accumulation under such conditions will deteriorate the processing quality, especially for polymers, which typically has a low melting temperature. An analytical thermodynamics model is developed to understand heat accumulation that occurs in laser processing of polymers under the conditions of high repetition rates and high pulse energies and experimental results are found to agree with theoretical predictions. The results are useful for selecting laser parameters in the processing of polymers.

2. The total absorbed energy and the total absorbed energy in the material during are two important figures of merit to predict the laser cutting performance. The depths of cavities under partial-depth cutting conditions with different laser parameters fit into a single straight line as a function of absorbed laser intensity or absorbed total pulse energy.

3. The material removal rates are found to have a linear relationship with the absorbed laser energy for different values of absorptivity under various laser-material interaction conditions, indicating that the thermal effects of different laser parameters are similar but the optical effects, i. e., the absorptivities, are different. Besides, the volumes of vaporized material also coincide with a single straight line as a function of the absorbed laser power.

4. Transient optical properties (reflectance, transmittance, absorptance) are measured in situ during a single ultrashort laser pulse interaction with opaque and pure polypropylene (PP) for a wide range of pulse energies by using an ellipsoidal mirror, which is capable to collect the majority of the light that reflects from the irradiated PP sample.

5. Experimental results showed that the interaction of the ultrafast laser pulse with polypropylene can be divided into three regions depending on nature (linear or nonlinear) of absorption that happens for the different peak intensity and the peak fluence. The measured transmittance is explained by a model that takes into account different effective absorption regions, and the non-linear absorption coefficient is estimated from the theoretical fitting of experimental results.

6. The aforementioned result suggests that nonlinear absorption in PP at 1030 nm wavelength is initiated by multiphoton absorption through high-order overtones, where the result suggests that the non-linear absorption originates from the two-step or two-photon occurs for

opaque PP, and three-steps or three-photon for transparent PP through vibrational overtone or combination.

7. The ultrafast laser interaction mechanisms with transparent PP and opaque PP is found to be distinct from each other, and the reason is suggested to be the impurity present in the opaque samples, which enhances the absorptance in the materials. The mechanism responsible for the ultrafast laser interaction with transparent PP and opaque PP can be explained by the observed morphologies after laser irradiation as shown in Chapter 5. Opaque and pure PP exhibit different morphologies in the irradiated zone. While craters are formed for opaque PP, pure PP first undergoes swelling with a single pulse, and then craters are formed with a second pulse. This is in agreement with in situ optical measurements.

8. The pulse-to-pulse evolution of optical properties (reflectance, transmittance, absorptance) of PP is determined by performing time-resolved measurements from pulse to pulse for a wide range of pulse energies. It is found that PP undergoes dramatic morphological change from pulse to pulse, which accompanied the changes in optical properties that call for the tuning of laser condition in order to fully utilize the laser energy. These results could help increase energy-efficiency in ultrashort pulsed laser processing of polymers towards the high-throughput operation.

9. An enhancement in absorptance is observed at certain ( $>1 \text{ J/cm}^2$ ) fluences. At even higher fluences, effects such as plasma shielding reduce absorptance. This indicates a window of optimal energy efficiency at around  $9.4 \text{ J/cm}^2$ . The enhancement is more pronounced for shorter pulses (i.e., 167 fs) than longer pulses (i.e., 1000 fs).

10. The effect of pulse duration is investigated in this study, where short pulse duration (167 fs) is preferred for surface processing, while longer pulses ( $\sim 1 \text{ ps}$ ) create sub-surface and

back-surface damages. An analytical equation is derived to model nonlinear beam propagation with the inclusion of optical Kerr effect and self-phase modulation.

## 8.2 Future works

➤ This study showed the evaluation of optical properties (i.e. absorptance, transmittance, and reflectance) of ultrafast laser processing of a pair of pulses, where the first pulse creates swelling, and 2<sup>nd</sup> pulse creates a deep crater. However, the evaluation of optical properties for a few pulses could be interesting to observe to have high precision laser micro/nano dilling on the surface of polymers. The current study has done for longer delay of 1 ms, where the material is considered to be cooled down before 2<sup>nd</sup> pulse arrives at the surface of the material. The different delay might give a better understanding to improve the processing quality of the ultrafast laser processing.

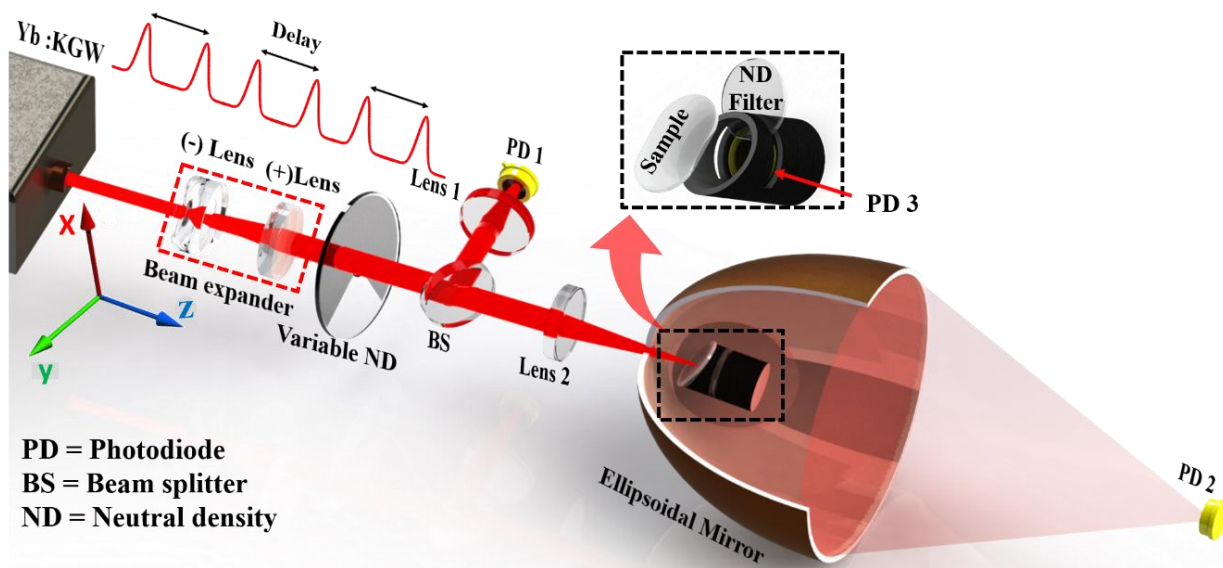


Figure 8.1: Experimental set up for measuring the optical properties of ultrafast laser interaction with transparent PP for multi-pulses.

➤ The current study suggested that the nonlinear absorption mechanism originates from the two-steps or two-photon and three-steps or three-photon vibrational overtone or

combination absorption for the near-infrared wavelength of 1030 nm. Note that the absorption at wavelengths ranging from 800 to 2500 nm, which corresponds to wavenumber 12,500 to 4000  $\text{cm}^{-1}$ , is present in polymers based on overtone/combination absorption. However, high energy photons with UV wavelengths can be used to trigger electronic absorption, which might improve the process quality of polymeric material by avoiding thermal effects inside the material. In that case, the third harmonic generation of the fundamental wavelength of 1030 nm could be used.

➤ Material processing requires good control of laser material interaction under the condition of high average laser power and high peak intensity. The current study can be used to fabricate microfluidic channels, as shown in Fig. 8.2..

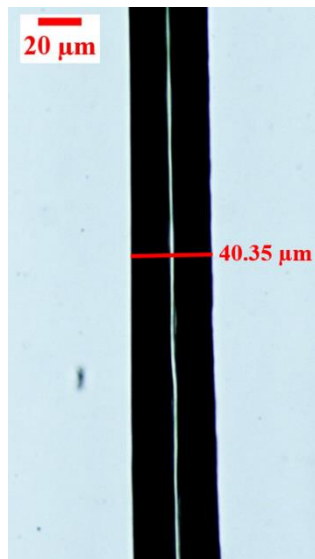


Figure 8.2: A microfluidic channel fabricated with ultrafast laser

➤ The experimental setup of the time-resolved measurement in this study could be used to detect laser-generated plasma emission and identify the elements present in the sample by replacing PD2 with a spectrum analyzer as shown below



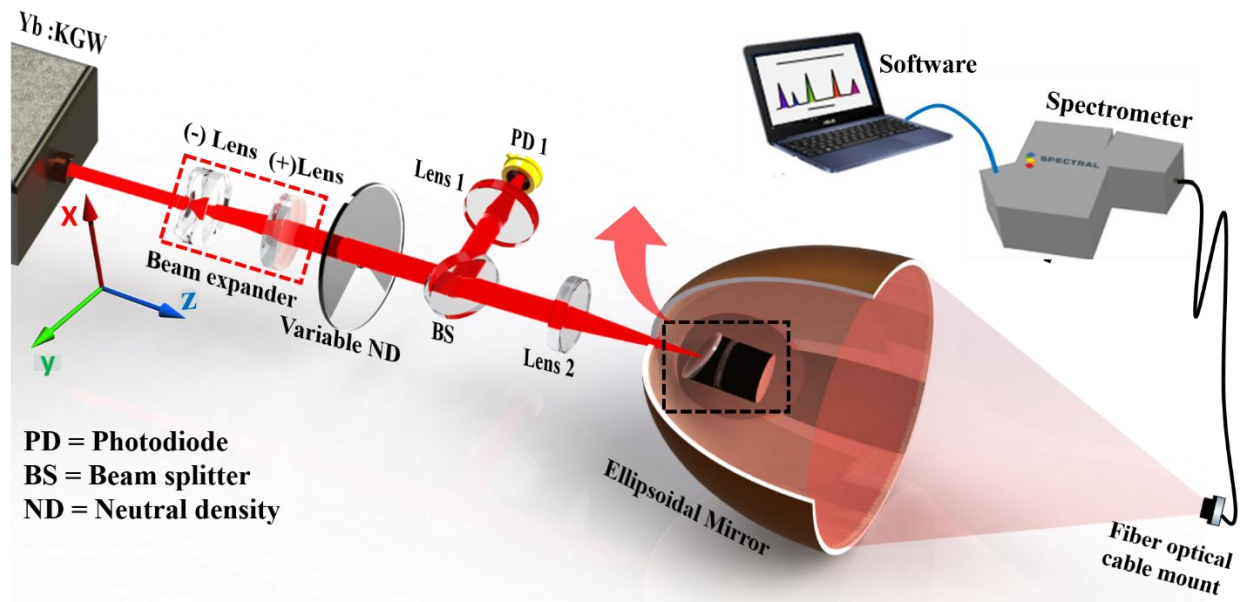


Figure 8.3: Experimental set up for optical sensing in laser material processing applications

## Appendix: Publications

### Publications: Journal

1. **Arifur Rahaman**, Aravinda Kar, and Xiaoming Yu, Thermal effects of ultrafast laser interaction with polypropylene, *Optics express*, 27, 5764-5783 (2019).
2. **Arifur Rahaman**, Aravinda Kar, and Xiaoming Yu, “Time-resolved measurements of optical properties in ultrafast laser interaction with polypropylene”, *Optics Express*, 28, pp. 2640-2648 (2020).
3. **Arifur Rahaman**, Xinpeng Du, Boyang Zhou, He Cheng, Aravinda Kar, and Xiaoming Yu, “Absorption and temperature distribution during ultrafast laser micro-cutting of polymeric materials”, *Journal of Laser Applications*, 32, 022044 (2020).
4. Boyang Zhou, **Arifur Rahaman**, X. Du, H. Cheng, A. Kar, M. J. Soileau and Xiaoming Yu, “Laser Processing of Dielectrics Using Spatiotemporally Tuned Ultrashort Pulses” *Journal of Laser Applications*, 32, 022044 (2020).
5. **Arifur Rahaman**, Aravinda Kar, and Xiaoming Yu, Dynamics of ultrafast laser interaction with opaque and transparent polypropylene, *Journal of Applied Physics*, 2020 (Manuscript preparing).
6. **Arifur Rahaman**, Aravinda Kar, and Xiaoming Yu, Evaluation of optical properties of ultrafast laser micro-processing of polymers”, *Journal of Laser application*, 2020. (Submitted)
7. **Arifur Rahaman**, Aravinda Kar, and Xiaoming Yu, “The spatial and temporal distortion of ultrafast laser pulse inside a nonlinear media” (Manuscript preparing).
8. Boyang Zhou, **Arifur Rahaman**, Xinpeng Du, Aravinda Kar, M. J. Soileau, and Xiaoming Yu, “Near-threshold characteristics of ultrashort laser pulses interaction with solids” *Journal of Laser applications* (2020). (Submitted)

## **Publications: Conference**

1. **Arifur Rahaman**, Xinpeng Du, Boyang Zhou, He Cheng, Aravinda Kar, Xiaoming Yu, Absorption, and Temperature Distribution during Ultrafast Laser Microcutting of Polymeric Materials, 2019 ICALEO (Laser Institute of America, Orlando, 2016), Orlando, Florida, October 7-100, 2019.
2. Xinpeng Du, **Arifur Rahaman**, Aravinda Kar, Michael Chase, Dave Wolfe, John Mathy, Xiaoming Yu, Laser Processing over a Large Area by Wavefront-Controlled Scanning, 2019 ICALEO (Laser Institute of America, Orlando, 2016), Orlando, Florida, October 7-100, 2019.
3. Boyang Zhou, **Arifur Rahaman**, He Cheng, Yingjie Chai, Aravinda Kar, MJ Soileau, Xiaoming Yu "Optical breakdown and sub-optical-cycle dynamics in laser-induced damage using single and a burst of ultrashort pulses" SPIE Photonics West 2019.
4. Boyang Zhou, Aravinda Kar, M.J. Soileau, **Arifur Rahaman**, Xinpeng Du, Xiaoming Yu, Laser Processing of Dielectrics Using Spatiotemporally Tuned Ultrashort Pulses" 2019 ICALEO (Laser Institute of America, Orlando, 2016), Orlando, Florida, October 7-100, 2019.
5. **Arifur Rahaman**, Aravinda Kar, and Xiaoming Yu, Evaluation of optical properties of ultrafast laser micro-processing of polymers", 2020 ICALEO (Laser Institute of America, Orlando, 2016), Orlando, Florida, October 19-20, 2020. (Accepted)
6. Boyang Zhou, **Arifur Rahaman**, Xinpeng Du, Aravinda Kar, M. J. Soileau, and Xiaoming Yu, "Near-threshold characteristics of ultrashort laser pulses interaction with solids" 2020 ICALEO (Laser Institute of America, Orlando, 2016), Orlando, Florida, October 19-20, 2020.(Accepted)